Structural Study of Enteroviruses

- Ling Qin

Division of Structural Biology
Nuffield Department of Medicine

Christ Church College

University of Oxford

A thesis submitted in partial fulfilment
for the degree of Doctor of Philosophy

Trinity Term 2023

Table of Contents

Abstract 6

Before reading 7

Numbering of Figure and Table 7

Abbreviations 7

Chapter one: Background 8

1.1 Enteroviruses 9

1.1.1 Origin 9

1.1.2 Pathogen 11

1.1.3 Agent 13

1.1.4 Traitor 16

1.2 Enterovirus life cycle and immune escape 17

1.2.1 Virus entry 18

1.2.2 Translation and Replication 20

1.2.3 Encapsidation and virus release 22

1.2.4 Immune escape 23

1.3 Structure facilitated drug design 25

1.3.1 Antivirals preventing enterovirus cell entry 26

1.3.2 Antivirals preventing enterovirus replication 30

1.3.3 Antivirals targeting other proteins 39

1.4 Single-particle analysis using cryo-EM 40

1.4.1 Brief history of cryoEM 41

1.4.2 Sample preparation and grid making 42

1.4.3 cryo-EM instrument 44

1.4.4 Data collection 47

1.4.5 Data processing 49

1.4.6 Structure building 51

1.5 Neutralizing antibodies against enterovirus 56

1.5.1 Enterovirus A71 58

1.5.2 Echovirus 59

1.5.3 Rhinovirus B14 60

1.5.4 Coxsackievirus 61

1.5.5 Enterovirus D68 63

Chapter Two: Methods and Materials 65

2.1 Molecular Cloning 66

2.1.1 Plasmid information and cloning workflow 66

2.1.2 pET28a-MSP-His plasmid linearization 68

2.1.3 Affinity tag replacement 69

2.1.4 pET28a-MSP-StrepII plasmid amplification 70

2.1.5 DAF cloning 70

2.2 Protein expression 71

2.2.1 cMSP26 from E.coli 72

2.2.2 SCARB2 and DAF from HEK-293T 73

2.3 Protein Purification 75

2.3.1 cMSP26 76

2.3.2 cMSP26 StrepII 77

2.3.3 SCARB2 and DAF 78

2.4 Enterovirus culture and purification 79

2.4.1 RD cell culture and enterovirus infection 79

2.4.2 Enterovirus purification 80

2.5 Grid making and EM data collection 82

2.5.1 Negative stain microscopy 82

2.5.2 cryo-EM sample preparation 83

2.5.3 cryo-EM data collection 85

2.6 EM data processing 86

2.6.1 Echo11-DAF 86

2.6.2 Poliovirus VLP – pAB 91

2.6.3 SyRe protocol 97

2.7 Nanodisc experiments 98

2.7.1 Lipids preparation 98

2.7.2 Nanodisc assembly 99

2.7.3 SCARB2 incorporated nanodiscs 99

2.8 Thermofluor experiment 100

2.9 Phylogenetic analysis 101

Chapter Three: Echovirus 11 - DAF 102

3.1 Introduction 103

3.2 Structure of the Echovirus 11 - DAF complex 105

3.3 Improved DAF density 108

3.4 Echovirus 11 - DAF interaction 110

3.5 Two binding modes of DAF to enteroviruses 113

3.6 Discussion 117

Chapter Four: Poliovirus VLP - polyclonal antibodies 119

4.1 Introduction 120

4.2 Overall structures 124

4.3 2-fold pAb1 attaching to expanded PV1 128

4.4 3-fold pAb1 attaching to expanded PV1 131

4.5 Other pAb1 attaching to expanded PV1 134

4.6 New epitopes provided by an absent pentamer 141

4.7 Semi-attached pentamer 145

4.8 Conclusions and Discussion 146

Chapter Five: Enterovirus A71 - SCARB2 – nanodisc..... 148

5.1 Introduction 149

5.2 Nanodisc(His)-SCARB2-EV71 complex 155

5.3 Nanodisc(StrepII)-SCARB2-EV71 complex 161

5.4 Environmental trigger 167

5.5 Conclusion and Discussion 170

Chapter Six: Conclusions and Future directions 172

Acknowledgements 177

References: 180

Abstract

Enteroviruses comprise a genus of picornaviruses causing global morbidity and regional outbreaks. These viruses are the causative agents of severe, widespread diseases such as hand-foot-and-mouth disease, poliomyelitis and aseptic meningitis. Although they have been studied for decades, few vaccines or drugs are in use. Indeed, many structural details of enterovirus infection, immune response and life cycle remain unknown. Solving these structural mysteries may provide crucial information that aids the elimination of these infectious particles.

The work described in this thesis extends our structural understanding of enteroviruses detailing the receptor binding manner of Echovirus 11 and closely related enteroviruses (chapter 3) and the polyclonal antibody response to poliovirus (chapter 4). To support these studies, a 'SyRe' protocol is described for analysis of enterovirus capsid proteins at protomer-scale, and pentamer-scale for the efficient detection of polyclonal antibody attachment (chapter 4). Finally, an *in-vitro* host cell membrane mimetic system is optimized to visualize virus-cell attachment and membrane penetration (chapter 5), together with powerful EM tools this will facilitate obtaining detailed structural information of virus entry in the near future.

Before reading

Numbering of Figures and Tables

To avoid confusion, all the figures and tables are numbered in this manner: Figure/Table x.y.z.n x = chapter number, y = section number, z = subsection number, n = the n^{th} figure/table in the subsection. If there is no subsection under a section, the number form is Figure/Table x.y.n.

Abbreviations

DAF: Complement Decay-Accelerating Factor, also known as CD55.

EVX is short for Enterovirus X, EX is short for Echovirus X, where X represent the number of virus type.

SCARB2: Scavenger Receptor Class B Member 2

RNC: Receptor(SCARB2)-Nanodisc Complex, sometimes expressed as SCARB2 incorporated nanodisc.

SyRe: Symmetry expansion, Re-center, Re-extraction and Re-construction. It is a data processing method especially designed for symmetrical proteins, especially enterovirus capsids. The 3 ‘Re’s protocol can also be applied to other large asymmetrical proteins to focus on a small portion of the protein. (for details go to chapter 2 section 2.6.3)

UMP: Uridene monophosphate

VRNC: Virus-Receptor-Nanodisc Complex, meaning EV71-SCARB2-Nanodisc Complex in this thesis (chapters 2 & 5).

Chapter one

Background

In this chapter, background knowledge of enteroviruses is described in detail, aiming to cover information

from the discovery of the first enterovirus to the near eradication of an enterovirus serotype

from macroscopic regional outbreaks to microscopic scientific breakthrough

from clinical infectious pathogens to cell-level secret agents

from vaccines to (therapeutic) antivirals

from life to death to life

……

1.1 Enteroviruses

1.1.1 Origin

Enteroviruses are a genus within the family *Picornaviridae* (Pico-rna-viridae = small-RNA-virus), which comprises small, non-enveloped, single-stranded RNA viruses. The genus enterovirus originates from the fact that these viruses primarily infect the enteric (intestinal) system (Entero = Greek word 'enteron' = intestine). Although Enteroviruses were first identified in the 1950s as a distinct group of viruses that were associated with gastrointestinal illness, they have been known to cause diseases in humans for almost two centuries.

According to Etymologia: From the Greek polios ("gray") + myelos ("marrow"), poliomyelitis may have plagued humanity since antiquity. The funerary stele of the Egyptian priest Ruma (~ 1400 BCE) shows a shortened, withered leg, in what is believed to be one of the earliest depictions of polio [1]. The first clinical observation date back to 1789 [1], and the first description of a polio-like illness was published in 1840 by the German physician Jakob Heine, who described an outbreak of paralysis in children in Würzburg, Germany [2]. However, it was not until the early 20th century that the causative agent of polio was identified by Dr. Karl Landsteiner and Dr. Erwin Popper [3], shortly after the devastating Scandinavian epidemic of poliomyelitis in 1905 [4].

The first non-polio enteroviruses to be identified were Coxsackievirus A and Coxsackievirus B, which were discovered in 1948 by Dalldorf and Sickles [5]. These viruses were originally isolated from patients with polio-like symptoms but were found to be distinct from poliovirus based on their antigenic properties and ability to grow in tissue culture.

Species	Types
Enterovirus A (*n* = 20)	CVA2–CVA8, CVA10, CVA12, CVA14, CVA16 EV-A71, EV-A76, EV-A89–EV-A91, EV-A114, EV-A119–EV-A121
Enterovirus B (*n* = 59)	CVA9 CVB1–CVB6 E1–E7, E9, E11–E21, E24–E27, E29–E33 EV-B69, EV-B73–EV-B75, EV-B77–EV-B88, EV-B93, EV-B97, EV-B98, EV-B100, EV-B101, EV-B106, EV-B107, EV-B111
Enterovirus C (*n* = 23)	CVA1, CVA11, CVA13, CVA17, CVA19–CVA22, CVA24 PV1–PV3 EV-C95, EV-C96, EV-C99, EV-C102, EV-C104, EV-C105, EV-C109, EV-C113, EV-C116–EV-C118
Enterovirus D (*n* = 4)	EV-D68, EV-D70, EV-D94, EV-D111

Table 1.1.1 Taxonomy of Enteroviruses infecting humans

Since the discovery of Coxsackieviruses, many other non-polio enteroviruses have been identified, including Enterovirus 71, Enterovirus D68, and several echovirus serotypes. Up to 2021, more than a hundred serotypes of Enterovirus have been classified into 4 species (Table 1.1.1) [6].

1.1.2 Pathogen

Enteroviruses as obligate human pathogens are a significant cause of morbidity and mortality throughout the world, especially for infants and young children. The transmission of human enteroviruses occurs through various routes, including fecal-oral, oral-oral, respiratory droplets (nasopharyngeal), and contaminated objects (fomites). Most commonly, enteroviruses enter the body through the fecal-oral route and replicate in the gastrointestinal tract, including the oropharyngeal and intestinal mucosa. The virus can be detected in respiratory secretions for 1-3 weeks and in faeces for 3-8 weeks [7]. Following initial replication in the respiratory or gastrointestinal tracts, mild symptoms typically appear within 3-5 days, with the potential for progression to more severe illness when the virus spreads to secondary organs such as the brain, liver, pancreas, and heart. Enteroviruses can cause systemic and localized infections, affecting multiple organ systems in individuals of all ages. Enteroviruses access to the central nervous system (CNS) mainly through three pathways: retrograde axonal transport, Trojan horse invasion, and direct infection [8]. While most enterovirus infections are asymptomatic or cause mild febrile illness, they can also lead to severe conditions (Table 1.1.2).

Species	Genotypes	Associated Disease	Strains
Human enterovirus A (EV-A)	Coxsackievirus (CV) Enterovirus (EV)	Encephalitis	CV-A2, CV-A3, CV-A4, CV-A5, CV-A6, CV-A7, CV-A8, CV-A16, EV-A71
		Paralysis or myelitis	CV-A2, CV-A4, CV-A5, CV-A7, CV-A8, CV-A16, EV-A71, EV-A76, EV-A89, EV-A90, EV-A91
		Meningitis	CV-A2, CV-A3, CV-A4, CV-A5, CV-A6, CV-A7, CV-A8, CV-A10, CV-A16, EV-A71
		Hand-foot-and-mouth disease	CV-A4, CV-A5, CV-A6, CV-A7, CV-A10, CV-A12, CV-A16, EV-A71
		Upper and lower respiratory disease	CV-A10, CV-A16, EV-A71
		Pleurodynia	CV-A2, CV-A4, CV-A6, CV-A10, CV-A16
		Herpangina	CV-A2, CV-A3, CV-A4, CV-A5, CV-A6, CV-A7, CV-A8, CV-A10, CV-A16, EV-A71
		Gastroenteritis	EV-A76, EV-A71, EV-A89, EV-A90
		Myopericarditis	CV-A16, EV-A71
		Pancreatitis	EV-A71
		Type I diabetes	EV-A71
Human enterovirus B (EV-B)	Coxsackievirus Echovirus (E) Enterovirus	Encephalitis	CV-A9, CV-B1, CV-B2, CV-B3, CV-B4, CV-B5, E-3, E-4, E-5, E-6, E-7, E-9, E-11, E-13, E-14, E-16, E-17, E-18, E-19, E-24 E- 25, E-27, E-30, E-33
		Paralysis or myelitis	CV-A9, CV-B1, CV-B2, CV-B3, CV-B4, CV-B5, CV-B6, E-1, E-2, E-3, E-4, E-5, E-6, E-7, E-9, E-11, E-12, E-13, E-14, E-16, E- 18, E-20, E-21, E-25, E-27, E-29, E-30, E-33, EV-B75, EV-B77, EV-B81, EV-B85, EV-B86, EV-B87, EV-B88, EV-B93, EV- B97, EV-B100
		Meningitis	CV-A9, CV-B1, CV-B2, CV-B3, CV-B4, CV-B5, CV-B6, E-1, E-2, E-3, E-4, E-5, E-6, E-7, E-9, E-11, E-12, E-13, E-14, E-15, E- 16, E-17, E-18, E-19, E-20, E-21, E-24, E-25, E-27, E-29, E-30, E-31, E-32, E-33
		Hand-foot-and-moth disease	CV-A9, CV-B1, CV-B2, CV-B3, CV-B5, E-4, E-9, E-11, E-19, EV-B84
		Upper and lower respiratory diseases	CV-A9, CV-B1, CV-B2, CV-B3, CV-B4, CV-B5, CV-B6, E-1, E-2, E-3, E-4, E-5, E-6, E-7, E-9, E-11, E-12, E-13, E-14, E-15, E- 16, E-17, E-18, E-19, E-20, E-21, E-25, E-29, E-30
		Pleurodynia	CV-A9, CV-B1, CV-B2, CV-B3, CV-B4, CV-B5, CV-B6, E-1, E-2, E-3, E-6, E-7, E-9, E-11, E-12, E-14, E-16, E-17, E-18, E-19, E-24, E-25, E-30
		Herpangina	CV-A9, CV-B1, CV-B2, CV-B3, CV-B4, CV-B5, E-3, E-6, E-9, E-11, E-16, E-17, E-25
		Conjunctivitis	E-7
		Gastroenteritis	CV-A9, CV-B2, CV-B3, CV-B4, CV-B6, E-1, E-6, E-7, E-11, E-13; E-14, E-17, E-18, E-19, E-21, E-24, E-25, E-30, E-32, EV- B84
		Myopericarditis	CV-A9, CV-B1, CV-B2, CV-B3, CV-B4, CV-B5, CV-B6, E-1, E-2, E-3, E-6, E-7, E-9, E-11, E-13, E-16
		Pancreatitis	CV-B1, CV-B2, CV-B3, CV-B4, CV-B5, E-6, E-11, E-30
		Hepatitis	CV-A9, CV-B1, CV-B2, CV-B3, CV-B4, CV-B5, E-3, E-6, E-7, E-9, E-11, E-14, E-17, E-19, E-20, E-25, E-30
		Type I diabetes	CV-A9, CV-B1, CV-B2, CV-B3, CV-B4, CV-B5, CV-B6, E-3, E-4, E-5, E-6, E-9, E-11, E-16, E-18, E-24, E-25, E-30
Human enterovirus C (EV-C)	Poliovirus (PV) Coxsackievirus Enterovirus	Encephalitis	CV-A11, CV-A13, PV-1, PV-2, PV-3
		Paralysis or myelitis	CV-A1, CV-A11, CV-A13, CV-A17, CV-A20, CV-A21, CV-A24, EV-C96, EV-C109, PV-1, PV-2, PV-3
		Meningitis	CV-A11, CV-A13, CV-A17, CV-A19, CV-A22, CV-A24, PV-1, PV-2, PV-3
		Upper and lower respiratory diseases	CV-A21, CV-A24, EV-C104, EV-C109, EV-C117, EC-C118, PV-3
		Pleurodynia	CV-A1
		Herpangina	CV-A1, CV-A19, CV-A22
		Conjunctivitis	CV-A24
		Gastroenteritis	CV-A1, CV-A13, CV-A17, CV-A19, CV-A21, CV-A22
		Myopericarditis	PV-1, PV-3
		Hepatitis	CV-A20
		Type I diabetes	CV-A21, CV-A24, PV-1, PV-2, PV-3
Human enterovirus D (EV-D)		Encephalitis	EV-D68, EV-D70
		Paralysis or myelitis	EV-D68, EV-D70, EV-D94
		Meningitis	EV-D68, EV-D70
		Upper and lower respiratory disease	EV-D68
		Conjunctivitis	EV-D70
		Type I diabetes	EV-D70

Table 1.1.2 Enteroviruses associated diseases

1.1.3 Agent

Enteroviruses, like other members of the family Picornaviridae, are non-enveloped icosahedral particles (~30 nm diameter), with a protein capsid surrounding the naked single-stranded positive (message)-sense RNA genome (~7.5 kb) [9]. The family members show thermal stability between 42°and 50°C in the presence of sulfhydryl reducing agents and magnesium cations in the extracellular environment. But unlike other members, enteroviruses have a slightly lower buoyant density of 1.34g/ml, and better stability at low pH which allows them to survive in the intestine [10].

The enterovirus genome encodes a single open reading frame, which leads to the translation of all viral proteins as a single polyprotein, which is further processed into several protein units including VP1-VP4. The viral capsid, exhibiting pseudo T=3 (truly T=1) icosahedral symmetry [11], is composed of 60 identical protomers. Each protomer consists of four capsid proteins, VP1-4, which are derived from the P1 polyprotein. VP2, VP3, and VP1 have the same topology: they form an eight-stranded anti-parallel β-barrel structure in the form of a wedge that facilitates packing. The topology resembles a β-sandwich “jelly roll” fold and the loops and strands are described according to convention ‘CHEF’ and ‘BIDG’ as shown in Figure 1.1.3.1 The similarity in these protein structures (Fig. 1.1.3.1) has led to the suggestion that they arose by gene duplication [12] and this is the basis of the pseudo T=3 symmetry. The main structural differences between viruses are found in the connecting loops and the C-termini on the outer side of the capsid [13]. VP1 contributes most to the external surface, for VP2 the most prominent surface loop is the “puff” and in VP3, the largest protrusion on the surface is the “knob” [14, 15]. VP4 (the cleaved N-terminus of VP2) is located on the inner surface. The capsid of enteroviruses features a characteristic depression called the "canyon" encircling the 5-fold

axes of symmetry, initially believed to be the binding site for IgG-like picornavirus receptors [16] (Figure 1.1.3.2). Subsequently, several uncoating receptors were found to bind to the canyon [17] [18], although this phenomenon is not universal e.g. SCARB2 binding to EV71 [19]. Beneath the floor of the enterovirus canyon, a lipid molecule known as "pocket factor" binds to VP1 within a hydrophobic pocket. This pocket factor is typically expelled early in the infection process, prior to viral uncoating and particle expansion.

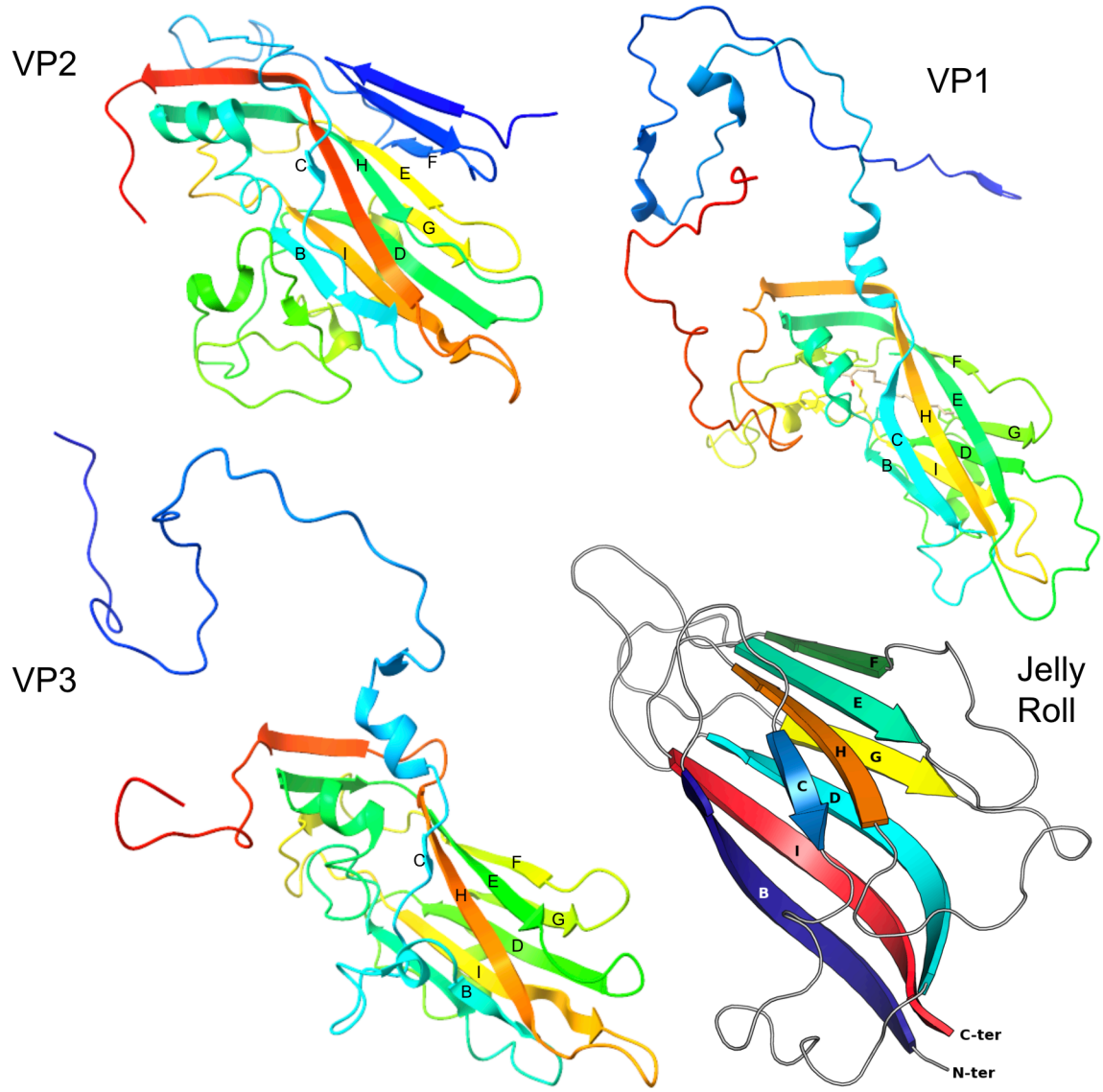


Figure 1.1.3.1 Topology of VP1, VP2, VP3 and the canonical 'Jelly Roll'

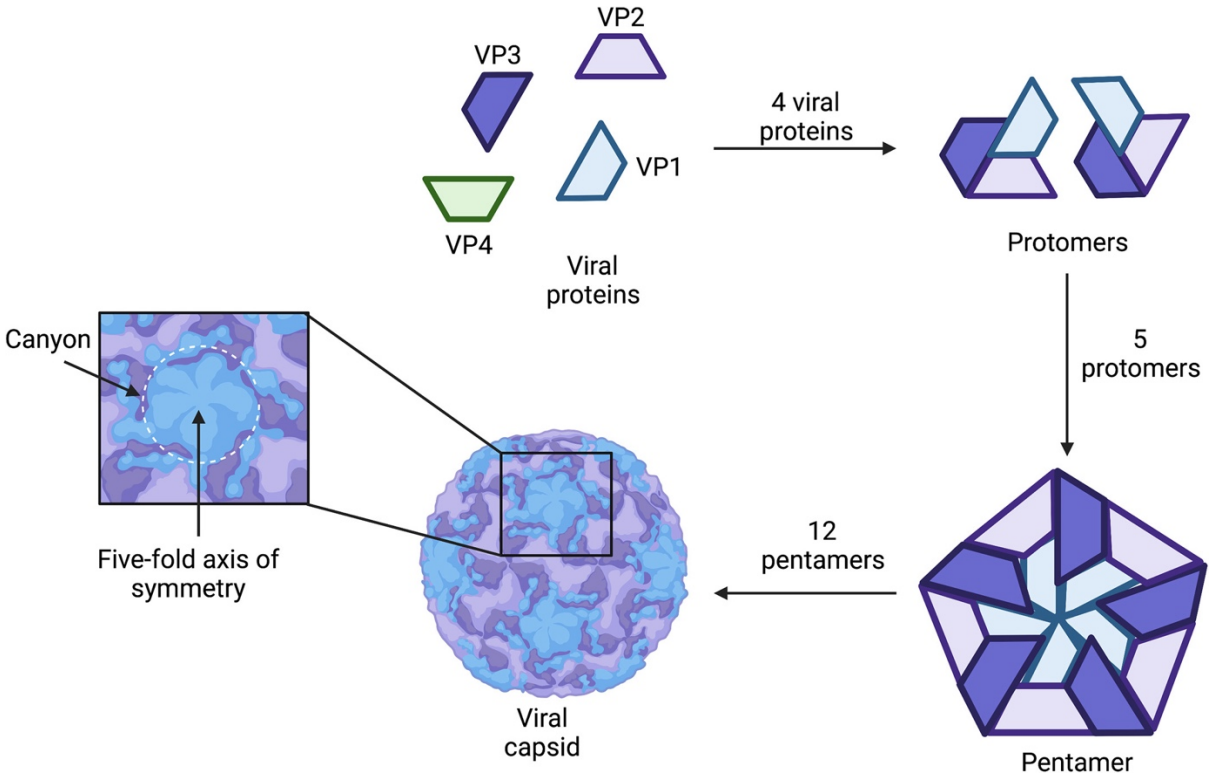


Figure 1.1.3.2 Schematic of enterovirus structure

1.1.4 Traitor

Poliovirus (PV), the first enterovirus to be discovered, has nearly been eradicated worldwide, with only 22 cases reported in 2022. This achievement is primarily due to the extensive global use of the oral PV vaccine. This vaccine utilizes a live-attenuated form of PV, is highly affordable ($0.15 per dose) and easy to administer, making it suitable for less developed countries. However, despite the progress made in eradicating wild-type PV, there have been rare instances (859 cases in 2022 [20]) of circulating vaccine-derived PVs. These vaccine-derived PVs possess similar neurovirulence and transmissibility to the wild-type PVs and arise when the vaccine strains of PV persist in populations with low immunization rates, allowing them to revert to a neurovirulent state [21]. In summary, although the attenuated PV strains were initially seen as human allies in the battle against PV, they betrayed human scientists and contributed to the emergence of vaccine-derived PVs. The war against PV is far from over, and the challenges persist.

1.2 Enterovirus life cycle and immune escape

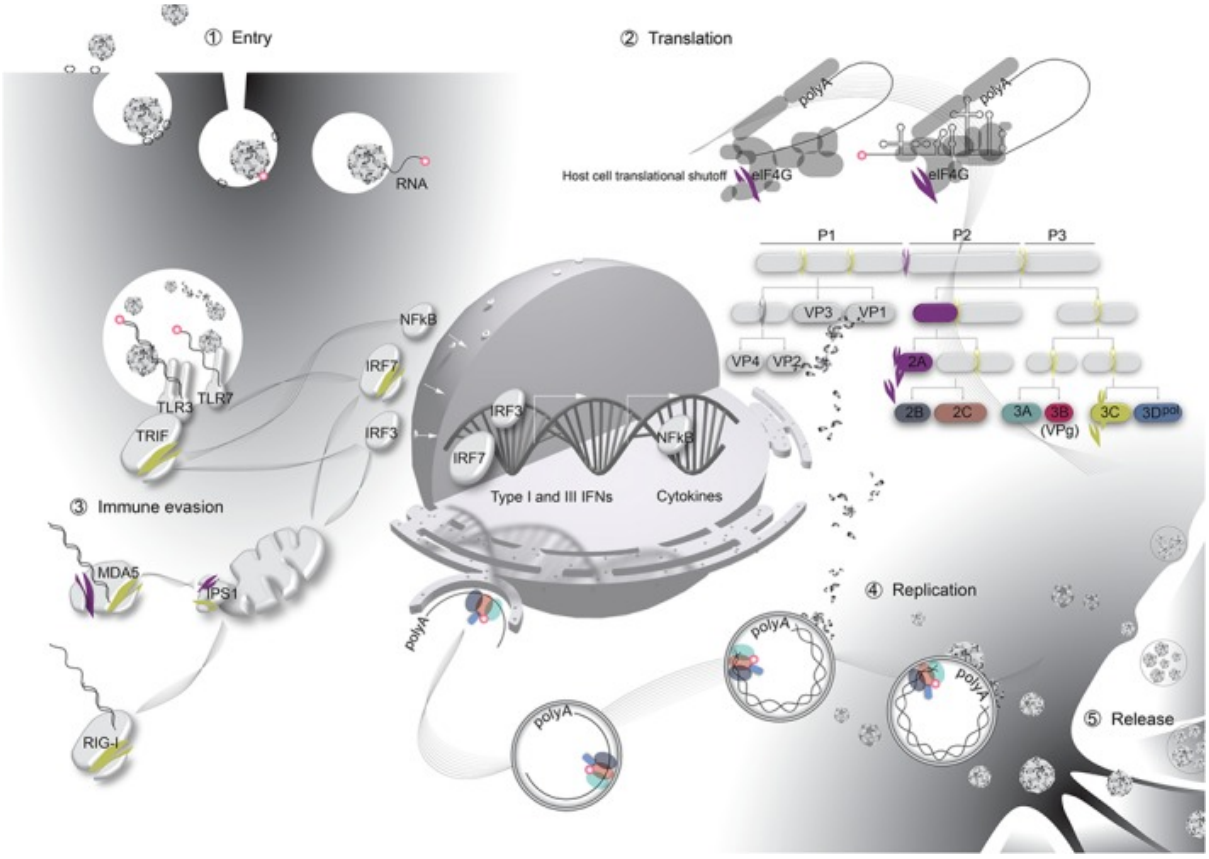


Figure 1.2.0 model of the enterovirus replication cycle. [22]

(1) Entry: After attachment to host cell-surface receptors virus is internalized and uncoated, leading to the release of viral RNA into the cytoplasm.

(2) Translation: Viral polyprotein is translated and then processed by the viral 2A and 3C proteases. Host-cell translation is also abrogated as a component of the translation machinery (eIF4G) cleaved by 2A.

(3) Immune evasion: Host immune responses are blunted by proteolysis mediated by viral proteases 2A and 3C as intracellular receptors (MDA5/RIG-1), and proteins relaying innate signalling (IPS-1) are targeted, blocking the production of interferons and cytokines.

(4) Replication: Viral proteins, in orchestration with host-cell factors, replicate the viral RNA at membrane-associated replication sites.

(5) Viral Release: Enteroviral positive-stranded RNA genomes are encapsidated by the viral structural proteins, and the new viral progeny are released either by cell lysis or in extracellular vesicles.

1.2.1 Virus entry

Enteroviruses utilize various types of cell-surface molecules as attachment factors and uncoating receptors to initiate virus entry into host cells. Many of these known enterovirus receptors are classified as immunoglobulin superfamily (IgSF) [23], specifically the type I transmembrane glycoproteins. This group includes the intracellular adhesion molecule (ICAM-1) [24], the coxsackievirus–adenovirus receptor (CAR) [25], and the poliovirus receptor (PVR) [26]. Additionally, there are non-IgSF type receptors such as decay accelerating factor (DAF), the low-density lipoprotein receptor (LDL-R), scavenger receptor B2 (SCARB2), and integrins [27 28 29 30 31].

The distribution of virus receptors in tissues and cells plays a critical role in determining the tropism of the virus. In the case of polioviruses, their primary target is the human gastrointestinal lymphoid tissues, specifically tonsils and Peyer's patches, which express the poliovirus receptor (PVR) [32 33]. When the virus gains access to the bloodstream and subsequently reaches the central nervous system, it can infect neuronal cells that also express PVR. This infection of neuronal cells can lead to symptoms such as muscle weakness and paralysis.

Through their attachment to cell-surface receptors, enteroviruses gain access into the cell via endocytic pathways. The specific route of entry depends on the virus species and the type of cell involved. Several mechanisms have been identified, including caveolae-dependent [34], clathrin-dependent [35], and other internalization pathways [36]. However, the presence of a receptor on the cell surface alone does not guarantee viral replication within the cell. Factors such as the availability of endogenous cellular proteins are necessary for viral propagation can determine whether the virus successfully replicates. For example, the polypyrimidine tract-binding protein (PTB) is an endogenous

protein that plays a role in viral replication [37]. PTB functions mainly as a splicing regulator, but it also functions in alternative 3' end processing, mRNA stability and RNA localization [38]. Additionally, a receptor-expressing cell can enter an antiviral state, rendering it non-permissive to infection [39]. Therefore, host susceptibility and permissiveness to viral infection are influenced by a complex interplay of various cellular factors, making it a multifaceted phenomenon.

Virus	Receptor	Attachment factor
Coxsackie A viruses	ICAM-1	DAF
	SCARB2	MHC-1 associated GRP78
	KREMEN1	Sialic acid
		Heparan sulfate
		PSGL-1
Coxsackie A9		αVβ3 and αVβ6 integrins
Coxsackie B viruses	CAR	Decay accelerating factor (DAF, CD55)
		Heparan sulfate
Echoviruses	Neonatal Fc receptor (FcRN)	DAF/CD55
		Integrin α2β1, integrin αvβ3
		Heparan sulfate
Enterovirus 68	ICAM-5	Sialic acid
Enterovirus 70		DAF
		Sialic acid
Enterovirus 71	SCARB2	PSGL-1
		Heparan sulfate
		Vimentin
		Nucleolin
		Annexin II
Parechoviruses		Heparan sulfate
		Integrin avb3, avb1, avb6
Poliovirus	PVR (CD155)	
Rhinovirus (major group)	ICAM-1	
Rhinovirus (major group)	LDL receptor	
Rhinovirus C	CDHR3	

Table 1.2.1 Categorization of receptor and attachment factors of some enteroviruses

1.2.2 Translation and Replication

Following endocytosis, the virus particle undergoes structural changes, leading to the uncoating of the viral genome. During this process, the capsid proteins interact with the endosomal membrane, likely facilitated by the N-terminus of VP1 and VP4. This allows the delivery of viral RNA with a 5′-linked VPg protein [40] and a 3′-polyadenylated tract [41] into the cytosol, where it is translated by the host ribosomes into the viral polyprotein.

The polyprotein encoded by a single open reading frame is divided into three regions: P1, P2, and P3. The P1 region consists of four structural proteins (VP1-VP4), while the P2 and P3 regions collectively contain seven non-structural proteins (2A-2C and 3A-3D). These non-structural proteins play essential roles in various stages of the virus replication cycle. The cleavage of the polyprotein into individual proteins begins during translation and is mediated by viral proteases, specifically 2A and 3C proteases [42] [43] [44].

During translation, the P1 region which encodes the structural proteins of the capsid is the first to be translated. It is followed by the P2 region, which contains three non-structural proteins (2A, 2B, and 2C). 2A is translated first and undergoes an in-cis cleavage, separating itself and the P2 region from the P1 region before the full polyprotein has been translated.

Translation then proceeds through the P3 region, which includes the second protease, 3C. This protease is responsible for eight out of the ten cleavages of the viral polyprotein. The cleavage events carried out by the two proteases generate all the non-structural proteins, along with several precursor proteins. Additionally, three structural proteins are formed: VP1, VP3, and VP0.

VP0, one of the structural proteins, is further cleaved into VP2 and VP4 [45]. The exact mechanism of this cleavage is not fully understood and is believed to involve an unknown process, potentially an RNA-mediated autocatalytic reaction, during the encapsidation process [46].

Viral replication occurs in close proximity to membranous vesicles, which are partially derived from the endoplasmic reticulum [47]. During replication, the positive strand RNA genome is replicated by the viral polymerase 3D into a complementary negative strand RNA. RNA synthesis is a protein-primed mechanism. The RNA polymerase links two UMPs to a tyrosine in VPg (3B), the terminal protein. A conserved sequence in the loop of a *cre* element acts as the template for the linkage of the UMPs to VPg to produce VPgpUpU which acts as the primer for the elongation of the RNA chains by 3D. A 'slide-back' mechanism is used to ensure the integrity of the genome ends [48].

The negative strand RNA then serves as a template for the transcription of the positive strand RNA genome. From a single negative-strand template, multiple positive-strand RNAs can be synthesized. This abundance of positive-sense RNA allows for direct availability for translation, synthesis of additional negative-sense RNA, and encapsidation [49].

1.2.3 Encapsidation and virus release

During viral replication, newly synthesized viral RNA and structural proteins accumulate, leading to the packaging of the viral genome into capsids and the formation of new viral progeny [15]. However, the process of encapsidation, or how the genome is precisely packaged into the capsids, remains poorly understood. Some studies have suggested that the assembly of the virus is linked to RNA synthesis [50] and occurs on the surface of cytoplasmic membranes [51].

Traditionally, it was believed that enteroviruses are released through cell lysis, where the infected cell ruptures, releasing the viral particles. However, recent observations challenge this model. It has been discovered that host cells can release virus-containing extracellular vesicles, which could potentially disseminate the infection [52] [53]. This sheds new light on the mode of enterovirus release.

Moreover, there have been reports of persistent enterovirus infections in tissues and cell models where there is no apparent cytopathic effect. These observations provide further support for the nonlytic model of virus release, suggesting that enteroviruses can be released from infected cells without causing cell lysis [54] [55] [56].

1.2.4 Immune escape

The immune system comprises innate immunity and acquired immunity, serving as a crucial defence system against the intrusion of harmful microorganisms while surveilling and eliminating foreign entities. During the early stage of infection the virus to rapidly proliferates within the respiratory system and spreads to its natural infection site [57]. To evade the humoral immune response, enteroviruses demonstrate a propensity for antigenic variation, enabling the virus to evade neutralizing antibodies, leading to multiple serotypes [58]. Ongoing antigenic drift can be detected for viruses such as EV71, which causes widespread outbreaks in South East Asia, with is evidence for ongoing selection of variants in the face of herd immunity [59]. Furthermore, enterovirus infection hampers the cellular immune response by reducing host lymphocytes, leading to severe viremia and eventual destruction of T cells. Moreover, enteroviruses inhibit the function of dendritic cells, impairing their ability to process antigens [60] [61]. Previous studies have indicated that major histocompatibility complex class I (MHC-I) molecule expression on infected cells diminishes within 30 minutes of enterovirus infection, thereby compromising the cells' capacity to present MHC-I-associated viral peptides to T lymphocytes [61]. This mechanism aids the virus in evading the host's cytotoxic immune response.

Another important immune evasion strategy employed by enteroviruses involves limiting the cytotoxic effect mediated by natural killer (NK) cells. Studies have shown a significant decline in porcine NK cell responsiveness 2-3 days post enterovirus infection, although it eventually returns to normal [62]. Extensive research has been conducted on the interference of enterovirus with immune responses and suppression of innate immunity. Certain enterovirus proteins ($L^{protease}$, 2B, 3A, 3B, 3C) can directly or indirectly target retinoic acid-induced gene I like receptors to inhibit innate immunity [63 64 65 66 67]. Enterovirus proteins VP0, VP3, 3A, and 3B reduce the expression of the junction protein virus-induced signalling adapter at the transcriptional or protein level [63 68 69]. Enterovirus proteins $L^{protease}$, VP0, VP1, 2B, and 3A can inhibit interferon production [63 70 71 65]. VP3 and 3C proteins inhibit the JAK-STAT signalling pathway, consequently suppressing the production of interferon-stimulated genes [72 73]. Additionally, enterovirus proteins $L^{protease}$ and 3C hinder the synthesis of antiviral molecules by cleaving host transcription and translation factors [74 75 76 77 78]. Enterovirus proteins VP2 and 2C facilitate virus replication by modulating autophagy [79 80]. These mechanisms provide opportunities for enteroviruses to undergo rapid transcription and translation processes.

1.3 Structure facilitated drug design

Due to the continuing outbreak of Enterovirus A71 in the Asian-Pacific region [81] in the last decade, extensive research has been focussed on antiviral compounds against this virus. Because of the similarity in gene sequence among enteroviruses (> 75% nucleotide and >85% amino acid sequence similarity [82]), certain EV71 inhibitors show therapeutic activity against other enteroviruses (Table 1.3.1).

Inhibitor	Remark	Inhibited	Not inhibited
Capsid inhibitors			
Pleconaril	Activity against EV-A71 is controversial Dropped out of clinical trial for rhinovirus infection	EV-D68, RV-87, RV-A, RV-B	PV-1, RV-B17, RV-A45, RV-C
Vapendavir	Dropped out of clinical trial for rhinovirus infection	EV-A71. EV-C, RV-A, RV-B	EV-D68
Pirodavir	Dropped out of clinical trial for rhinovirus infection	EV-A71, EV-D68, EV-A, EV-B, EV-C, EV-D, RV-A, RV-B	RV-A8, RV-A25, RV-A45, RV-87, RV-C
PR66	*In vivo* antiviral efficacy against EV-A71 in mice	EV-A71	EV-D68, CV-A16, CV-B1, CV-B2, CV-B3, Echovirus 9, rhinovirus
NLD-22	Favorable PK properties *In vivo* antiviral efficacy against EV-A71 in mice	EV-A71	–
VP1-14	Favorable PK properties *In vivo* antiviral efficacy against EV-A71 in mice	EV-A71	–
ICA135	*In vivo* antiviral efficacy against CV-A10 in mice	CV-A10, EV-A71, CV-A16, CV-B3, PV-1, EV-D68	–
CB-30	Binds to the five-fold axis of the EV-A71 capsid	EV-A71, HIV-1, HIV-2	–
Suramin	Polypharmacology *In vivo* antiviral efficacy against EV-A71 in mice and rhesus monkeys	EV-A71, CV-A2, CV-A3, CV-A10, CV-A12, CV-A16, CV-A9, ECHO25	ECHO20, PV1-3, EV-D68
Brilliant black BN (E151)	Binds to the five-fold axis of the EV-A71 capsid *In vivo* antiviral efficacy against EV-A71 in mice	EV-A71, CV-A16, CV-A6	CV-A4, CV-A10
2C inhibitor			
(*S*)-Fluoxetine	Lack of efficacy against EV-D68 in clinical trials (*S*)-enantiomer is more active	CV-B3, EV-D68, HRV-A2, HRV-B14	EV-A71, PV-1
2C-12b	Analog of fluoxetine	EV-A71, EV-D68, CV-B3, PV-1, CV-A24, HRV-A2, HRV-B14	–
Dibucaine	Identified through drug repurposing	EV-A71, EV-D68, CV-B3	PV-11, RV-A2, RV-B14
2C-12a	Dibucaine analog; Did not inhibit Na^+ channel	EV-D68	–
JX040	Derived from a HTS hit	CV-B3, EV-A71, PV-1	–
2C-7d	Derived from a HTS hit	EV-A71, EV-D68, CV-B3	–
3A protein inhibitor			
Enviroxime	Failed in phase II trial for rhinovirus infection; PI4KIIIβ was also suggested as the drug target	PV1-3, RV14, RV16, CA21, CB3, RV-87, EV-A71, EV-D68	–
Itraconazole	Mutations in 3A confer drug resistance; OSBP was also suggested as the drug target	EV-A71, CV-A16, CV-B3, PV-1, HRV14, EV-D68	Equine rhinitis A virus
3Cpro inhibitor			
Rupintrivir	Failed in phase II trial for rhinovirus infection	EV-A71, CV-A16, EV-D68, RV-87, norovirus, human rhinoviruses	SARS-CoV-2
GC-376	Veterinary drug candidate for FIPV infection in cats	EV-A71, EV-D68, HRV18, HRV51, HRV68	–
3Dpol inhibitor			
Gemcitabine	Identified through drug repurposing; Synergistic effect with interferon-β	EV-A71, EV-D68, CV-B3, CV-A6, CV-A16, E-7, PV-1, DENV, CHIKV	–
Sofosbuvir	*In vivo* antiviral efficacy against EV-A71 in mice	EV-A71	–
FNC	HIV clinical candidate	EV-A71, CV-A16, CV-A6, EV-D68, CV-B3	–
Favipiravir (T-705)	Synergistic effect with suramin	EV-A71, EV-D68 (not all subtypes)	–
NITD008	Failed in clinical trial for flavivirus infection	EV-A71	–
IRES inhibitor			
DMA-135	Binds to the IRES stem loop 2	EV-A71	–
Prunin	Mutations in IRES confer drug resistance; *In vivo* antiviral efficacy against EV-A71 infection in mice	EV-A71	–
Emetine	*In vivo* antiviral efficacy against EV-A71 infection in mice	EV-A71, CV-A16, CV-B1, EV-D68, Echovirus 6	–
Host-targeting antivirals			
OSW-1	Decreases OSBP level	EV-A71, CV-B3, CV-A21, RV-B14	–
MDL-860	Allosteric inhibitor of PI4KB	RV-1, RV-2, RV-8, RV-64, PV-2, EV-A71, EV-D68	–
RYL-634	DHODH inhibitor	HCV, DENV, ZIKV, CHIV, EV-A71, HIV, RSV	–

Table 1.3.1 selected EV71 antivirals with translational potential [83]

1.3.1 Antivirals preventing enterovirus cell entry

Pocket factor

Capsid binders are extensively studied antiviral compounds that block virion uncoating by replacing the pocket factor in the canyon [84] [85]. Inhibitors bind to the hydrophobic pocket of VP1 with higher affinity than the lipid pocket factor and therefore cannot be released upon receptor binding [86]. They function as molecular glue that effectively hinders the uncoating of the viral capsid proteins.

The most advanced enterovirus capsid inhibitors are derived from the WIN series of compounds such as Pleconaril [87]. Pleconaril was tested in a trial for the treatment of neonates with enterovirus sepsis, showing improved survival rates among recipients of pleconaril [88]. However, a significant drawback of capsid binders is the rapid emergence of resistance. In a clinical trial for the treatment of rhinovirus infections using pleconaril, viruses resistant to the compound were isolated [89]. Furthermore, naturally occurring pleconaril-resistant viruses, such as an echovirus 11 strain, have been reported [90]. It is also controversial whether pleconaril is active against EV71 [91]. These issues with resistance complicate the use of capsid binders in clinical settings.

The United States Food and Drug Administration (FDA) rejected pleconaril as a potential drug candidate for treating rhinoviruses due to concerns over its side effects, including menstrual irregularity and drug resistance [92]. However, during structure-activity relationship studies, an imidazolidinone derivative called PR66 was identified as a potent antiviral against EV71 [93]. Two structural analogues of PR66, namely NLD and ALD, were discovered to inhibit EV71 replication with impressive potency. Their IC50 values were measured at 0.025 and 8.54 nmol/L, respectively, making them the most potent EV71 inhibitors reported thus far [94]. Their function of replacing the pocket factor is confirmed thanks to high-resolution structure solved by x-ray crystallography and cryo-EM (PDB code: 4CEY, 4CEW, 6LQD). Besides that, many other antiviral compounds are under clinical trials (Figure 1.3.1.1)

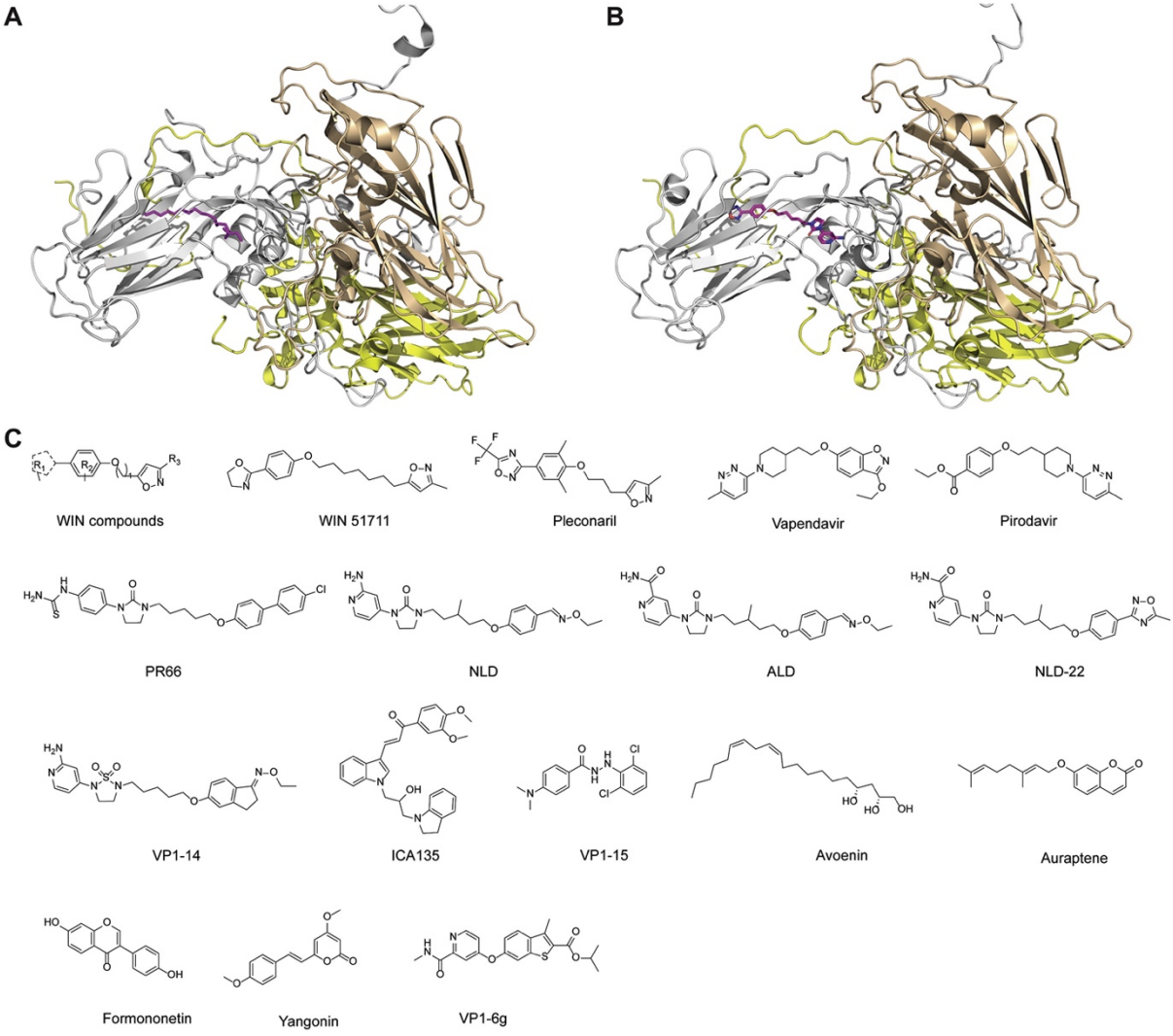


Figure 1.3.1.1 EV71 capsid inhibitors targeting the VP1 hydrophobic pocket. (A) Cryo-EM structure of EV71 capsid proteins in complex with sphingosine (PDB: 6UH6). (B) NLD-22 (PDB: 6LQD). VP1, VP2, VP3, and NLD-22 were coloured in grey, tint, yellow, and magenta, respectively. (C) Chemical structures of EV71 capsid inhibitors targeting the VP1 hydrophobic pocket.

5-fold axis

Another class of antivirals interact with the VP1 amino acid residues proximal to the five-fold axis of the enterovirus capsid and function by blocking the virus receptor and/or attachment factors from binding the virus (Figure 1.3.1.2). Dendrimers (highly ordered, branched polymeric molecules), such as MADL385 and a simplified version CB30, have been proven to prevent EV71 from interacting with its cellular co-receptors: P-selectin glycoprotein ligand-1 (PSGL1) and heparan sulfate (PDB code: 6DIZ, 6UH7). A natural product rosmarinic acid (RA) was found to inhibit multiple strains of EV71 but not EV-D68, and it has a stronger antiviral efficacy *in vivo* than *in vitro* suggesting an unknown mechanism is involved [95]. Suramin, an FDA-approved pediatric antiparasitic drug, was found to inhibit virus entry with an elusive mechanism, but its analogs NF449, NF110 and NM16 clearly inhibits receptor attachment in a similar way to the dendrimers. Brilliant Black BN (E151), a sulfonated food azo dye, was identified to inhibit EV-A71, CV-A16, and CV-A6 replication in cell culture, as sulfonated compounds can function as mimics of sulfated glycosaminoglycans, which are attachment factors and/or receptors of many enteroviruses [96].

Capsid inhibitors offer the advantage of high potency, typically ranging from nanomolar to picomolar concentrations (nmol/L to pmol/L). However, capsid inhibitors normally exhibit a low genetic barrier to drug resistance, meaning that the viruses can develop resistance to them relatively easily. Additionally, the antiviral activity of capsid inhibitors is often restricted to specific subtypes of enteroviruses. As of now, there have been no reports of broad-spectrum capsid inhibitors that can effectively target a wide range of enterovirus subtypes [97].

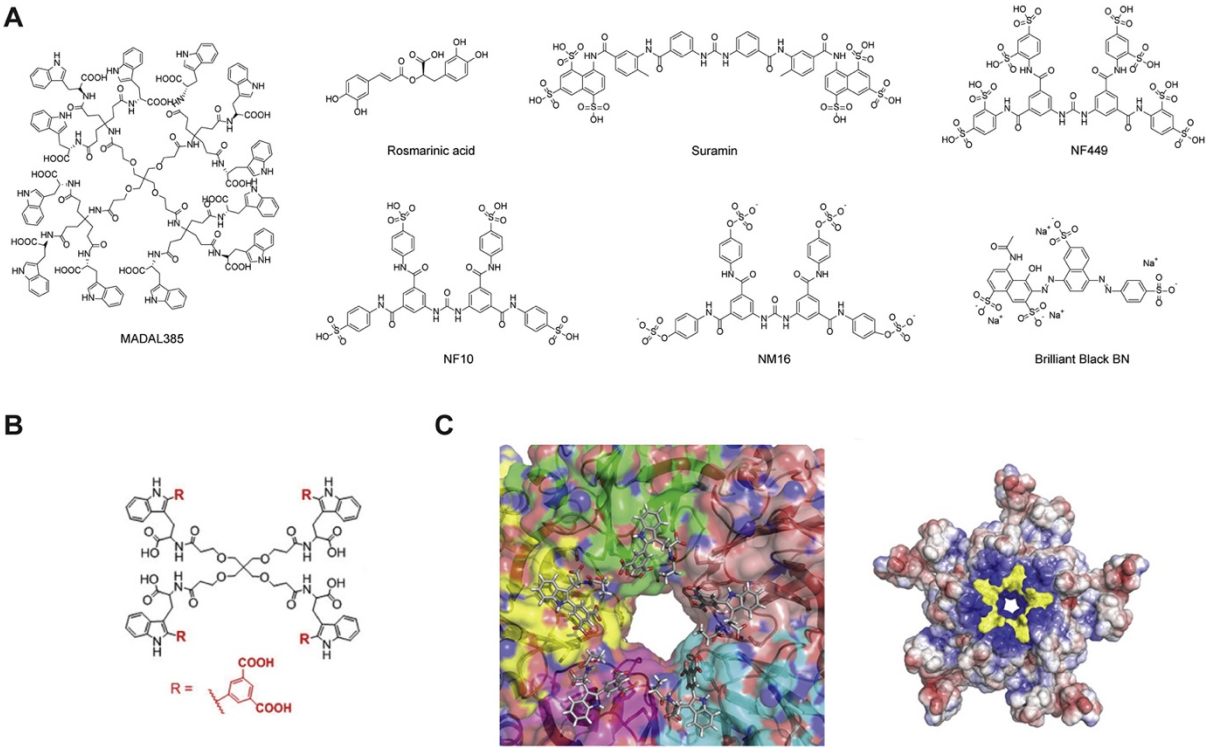


Fig 1.3.1.2 EV71 antivirals targeting the 5-fold axis of the capsid proteins. (A) Chemical structure of EV71 capsid inhibitors targeting the 5-fold axis of the capsid proteins. (B) Chemical structure of CB-30. (C) Binding pose of EV71 capsid inhibitor CB-30 (compound 30 in the original publication) [98].

1.3.2 Antivirals preventing enterovirus replication

Non-structural proteins of enteroviruses (2A protease, 2C, 3A, 3C protease and 3D polymerase) perform some crucial steps in the virus replication process, are therefore good targets for antiviral drug design and have been extensively studied.

2A and 3C protease

The role of 2A protease and 3C protease in both cleavage of the viral polyprotein and assisting immune escape have been described in the previous section. In comparison to 3C protease, 2A protease remains a relatively unexplored drug target, with CV33 [99] and a peptide-based inhibitor Z-LVLQTM-FMK [100] showing weak inhibitory activities against EV71. In another study, a library of 32 lycorine derivatives was screened against EV71 and 1-acetyllycorine stands out to be the most potent hit, but the exact mechanism of action remains elusive [101]. An X-ray crystal structure of the EV71 2A mutant was solved, paving the way for structure-based drug design or virtual screening [101].

The 3C or 3C-like protease demonstrates a strong preference for glutamine at the P1 position when it comes to substrates. As a result, the majority of inhibitors targeting the 3C protease are designed to incorporate a pyrrolidone at the P1 position, acting as a mimic for the substrate. These inhibitors typically consist of di-, tri-, or tetra-peptides linked to a 'reactive warhead'. Reactive warheads commonly utilized include aldehyde, ketoamide, and α,β-unsaturated ester. The aldehyde warhead can also be transformed into bisulfide and cyanohydrin prodrugs [102]. Several X-ray crystal structures have been resolved, depicting the complex formation between the EV71 3C protease and inhibitors such as rupintrivir [101], 3C-18p [103], and 3C-4 [104]. These structures reveal the formation of a covalent bond between the catalytic residue C147 and the inhibitor (Figure 1.3.2.2).

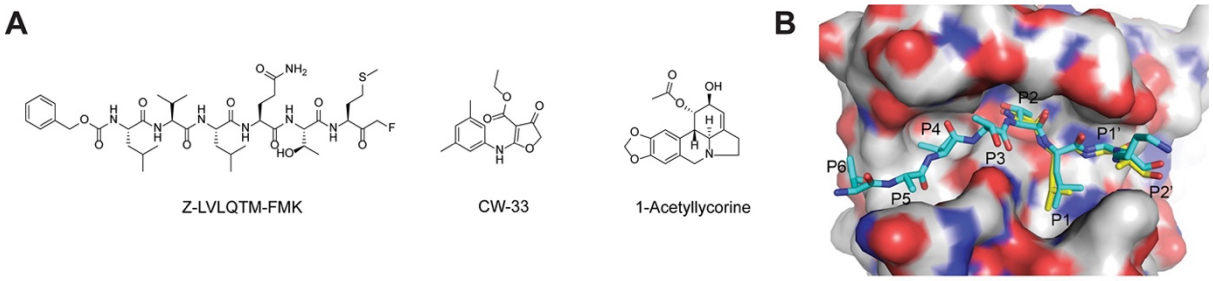


Figure 1.3.2.1 EV71 2A protease inhibitors. (A) Chemical structure of the EV71 2Apro inhibitors. (B) Modeling of the substrate peptide on the X-ray crystal structure of EV71 2Apro C110A mutant (PDB: 4FVB)

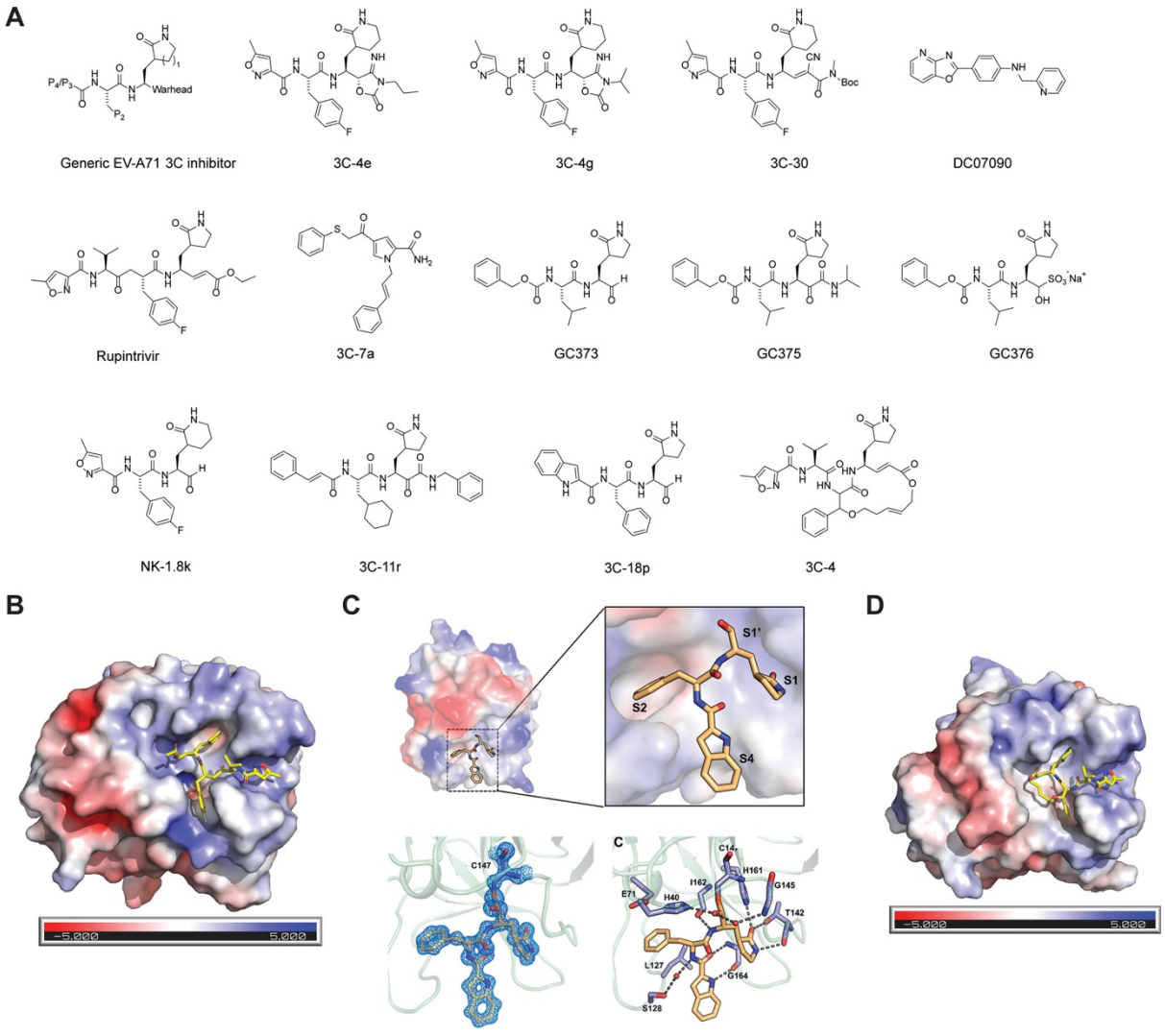


Figure 1.3.2.2 EV71 3C inhibitors. (A) Chemical structures of EV71 3Cpro inhibitors. (B) X-ray crystal structure of EV71 3Cpro in complex with rupintrivir (AG7088) (PDB: 3SJO). (C) X-ray crystal structure of EV71 3Cpro in complex with 3C-18p (PDB: 7DNC). (D) X-ray crystal structure of EV71 3Cpro in complex with macrocyclic inhibitor 3C-4 (PDB: 6LKA).

2C protein

The 2C protein is a multifunctional protein and its known functions include viral uncoating, membrane remodelling, RNA binding and replication, and encapsidation [105], but the detailed mechanism is yet to be elucidated. The enterovirus 2C protein was reported to have ATP-dependent RNA helicase and ATP-independent chaperoning activities [106], which makes it a high-profile antiviral drug target.

The X-ray crystal structure of a soluble portion of EV71 2C (residues 116−329) was resolved at a 2.5 Å resolution (Figure 1.3.2.3 A). This 2C protein comprises an adenosine triphosphatase (ATPase) domain, a cysteine-rich zinc finger, and a C-terminal helical domain. The C-terminal helical domain plays a crucial role in oligomerization, as it binds to a concave pocket formed between the ATPase and zinc finger domains of a neighbouring monomer. Functional studies have demonstrated that this oligomerization is vital for 2C ATPase activity and essential for EV71 viral replication [107].

Cryo-EM and X-ray crystal structures showed that (S)-fluoxetine binds to the allosteric site in the coxsackievirus-B3 2C (Figure 1.3.2.3 B and C), and drug binding stabilizes the 2C hexamer. Drug-resistant mutations are mapped to both the (S)-fluoxetine binding site (C179F, C179Y and F190L) and the 224-AGSINA-229 loop (A224V, I227V, and A229V). The 224-AGSINA-229 loop is located downstream of the Walker C motif and does not directly interact with (S)-fluoxetine. It was proposed that the 224-AGSINA-229 loop stabilizes the Walker B-containing loop in an “open conformation” suitable for (S)-fluoxetine binding.

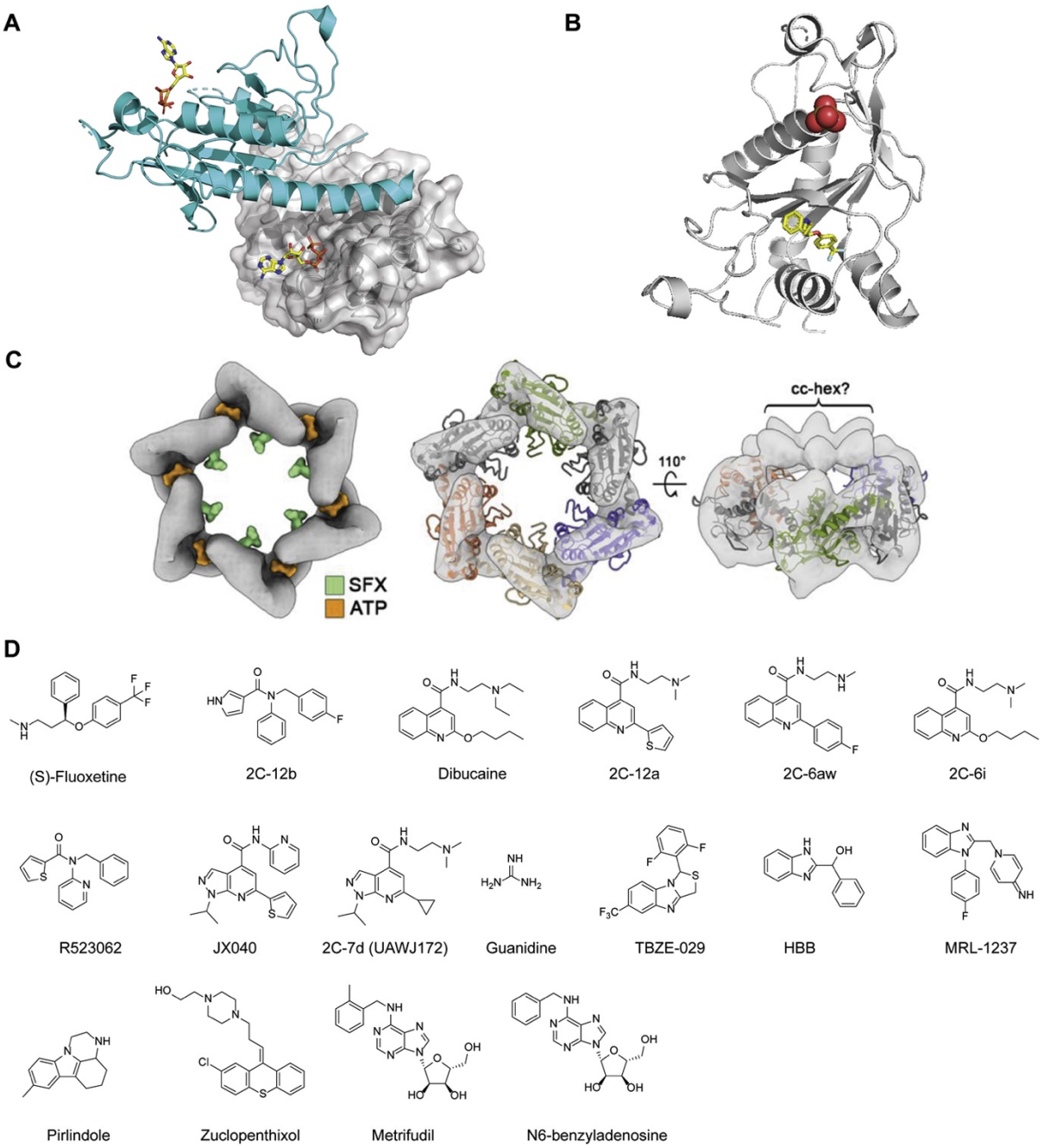


Figure 1.3.2.3 EV71 2C inhibitors. (A) X-ray crystal structure of EV71 2C protein (PDB: 5GRB). One monomer is coloured in cyan, and another monomer is coloured in grey and shown as a surface. ATP is shown in sticks. (B) X-ray crystal structure of coxsackievirus-B3 2C (117-329) in complex with (S)-fluoxetine (PDB: 6T3W). (C) Cryo-electron density maps of coxsackievirus-B3 2C with (S)-fluoxetine and ATP [108]. (D) Structurally diverse inhibitors all target EV71 2C protein.

3A protein

The replication complex of enteroviruses resides in replication organelles, which are formed by hijacking host lipid homeostasis pathways [109]. The formation of these organelles depends on essential components such as the viral 3A protein, host phosphatidylinositol 4-kinase IIIβ (PI4KB), acyl-coenzyme A binding domain containing 3 (ACBD3), and oxysterol-binding protein (OSBP) [109] [108]. Increased interactions between PI4KB and ACBD3 are observed upon overexpression of the 3A protein or during EV71 infection. Co-localization of viral 3A, PI4KB, and ACBD3 occurs at the replication organelles, where viral RNA replication takes place, and direct interaction between 3A and ACBD3 is confirmed (Figure 1.3.2.4 A). Mutations in the 3A protein (I44A and H54Y) disrupt the PI4KB–ACBD3 interaction. Recent research highlights ACBD3's essential role in mediating 3A-PI4KB interactions [110].

X-ray crystal structures of the C-terminal Golgi-dynamics domain (GOLD) of ACBD3 in complex with the 3A protein from various enteroviruses, including EV71, PV1, EV-D68, and rhinovirus-B14, have been resolved (PDBs: 6HLW, 6HLV, 6HLN, and 6HLT) (Fig. 1.3.2.4 B) [111]. These structures exhibit high similarity, suggesting that diverse enteroviruses employ a conserved mechanism to recruit the host ACBD3 protein to the Golgi.

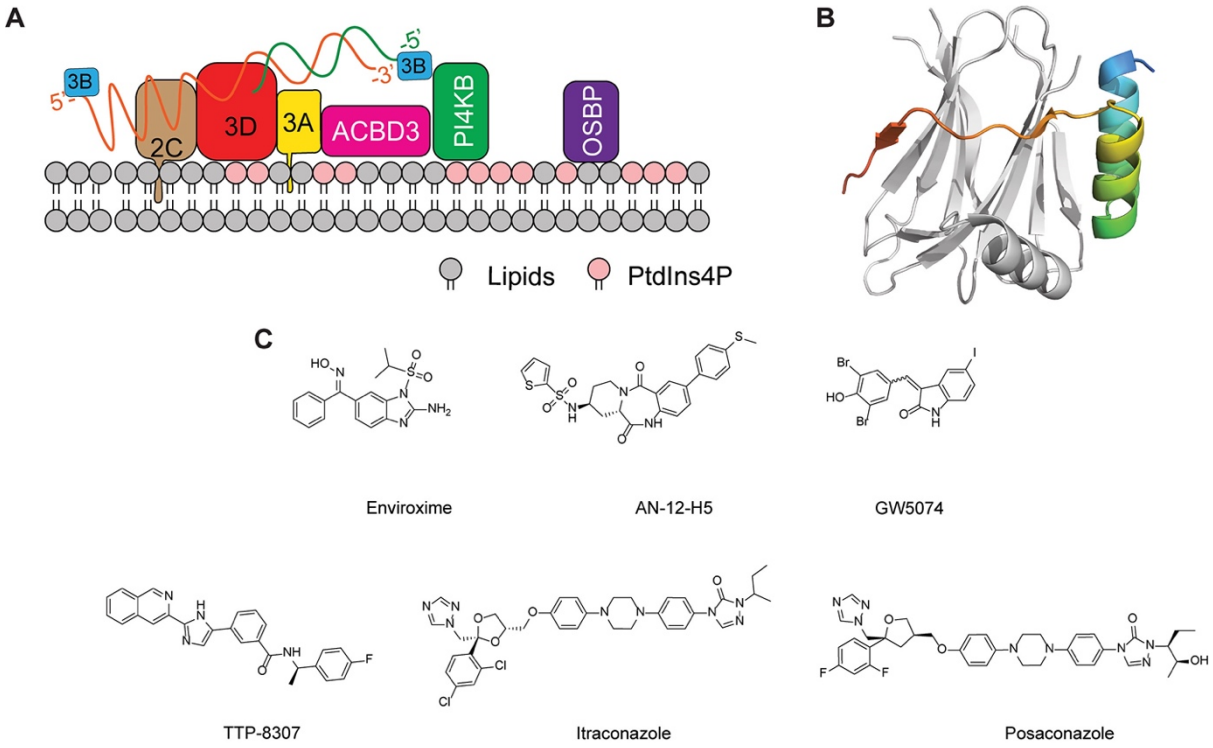


Figure 1.3.2.4. EV71 3A structure and inhibitors. (A) Model of the EV71 3A protein and the associated proteins in the replication organelle. (B) X-ray crystal structure of the C-terminal Golgi-dynamics domain (GOLD) of ACBD3 in complex with the cytoplasmic domain of the EV71 3A protein (PDB: 6HLW). The ACBD3 and 3A proteins are coloured in grey and rainbow, respectively. (C) Chemical structure of EV71 3A inhibitors. [83]

3D polymerase

Enterovirus 3D polymerase serves as an RNA-dependent RNA polymerase responsible for viral RNA synthesis. The majority of FDA-approved viral polymerase inhibitors are nucleoside or nucleotide analogs that can act as polymerase inhibitors, chain terminators, or mutagens once they are incorporated into viral RNA or DNA [112 113]. GPC-N114, cited as a potent non-nucleoside inhibitor, exhibits broad-spectrum antiviral effects against enteroviruses and cardioviruses [114]. Mechanistic confirmation occurred via an *in vitro* polymerase assay, revealing GPC-N114's inhibition of RNA elongation catalysed by CV-B3 3D polymerase. The co-crystal structure of CV-B3 3D polymerase complexed with GPC-N114 indicated binding in the RNA-binding channel (Figure 1.3.2.5).

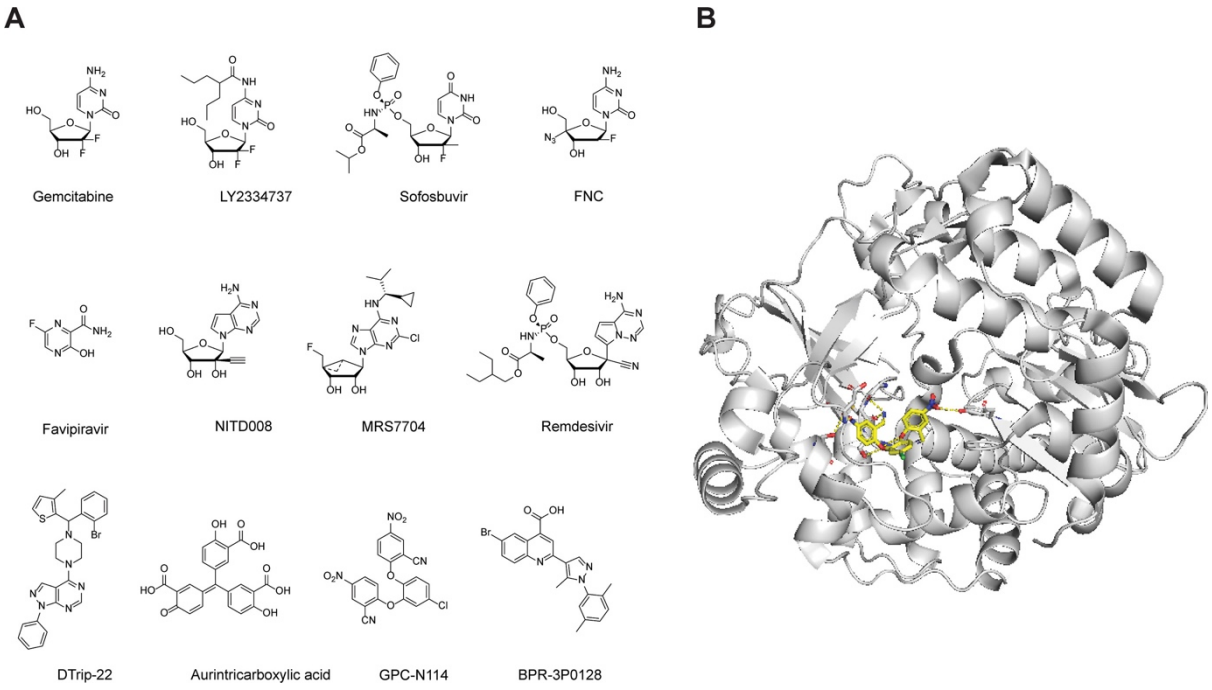


Figure 1.3.2.5 EV71 3D polymerase inhibitors. (A) Chemical structures of EV71 3D polymerase inhibitors. [83] (B) X-ray crystal structure of CV-B3 3D-polymerase in complex with GPC-N114 (PDB: 4Y2A).

Internal Ribosomal Entry Site (IRES)

Enterovirus, like other eukaryotic viruses, manipulate the host's translational machinery for viral protein synthesis. However, unlike the host's cap-dependent translation, the enterovirus's viral genome lacks the 5′ cap, initiating translation through an (IRES)-mediated, cap-independent mechanism [115]. This IRES is found in the 5′ UTR of enterovirus mRNA and contains four domains. Among these, the stem loop II plays a crucial role in viral replication, making it an attractive drug target. Most of the IRES-targeting inhibitors are natural products and some are used in humans, making them ideal candidates for a combination therapy. Screening a focused library of RNA-targeting compounds using the peptide-displacement assay led to the discovery of DMA-135, a potent IRES inhibitor [116]. The solution NMR structure of IRES stem loop 2 in complex with DMA-135 was resolved (Figure 1.3.2.6). The binding of DMA-135 to IRES stem loop 2 induces a conformational change that stabilizes the ternary complex with the AU-rich binding factor, ultimately suppressing translation.

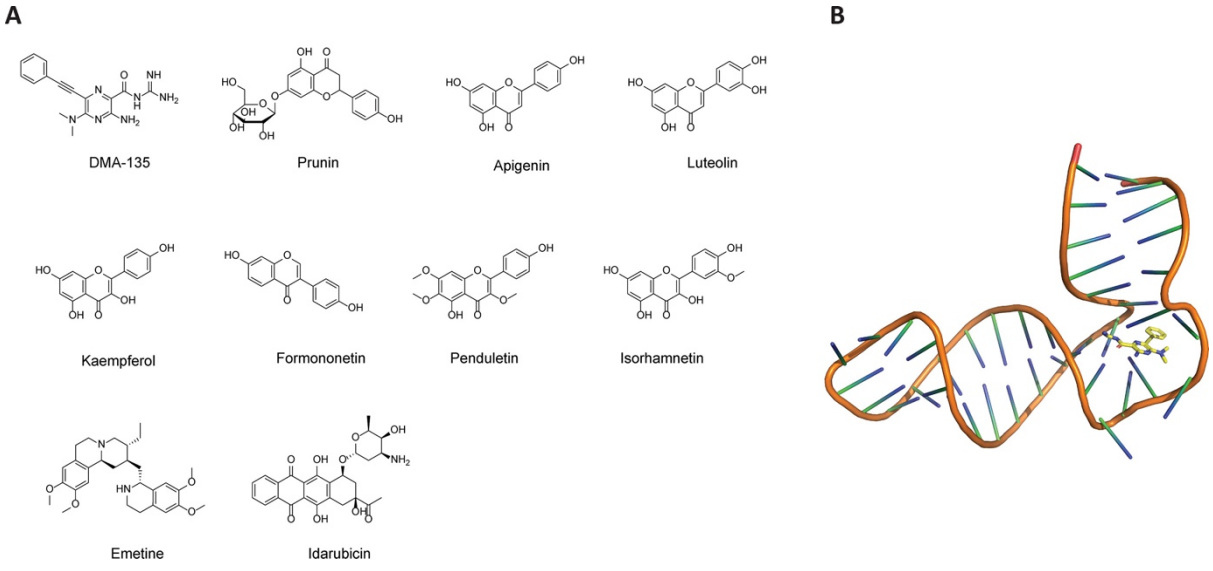


Figure 1.3.2.6 EV71 IRES inhibitors. (A) Chemical structures of EV71 IRES inhibitors. [83] (B) Solution NMR structure of EV71 IRES in complex with DMA-135 (PDB: 6XB7).

In summary

Antivirals that prevent enterovirus replication normally offer broad-spectrum and potent antiviral activity, but the potential off-target effects may cause unwanted side-effects on the host. Overall, the creation of inhibitors against these targets is a high risk and high reward strategy.

1.3.3 Antivirals targeting other proteins

The enteroviral protein 3B (VPg) serves as a primer for viral genome replication, which takes place on the surface of membranous vesicles [117]. When expressed in xenopus oocyte, the enteroviral protein 3B forms an ion channel that selectively conducts chloride ion [118], rendering it a putative member of the viroporin family [119]. 3B proteins are relatively less studied and currently no reliable results of antiviral activity have been published.

Enteroviruses, as obligate intracellular parasites, exploit host proteins and signalling pathways for their replication. Targeting host factors without interfering the host provides a promising avenue for developing antivirals. Several methods, such as siRNA, proteomics, and insertional mutagenesis, have been employed to identify critical host factors and pathways essential for enterovirus replication [120] [121]. Host-targeting antivirals offer advantages like broad-spectrum antiviral activity and a high genetic barrier to drug resistance. However, potential cytotoxicity remains a concern due to their impact on host cells.

1.4 Single-particle analysis using cryo-EM

In the last section, anti-enterovirus drugs were described in detail. For most of these, the drug design was structure-based. Structure-Based Drug Design (SBDD) utilizes atomic-level information about a therapeutic target to rationally design and identify in silico chemical compounds effective against that target. It originated in the 1980s, focusing on enzyme-targeting drugs like captopril and dorzolamide [122] [123] [124], as an alternative to the time-consuming and low-yielding high-throughput screening conducted in wet laboratories.

For the past half century, X-ray crystallography has been the predominant technique in structural biology and SBDD. However, it has intrinsic weaknesses that can be overcome by cryo-electron microscopy (cryo-EM). First, X-ray crystallography struggles with difficult-to-crystallize molecules, including some notoriously difficult membrane proteins. In contrast, cryo-EM offers a simpler sample preparation process, requires no crystallization, and uses smaller sample amounts. Second, crystal contacts in X-ray crystallography can alter protein structures, making it challenging to capture their physiologically relevant conformation. Meanwhile cryo-EM rapidly freezes samples in vitreous ice, preserving molecules in near-physiological conditions. Third, X-ray beams aggregate information from all molecules, hindering visualization of structural variability. Each particle's projection in a cryo-EM experiment is recorded independently, allowing estimation of multiple structures associated with different functional states [125]. A third technique, nuclear magnetic resonance (NMR), can determine molecular structures in physiological conditions (water solution at room temperature) but is normally limited to small structures with a relatively small molecular weight.

1.4.1 Brief history of cryoEM

Forty years ago, Dubochet and his team introduced a ground-breaking technique involving vitreous ice, an amorphous solid form of water, to make biological samples vacuum-compatible [126]. Unlike regular ice, vitreous ice lacks a crystalline structure, allowing for the preservation of delicate biological structures. They named this technique cryo-electron microscopy (cryo-EM) as it involved maintaining the vitreous ice at extremely low temperatures using liquid-nitrogen or liquid-helium.

In the following decades, cryo-EM was successfully applied to study large and symmetrical structures like ribosomes and various viruses. However, before 2013, the technique had limitations, and only a few structures were resolved at resolutions better than 7 Å, resulting in what was humorously termed "blob-ology" due to the structures' blob-like appearance.

Around ten years ago, a significant advance came with the development of direct electron detectors (DEDs). These detectors, unlike charge-coupled device (CCD) cameras, do not convert electrons to photons prior to detection. DEDs revolutionized cryo-EM by dramatically improving image quality and signal-to-noise ratio (SNR), enabling researchers to achieve higher resolutions. Moreover, DEDs have high-output frame rates, allowing the recording of multiple frames per micrograph (movies) rather than the integration of individual exposures [127]. These movies aid in compensating for motion induced by the electron beam during imaging.

Additionally, recent hardware developments have made it possible to acquire and store vast amounts of data. Coupled with easy access to powerful CPU and GPU resources, these advances have propelled the field of cryo-EM forward, making it a powerful tool for studying biological structures with unprecedented detail.

1.4.2 Sample preparation and grid making

Biochemical and biophysical knowledge about a sample is essential before using cryo-EM to image biological objects. This information guides the interpretation of cryo-EM micrographs and helps troubleshoot challenging samples. Conventional techniques like gel electrophoresis, size exclusion chromatography, dynamic light scattering, and differential scanning calorimetry can provide valuable data on sample size, shape, molecular weight, purity, and homogeneity, complementing cryo-EM analysis.

Negative stain electron microscopy (EM) complements cryo-EM by providing a valuable tool for sample characterization before cryo-imaging. It allows rapid screening for sample quality, saving time and resources compared to vitrification and cryo-imaging. Moreover, negative stain EM typically requires significantly less sample, about an order of magnitude less. However, one limitation of negative stain EM is that it requires much lower protein concentrations compared to cryo-EM. Complexes that are stable at higher concentrations might disassociate at lower concentrations, posing a challenge when using negative stain EM for certain samples. Additionally, the stains used are acidic which can de-stabilize pH sensitive samples.

The aim of sample preparation for cryo-EM is to suspend proteins in a thin, well-vitrified ice layer on an EM grid. The ideal grid has uniform, vitreous ice slightly thicker than the molecule of interest, with well-distributed particles at sufficient concentration. Reproducible grids lead to more high-quality images collected faster and reduce costs. However, achieving this level of vitrification remains challenging, even with robotic plunge freezers like the Vitrobot and Leica GP2. It requires precise fine motor skills and can be difficult to replicate consistently across grids.

To create a cryo-EM grid, a small sample volume (~3 μL) is applied to the grid and then reduced to a thin film (10-100 nm) by blotting with filter paper. The grid is then rapidly plunged into a cryogen. During the thinning process, the surface area to volume ratio of the sample significantly increases, causing proteins to collide with the air-water interface (AWI) multiple times (100-1,000) between blotting and vitrification [128] [129]. These collisions with the AWI can lead to issues like preferred orientation, denaturation, complex dissociation, and compositional heterogeneity [130] [131]. Despite the challenges posed by the AWI, it also explains why we observe a high number of particles in micrographs despite using low protein concentrations [132] [133]. However, the overall effects of the AWI are not yet fully understood and require further investigation.

Reducing beam-induced motion is another challenge in cryo-EM imaging. During electron beam exposure, sample and support foil movements cause blurred images, limiting high-resolution information capture [134] [135]. Motion-correction algorithms can correct this blurring by analyzing movie frames from direct detectors [134] [136]. However, early frames containing high-resolution information often have the largest movements [137]. To mitigate beam-induced motion, using a gold foil instead of traditional holey carbon support foil has been effective [138]. UltrAuFoil grids (gold foil on gold grids) have been used for high-resolution cryo-EM maps (e.g., apoferritin at ~1.2 Å) [139] [140]. However, carbon foil preparation also achieved high resolution (e.g., apoferritin at ~1.4 Å) [141].

Sample preparation and grid-making for cryo-EM present the largest hurdles for most projects. It remains unpredictable as to which samples will be amenable to imaging by single-particle cryo-EM. Like the problems of making crystals for X-ray crystallography, in cryo-EM it is unknown whether a novel sample will survive current grid-making methods until it is attempted.

1.4.3 cryo-EM instrument

Acquiring images of a vitrified sample requires a cryogenic transmission electron microscope (cryo-TEM). Simply, these microscopes have a source that produces an electron beam, an ultrahigh vacuum system, a series of magnetic lenses that focus the beam, a cryogenic sample holder for translating the grid, and a detector that captures images. Most of these components are still undergoing significant development to improve images and speed up the imaging process.

In the past few decades, electron sources in cryo-EM have undergone significant advancements. The introduction of the field emission gun (FEG) allowed for a brighter electron beam with better spatial and temporal coherence compared to conventional thermionic sources like tungsten filaments or LaB6 crystals. Many high-end cryo-EM microscopes, such as the Titan Krios (Thermo Fisher Scientific), are equipped with FEGs operated at elevated temperatures (XFEGs) for optimal performance. In 2012, Ricolleau and JEOL developed the cold field emission gun (CFEG), the first room-temperature FEG. CFEGs produce an electron beam with a smaller energy spread of around 0.3 eV, offering better temporal coherence and signal-to-noise ratio compared to XFEGs (with a 0.7-eV spread) [139] [142]. This advancement was utilized in 2019 by Kato et al. to achieve a 1.5-Å reconstruction of apoferritin using the JEOL CryoARM-300 equipped with a CFEG. More recently, Nakane et al. achieved a record-breaking 1.2-Å-resolution map of apoferritin by using a prototype CFEG in combination with a new post-column energy filter, called Selectris, both developed by Thermo Fisher Scientific, installed in a Titan Krios microscope. The Selectris energy filter enables stable data collection for extended periods and reduces higher-order distortions with its large prism radius. This advance allowed for the visualization of individual hydrogen atoms in the protein (Figure 1.4.3).

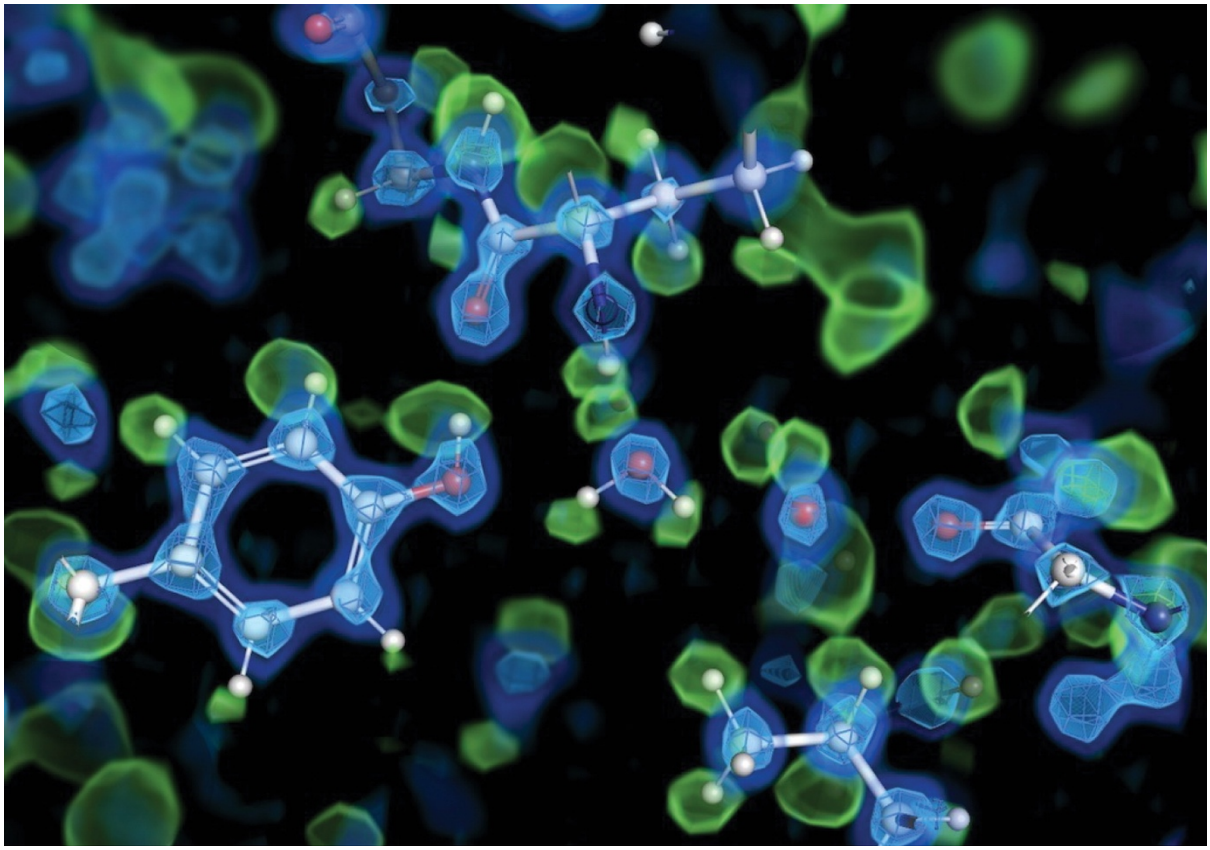


Figure 1.4.3 Advances in cryo–electron microscopy instrumentation and processing recently produced an atomic-resolution map of apoferritin [139], shown here in blue, volume-rendered using PyMOL. The hydrogen difference map (green) shows ordered hydrogens, even on a water molecule (center). Modelled atoms are shown as spheres with bonds as sticks. Carbon is shown in light blue, oxygen in red, nitrogen in dark blue, and hydrogens in white.

Advances in aberration correction also increase the resolution of cryo-EM results. While many of these aberrations, including beam tilt, coma, trefoil, and tetrafoil, can be corrected post-acquisition through software [143], spherical (Cs) and chromatic (Cc) aberrations can be corrected with additional lenses added to the column of the microscope. Cs correctors use hexapole magnets to correct third-order aberrations, and one way of reducing Cc aberrations is by using a monochromator to reduce the energy spread of the electron beam [140].

Recent advancements in direct detector technology have significantly increased data collection rates in cryo-EM [144]. With a day's worth of data collection on a Krios microscope, multiple terabytes of data can now be generated, making data

management a crucial consideration [145]. A notable innovation for recording camera readouts is the use of the electron event representation (EER) format [146]. Instead of saving movies as a series of frames, the EER format records individual electron detection events, capturing both position and time at the detector's physical frame rate. This preservation of spatial and temporal resolution in the data results in smaller file sizes for most applications (although frame-based methods can sometimes use very effective image compression) and can improve motion correction by retaining temporal resolution and eliminating the need for user-defined dose fractionation.

The recent development of the laser phase plate has renewed interest in phase plates in cryo-EM. Turnbaugh [147] demonstrated the capability of generating enough intensity in a Fabry-Perot cavity to induce a 90° phase shift to electrons accelerated to 300 keV. While the Volta phase plate significantly enhanced contrast in cryo-EM images, it faced challenges with continuously developing phase shifts and a reduction in high-spatial frequency information [148]. The laser phase plate holds promise as a potential solution to address these limitations and further improve cryo-EM image quality.

Recent advances in microscope technology have shown that it is no longer a limiting factor in achieving atomic resolution on well-behaved samples. Innovations in microscope design have led to significant improvements in data collection, resulting in enhanced information collected from each sample and micrograph. These developments have pushed the boundaries of cryo-EM, enabling researchers to obtain more detailed structural insights at atomic resolution levels.

1.4.4 Data collection

Once a grid is inserted into the microscope, a data collection strategy is essential to target and image the regions of the grid containing the sample of interest under optimal conditions. In single-particle data collections, the primary objective is to gather sufficient high-magnification images to achieve a reconstruction at the resolution necessary to address the biological question at hand. A typical data collection workflow in cryo-EM involves the following steps:

1. Initial low-magnification atlas of the grid is collected.
2. Squares of interest are selected either automatically or manually by an operator through visual inspection.
3. Higher-magnification images of selected squares are taken to aid in precise targeting of regions of interest.
4. Holes covered by ice of suitable thickness are identified, and drift and defocus are checked and adjusted.
5. High-magnification images of the sample of interest are acquired at the desired dose and pixel size.

Traditionally, this multiscale imaging workflow required substantial manual input and consumed many operator hours on the microscope, making it a tedious and repetitive task. Since the 2000s, data collection software like Leginon [149] [150] [151], SerialEM [152], EPU (Thermo Fisher Scientific), JADAS (JEOL) [153], and Latitude S (Gatan) have been developed to automate these processes. This led to major speedups in cryo-EM data collection rates and reduced the amount of manual input required during a data collection session.

A recent data collection strategy has significantly increased throughput in cryo-EM by utilizing beam-image shifts instead of stage movement to center exposure targets for data acquisition [154]. This approach allows for collecting up to approximately 40 high-magnification exposure images per stage movement on a standard grid, compared to the previous method of obtaining only a single high-magnification exposure image with stage shift data collection. By using beam-image shifts to move to selected targets, the number of slower and less accurate stage movements is minimized, resulting in higher data collection rates. However, the use of beam-image shifts can introduce coma, particularly with larger beam-image shifts. To address this issue, methods have been developed to correct beam tilt and higher-order aberrations either before data collection using hardware [151 155] or after data collection with software [143 156].

1.4.5 Data processing

After acquiring cryo-EM micrographs, the next stage in the pipeline is computational image processing. This involves several essential steps:

1. Motion correction: Correcting for sample and beam-induced movements in movie frames to improve image quality and alignment.
2. CTF estimation: Determining the Contrast Transfer Function to account for electron microscope imaging imperfections.
3. Particle picking and extraction: Identifying and extracting particle images from micrographs for further analysis.
4. 2D classification: Sorting particles into classes based on their 2D projections to identify and remove low-quality or damaged particles.
5. Initial model generation: Generating a low-resolution initial model from the 2D classified particles to serve as a starting point for 3D reconstruction.
6. 3D classification: Further sorting particles based on their 3D structures to segregate different conformations or states of the specimen.
7. 3D refinement: Iteratively improving the 3D model through refinement to achieve a high-resolution cryo-EM map.

In recent years, several approaches to increase the highest achievable resolution for a given cryo-EM data set have been introduced. These include CTF refinement, which estimates defocus and astigmatism on a per-particle basis [157]; Bayesian polishing, which performs radiation dose weighting and corrects for beam-induced motion [158]; and corrections for beam tilt, high-order aberrations, Ewald sphere curvature, and anisotropic magnification [159] [160] [143]. However, since resolution-limiting factors can vary across data sets, including the optical aberrations of the microscope, data collection scheme, and specimen characteristics, there is no universally accepted sequence for performing these corrections to guarantee the highest possible resolution for any given data set.

Researchers need to carefully optimize the correction approach based on the characteristics of their data to achieve the best possible resolution.

Cryo-EM offers a significant advantage in handling high degrees of sample heterogeneity. Heterogeneity can manifest as either discrete, where distinct specimen conformations are easily distinguishable, or continuous, where the conformations are too numerous or similar to be reliably separated. For discrete heterogeneity, consecutive rounds of 3D classification, focused classification, and signal subtraction have been established as effective methods [161,162]. These approaches allow researchers to identify and isolate different conformations within the sample, enabling a more comprehensive understanding of the specimen's structural complexity.

Continuous heterogeneity, which has been a more challenging aspect to address in cryo-EM, has seen significant progress with the development of novel approaches. Multibody refinement tracks user-defined bodies representing specific subunits or components of the specimen, enabling the analysis of continuous variations within the sample [163]. Variability analysis based on principal component analysis fits 3D linear subspace models to cryo-EM data [164]. Machine learning algorithms have also played a crucial role in advancing the analysis of continuous heterogeneity. Manifold embedding allows for tracking conformational motions across the specimen's energy landscape [165]. EMAN2's e2gmm employs a 3D Gaussian mixture model to trace conformational spectrums [166]. Additionally, the application of deep neural networks in CryoDRGN has shown promise in identifying continuous conformational changes and provides tools for exploring per-particle heterogeneity [167]. These innovative approaches have significantly improved our ability to analyse and understand the continuous heterogeneity present in cryo-EM data.

1.4.6 Symmetry mismatch

3D refinement jobs normally require estimating the orientation from which each particle is viewed, relative to a reference density. This ‘alignment’ step enables iterative refinement, and allows for successive reconstruction of an updated density map, and requires solving a 5-dimensional search problem, 3 dimensions of rotation (pose) and 2 dimensions of translation (shift) independently for every particle, via matching projections of the rotated and shifted density to particle images.

Since poses and shifts range over a continuum of possible values, the search space of poses and shifts must be made discrete, so that a projection-matching based likelihood calculation can be performed at all poses in the discrete space. Discretization of poses usually does not cause issues for asymmetric structures, for which each particle will have only one correct pose. Discretization isn’t problematic with perfectly symmetric structures either, because each particle has a set of multiple correct poses, the number of which is equal to the symmetry order of the imposed symmetry group. Each of these correct poses is related to each other via a symmetry transform. In this case, the alignment algorithm can find any of the optimal poses, and the entire set of symmetry-related poses will be used to reconstruct the molecule.

The strategy encounters difficulties with nearly symmetric molecules, also called symmetry-mismatches [168]. Symmetry mismatched particles may have several plausible poses at low resolution, and the correct pose may only be distinguishable if each of the symmetry-related poses are compared directly.

In the latest version of CryoSPARC v4.4, a symmetry relaxation tool is implemented for homogeneous and non-uniform refinement jobs which modifies the orientation search procedure to make the search more thorough, to avoid placing particles in incorrect poses that are related to the true pose by a symmetry transform.

When studying interaction between icosahedral symmetric enterovirus capsid and receptor or antibodies, Cryo-EM data processing it is common to apply icosahedral symmetry to the 3D reconstruction or 3D refinement jobs, despite the fact that viral receptor attachment or antibodies attachment are often not symmetrized. It is not problematic until the symmetrized attachments generate confusion (chapters 3&4).

A novel solution to symmetry mismatched problem was published in 2005 which allowed the improved reconstruction of a partially occupied vertex in Kelp fly virus [169], This virus system was then used to develop a more rigorous approach which successfully produced independent reconstructions of the two types of fivefold vertex. This approach used the orientation information derived from the icosahedral orientation search to facilitate multivariate statistical analysis and to limit the orientational degrees of freedom for reconstruction [170]. The essence of localized reconstruction is that after determining the particle orientations, local areas corresponding to the subunits can be extracted and treated as single particles. The method was subsequently further developed and generalised so that it could be applied to flexible assemblies and complexes harbouring subunits with either partial occupancy or mismatched symmetry [171]. This allowed accurate fitting of the monomeric RNA-dependent RNA polymerase bound at the threefold axis of symmetry inside a viral capsid, revealing for the first time its exact orientation and interactions with the capsid proteins [171].

More recently a localized reconstruction method termed LocalRec was implemented into Scipion (a cryo-EM image processing framework that integrates functions from different image processing packages as plugins), and resolved the symmetry-mismatched trimeric fibre bound to the five-fold vertices of the adenovirus capsid. It also improves the structure determination of the icosahedral capsid by dealing with the defocus gradient across the particle [172].

In this thesis, 'SyRe' protocol (section 2.6.3) is created to tackle such problem, based on localized reconstruction methods previously established. Some notable differences between 'SyRe' protocol and localized reconstruction are: 1. In SyRe the particle's own symmetry axis (for example the five-fold axis of an extracted pentamer) is not aligned to standard orientation (five-fold axis aligned on Z axis). 2. Overlapping particles are not removed so that only one is extracted for any symmetry related position (when this is done, it is possible to apply the right symmetry, or to relax it). 3. Extracted smaller particles are not "back plotted" to regenerate the larger particle from several extracted particles. 4. The average defocus D of the large particle is known, but the relative Z position for each of the smaller particle is not adjusted. To sum up, SyRe is a simpler workflow compared to localized reconstruction, and a CryoSPARC implementation.

1.4.7 Structure building

In the cryo-EM process, after obtaining the cryo-EM map, the subsequent stage involves building and refining an accurate model to represent and interpret the experimental data. This step necessitates a profound understanding of chemistry and the specific nature of cryo-EM maps. Cryo-EM has significantly benefited from model building and validation techniques developed in X-ray crystallography. Commonly employed tools for this purpose include CCP-EM [173], Phenix [174], Rosetta [175], UCSF Chimera [176], ISOLDE [177], and Coot [178].

Model building can encompass various complementary approaches, such as generating homology models based on existing NMR, X-ray, or cryo-EM structures, using secondary structure prediction algorithms to assist in sequencing and building, incorporating restraints from NMR or crosslinking mass spectrometry, and employing integrative structural modelling methods [179]. Automated strategies for model building, like Buccaneer [180], MAINMAST [181], and phenix.map_to_model [182], have been developed to enhance efficiency. Deep learning techniques have also contributed significantly, with neural networks being used to predict protein structures from primary sequence information [183]. Notably, DeepMind's AlphaFold 2 [184] achieved outstanding results in protein structure prediction during the CASP14 assessment. Along with other tools like RoseTTAFold [185], showing great promise in providing preliminary models for proteins with unknown structures, which can be subsequently integrated into cryo-EM data, expediting the overall modelling process.

Finally, the cryo-EM results are deposited, which means the maps and models are made accessible to the wider scientific community. This step has played a crucial role in driving rapid advancements in the field, as it allows other researchers and software developers to analyse the data, test new algorithms and software, and contribute to further improvements [186]. Cryo-EM maps can be deposited in the Electron Microscopy Data Bank (EMDB) (https://www.ebi.ac.uk/pdbe/emdb) [187], while the corresponding atomic models can be deposited in the Protein Data Bank (PDB) (https://www.rcsb.org) [188]. By sharing data in these publicly accessible databases, the cryo-EM community fosters collaboration, transparency, and the dissemination of valuable knowledge for the benefit of scientific progress.

1.5 Neutralizing antibodies against enterovirus

Despite extensive research into antivirals (Section 1.3), there are no approved antiviral drugs or licensed vaccines against the majority of circulating enteroviruses. Antibody immunity plays a key role in preventing and limiting enteroviral infections, which is mainly achieved when the virus is neutralized by specific antibodies [189] [190]. Understanding of this neutralization mechanism has been facilitated by recent progress in elucidating viral structures and antibody-virus complexes, thanks to the advances in methods and equipment in structural biology (Section 1.4). The identification and characterization of potent monoclonal antibodies allows researchers to identify relevant neutralization epitopes at the molecular level.

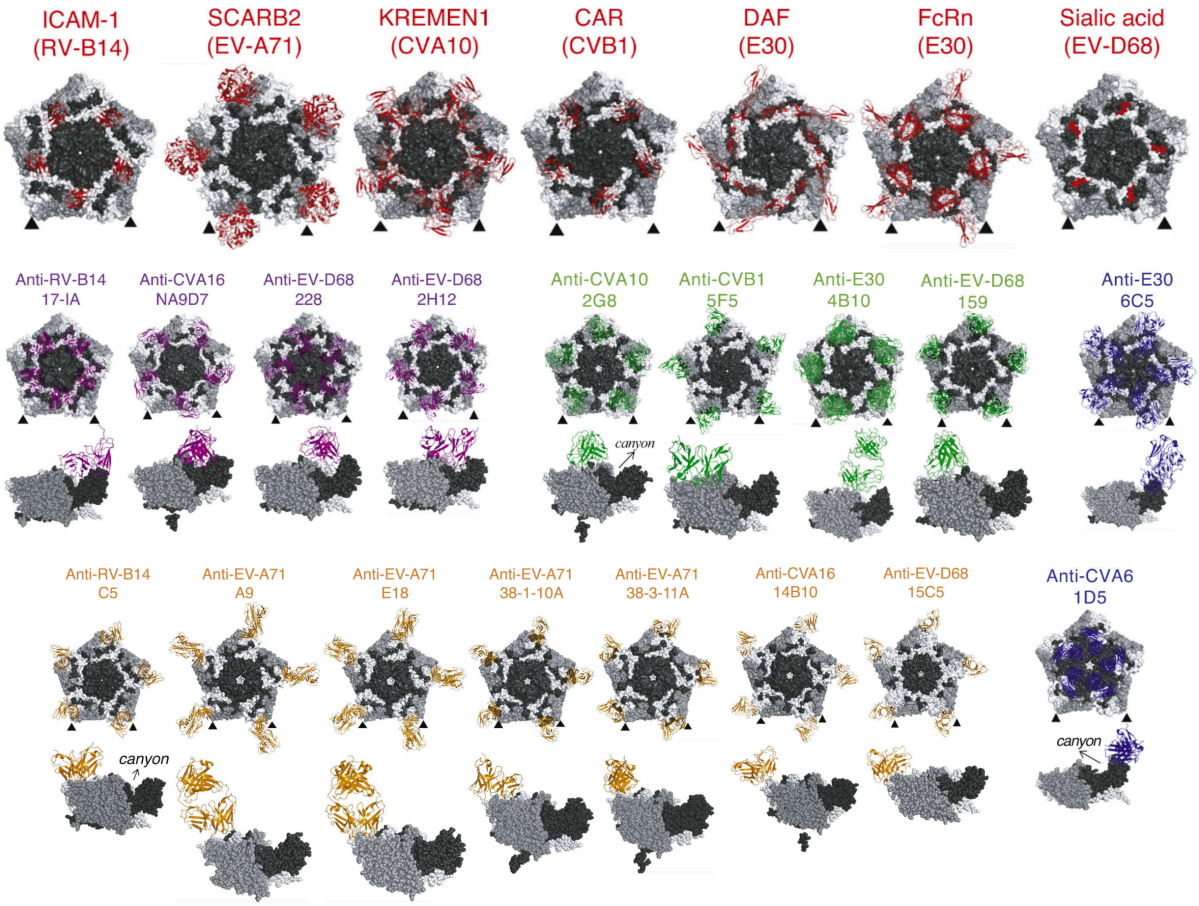


Figure 1.5 structures of neutralizing antibodies against enteroviruses [191]

The capsid-protein pentamer is shown with the 5-fold vertex at the center and the antibody or receptor is shown in cartoon representation. A side view of the icosahedral asymmetric unit of capsid is also shown. The capsid VP1 protein is coloured in black, VP2 in grey and VP3 in white. **(Red – cellular receptors for enteroviruses)** Enterovirus in complex with receptor ICAM-1 (PDB 7BG7), SCARB2 (PDB 6I2K), KREMEN1 (PDB 6SNW), CAR (PDB 7DQ1), DAF (PDB 7C9W), FcRn (PDB 7C9V) or sialic acid (PDB 5BNP). **(Purple – neutralizing antibodies against canyon depression)** Enterovirus in complex with anti-RV-B14 17-IA (PDB IRVF), anti-CVA16 NA9D7 (PDB 6LHQ), anti-EV-D68 228 (PDB 6WDT) or anti-EV-D68 2H12 (PDB 7EBZ). **(Green – neutralizing antibodies against southern rim of the canyon)** Enterovirus in complex with anti-CVA10 2G8 (PDB 6AD0), anti-CVB1 5F5 (PDB 7DQ7), anti-E30 4B10 (PDB 7C80) or anti-EV-D68 159 (PDB 6WDS). **(Blue - neutralizing antibodies against northern rim of the canyon)** Enterovirus in complex with anti-CVA6 1D5 (PDB 5XS7) or anti-E30 6C5 (PDB 7C81). **(Yellow - neutralizing antibodies against 3-fold plateau)** Enterovirus in complex with anti-RV-B14 C5 (PDB 5W3E), anti-EV-A71 A9 (PDB 5ZUF), anti-EV-A71 E18 (PDB 4C0U), anti-EV-A71 38-1-10A (PDB 6Z3Q), anti-EV-A71 38-3-11A (PDB 6Z3P), anti-CVA16 14B10 (PDB 6LHP), or anti-EV-D68 15C5 (PDB 6AJ7). Rhinovirus B14, RV-B14; Enterovirus A71, EV-A71; Coxsackievirus A10, CVA10; Coxsackievirus A16, CVA16; Coxsackievirus A6, CVA6; Coxsackievirus B1, CVB1; Echovirus 30, E30; Enterovirus D68, EV-D68; Intercellular adhesion molecule-1, ICAM-1; Scavenger receptor class B member 2, SCARB2; Kringle containing transmembrane protein 1, KREMEN1; Coxsackievirus-adenovirus receptor, CAR; Decay-accelerating factor, DAF; Neonatal Fc receptor, FcRn.

1.5.1 Enterovirus A71

In contrast to the cellular receptor SCARB2 for EV71 (detailed description in chapter 5), the neutralizing antibody A9 (Figure 1.5 yellow2) does not interact with residues located in the vicinity of the canyon region. Instead, A9 binds to the virion spanning the area between the 2-fold and 3-fold axes, in a bivalent manner. When the murine antibody A9 binds, it triggers a transformation of the virions into empty particles even under physiological temperatures [192]. These changes in the capsid's conformation brought about by the antibody can disrupt the virus's ability to recognize its receptor, which helps elucidate A9's capacity for neutralization prior to virus-cell attachment.

The murine antibody E18 (Figure 1.5 yellow3) induces capsid conformational changes and early viral genome release, similar to A9 [193]. They both target epitopes near the capsid pentamer edges. However, E18's broader footprint extends to the SCARB2 receptor-binding site. This suggests a receptor-like neutralization mechanism for E18. Additionally, E18 might partially neutralize by competing with the virus-receptor interaction.

Advanced techniques have emerged to streamline the production of human monoclonal antibodies. Single-cell expression systems enable the isolation of native human monoclonal antibodies, maintaining the natural pairing of heavy and light chain variable domains [194] [195]. Notably, human antibodies 38-1-10A and 38-3-11A (Figure 1.5 yellow4&5), obtained from EV-A71 convalescent patients, exhibit potent nanogram-level neutralization of the virus. Despite originating from distinct variable regions, both antibodies target highly similar epitopes surrounding the 3-fold axes [194]. When compared with EV-A71/SCARB2 [19], structural analysis reveals clashes between the Fabs of the antibodies and the receptor, indicating their role in impeding receptor binding.

1.5.2 Echovirus

Echoviruses primarily utilize DAF as their attachment receptor, with viral entry facilitated by the neonatal Fc receptor (FcRn) [196] [197]. FcRn engages the canyon depression, interacting with VP1 BC, EF, GH, and VP2 EF loops [196] [197]. Recent advances led to the isolation of two specific murine neutralizing antibodies, 6C5 and 4B10 (Figure 1.5 blue2 & green3), targeting echovirus 30 (E30). These antibodies target the northern and southern rims (can check Figure 4.1.1 in chapter 4 for the location of rims) of the capsid canyon respectively [198]. When the capsid is fully occupied, 60 copies of Fab 6C5 and 4B10 bind to it, demonstrating potent activity against E30. Although capsid conformational changes are not evident upon binding, both antibodies effectively hinder the interaction between the virus and receptor DAF, as well as between the virus and FcRn. This suggests that the neutralizing action of 6C5 and 4B10 stems from their ability to block these crucial binding events.

1.5.3 Rhinovirus B14

Structural investigations have elucidated that intercellular adhesion molecule-1 (ICAM-1), characterized by an elongated structure composed of immunoglobulin-like domains, serves as a receptor for major human rhinoviruses and fits well with the capsid canyon [199]. The identification of neutralizing murine antibody 17-IA (Figure 1.5 purple1) marked a notable breakthrough, as canyon-targeting antibodies had been scarcely observed [200 201]. Structural analysis of the Fab-virus interaction revealed that 17-IA engages extensively with a substantial portion of the canyon's internal surface, aligning its footprint with the ICAM-1 receptor-binding site. Although not reaching the canyon's base, 17-IA establishes significant contact with the inner wall and rim, resulting in bivalent binding to the viral capsid at a ratio of 30 antibodies per virion. This binding strongly neutralizes the virus, primarily by disrupting viral attachment to cellular receptors. The stability induced in the capsid structure by the antibody could further contribute to neutralization [202], a phenomenon also observed in other anti-rhinovirus antibody structures [203 204].

In rhinovirus entry, a critical stage involves capsid structural changes post-cell attachment, crucial for genome release through uncoating. The neutralizing murine antibody C5 (Figure 1.5 yellow1), upon binding, induces premature genome release and virion-to-empty particle transformation. However, these effects are temperature and virus-Fab molar ratio dependent [205]. Examination of the complexes indicates that 60 Fab C5 molecules bind to the epitopes around the 3-fold axes (epitope NIm-III) [16], distinct from the ICAM-1 receptor-binding site. Consequently, antibody-triggered conformational shifts may influence virion function, playing a role in virus neutralization.

1.5.4 Coxsackievirus

Coxsackievirus A16 presents a scenario where neutralizing murine antibodies 14B10 and NA9D7 (Figure 1.5 yellow6 & purpe2) target distinct epitopes – the capsid 3-fold plateau and the inner surface of the canyon, respectively [206]. Although these capsid-binding antibodies do not trigger any conformational changes in the capsid, their neutralization mechanism likely revolves around hindering viral attachment. This is supported by the potential overlap of both 14B10 and NA9D7 footprints with the presumed receptor-binding site, which encompasses the VP1 GH loop and VP2 EF loop [19] [207]. Additionally, binding of either Fab or full-length antibodies contributes to virion stabilization, possibly contributing to their neutralizing effect [206].

Recent studies on Coxsackievirus A6 and A10 have unveiled that kringle containing transmembrane protein 1 (KREMEN1) serves as the host receptor, with the receptor-binding site extending across the capsid canyon region (Figure 1.5 red3) [208] [209]. Two highly effective murine antibodies, known as anti-CVA6 1D5 and anti-CVA10 2G8 (Figure 1.5 blue1 & green1), have shown remarkable efficacy in murine models against lethal challenges. These antibodies target conserved epitopes situated at the northern and southern rims of the capsid canyon, respectively (for the canyon rim position, please go to Figure 4.1.1 in chapter 4) [210] [211]. Structural analysis of the antibody-virus complexes reveals that each capsid is engaged with 60 copies of Fabs. The footprints of both 1D5 and 2G8 antibodies slightly overlap with the receptor-binding site (specifically, the VP1 EF loop with 1D5, and the VP1 C-terminus and VP3 AB loop with 2G8) [210] [211], suggesting that their binding may partially obstruct viral attachment. This neutralization mechanism is corroborated by the significant inhibition of virus binding in the pre-attachment stage by both 1D5 and 2G8.

Across various serotypes of coxsackievirus B, binding to host cells involves the coxsackievirus-adenovirus receptor (CAR), with some serotypes (CVB1, CVB3, and CVB5) additionally capable of binding to the decay-accelerating factor (DAF) for viral attachment [212]. The interaction with CAR triggers viral uncoating and genome release [213]. Both CAR and DAF receptors engage with the viral capsid's canyon region. CAR attaches to the inner surface of the canyon, while DAF spans the canyon and extends into the southern rim at the VP2 EF loop's 'puff' region [213 31]. The potent murine neutralizing antibody anti-CVB1 5F5 (Figure 1.5 green2) demonstrates efficacy against viruses and offers in vivo protection. Upon analyzing the Fab-virus complex, it was observed that 5F5 binds to the capsid's southern rim of the canyon, with its footprint extending to the 3-fold plateau. While the 5F5 footprint doesn't directly overlap with the CAR-binding site, antibody binding could potentially impact the virus-receptor interaction through steric hindrance [213]. Importantly, both 5F5 and DAF have overlapping footprints on the southern rim of the canyon region, particularly involving the VP2 EF loop. This is further supported by their dose-dependent inhibition of viral attachment [213 31]. Additionally, the binding of 5F5 induces conformational changes in the capsid and viral disruption, mimicking the effects of receptor binding [213].

1.5.5 Enterovirus D68

Cell surface sialic acid plays a crucial role in EV-D68 attachment and infection, and the structure of the complex reveals that the receptor-binding site is located in the canyon region [214]. Receptor binding triggers the release of the pocket factor, collapse of the pocket and subsequent conformational changes, which are prerequisites for infection.

The neutralization of the virus could be attributed to interference with virus binding to the sialic acid receptor. Potent human antibodies 159 and 228 (Figure 1.5 green4 & purple3) were isolated from patients with EV-D68 infection [215]. Antibodies 159 and 228 target epitopes adjacent to and within the canyon region, respectively. The Fab-virus complexes revealed that part of the antibody footprints for 159 or 228 overlapped the sialic acid receptor-binding site (the VP1 C-terminus and VP3 C-terminus), which indicates that receptor binding blockade may contribute to the function of these antibodies, but they target different epitopes and differ in their neutralization breadth against EV-D68 [215]. Within the antibody 228 footprint, the exposed amino acid residues were highly conserved across serotypes of EV-D68. In contrast, the residues in the antibody 159 epitope are conserved among B1, B2, and B3 strains, but are changed in Fermon and emerging D strains, which may explain the loss of neutralization with these mutated strains.

Similar to antibody 228, the murine antibody 2H12 (Figure 1.5 purple4) also binds to the canyon region, effectively neutralizing wild-type viruses and providing protection against lethal EV-D68 challenges in vivo [215]. The footprint of antibody 2H12 coincides with the receptor-binding sites for sialic acid. This suggests that the neutralizing effect might stem from their ability to obstruct the binding of EV-D68 to the receptor, contributing to their potent neutralization activities.

Neutralization of EV-D68 may also result from the destabilization of the virion structure [216] [217]. The interaction between the anti-canyon antibody 2H12 and the virus leads to premature viral uncoating and the release of the viral genome [216]. Similarly, the murine antibody 15C5 (Figure 1.5 yellow7) targets the epitope around the 3-fold axes, inducing the transformation of virions into expanded form. This transformation also obstructs the attachment process [217].

Notably, antibodies against EV-A71 and CV-A16 exhibit recognition of analogous epitopes positioned close to the icosahedral 3-fold axes of the capsid [194] [193] [206]. An interesting observation is that residue 74 within the VP3 BC loop is targeted by both the EV-D68 with antibody 15C5 and the EV-A71 with antibody 38-1-10A [217] [194]. This highlights the VP3 BC loop as an immunogenic hotspot in the antibody response to enteroviruses.

Chapter Two

Methods and Materials

In this chapter, standard protocols for all the experiments performed by the author and mentioned in this thesis are described in detail, and all the materials used in the experiments are provided with the exact name and quantity if necessary. Readers can simply reproduce the results by following the protocols below.

This chapter is divided into several sections, each describes a series of experiments sharing similar methods and purposes. Sections 1-6 are standard methods for structural biology, starting from molecular cloning, protein expression and purification, virus culture and purification, followed by EM grids making, data collection, and data processing. Sections 7-9 describe unique methods performed in this thesis including nanodisc assembly techniques, phylogenetic analysis and thermofluor experiments.

All the experiments mentioned in this chapter were performed by the author, except those where the contributions of other colleagues are mentioned.

2.1 Molecular Cloning

In this section, the protocol for shifting the affinity tag of the nanodisc membrane scaffold protein (MSP) from a His tag to StrepII tag is described in detail. Molecular cloning of DAF is described in brief as it shares the same method with the MSP.

2.1.1 Plasmid information and cloning workflow

pET28a-MSP-His plasmid vector was derived from a previously published construct [218]. The plasmid with a kanamycin resistance gene and MSP26 gene region was sequenced by Eurofins with the sequencing primers for verification (shown below).

- T7 promoter forward primer: 5'-TAATACGACTCACTATAGGG
- T7 Terminator reverse primer: 5'-GCTAGTTATTGCTCAGCGG

In step A of Figure 2.1.1, pET28a-MSP-HIS plasmid was first linearized from the 6 consecutive histidine portion (CATCACCACCATCATCAC). In the linearized plasmid, the His tag was removed, leaving a gap which was filled by the StrepII tag gene in step B and circularizing the plasmid at the same time.

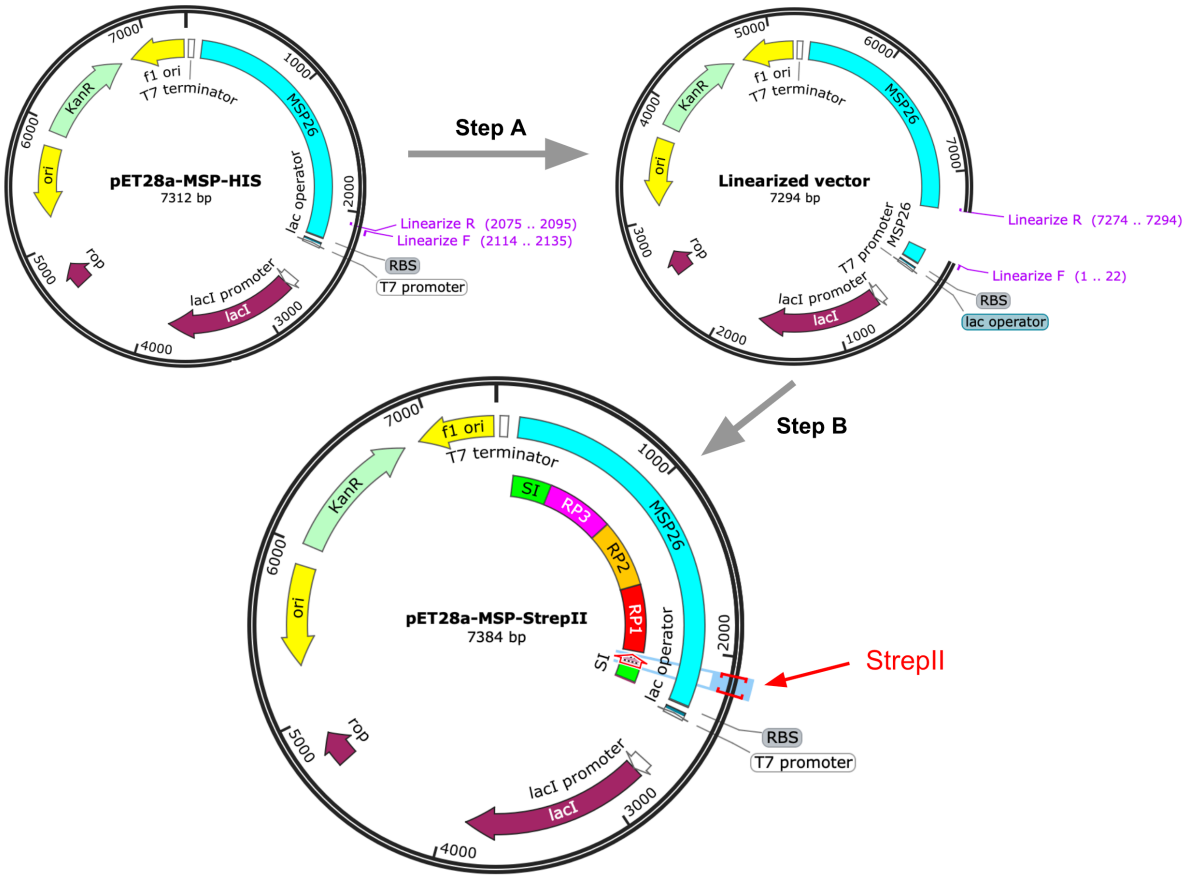


Figure 2.1.1 overall workflow pET28a-MSP His tag replaced by StrepII tag

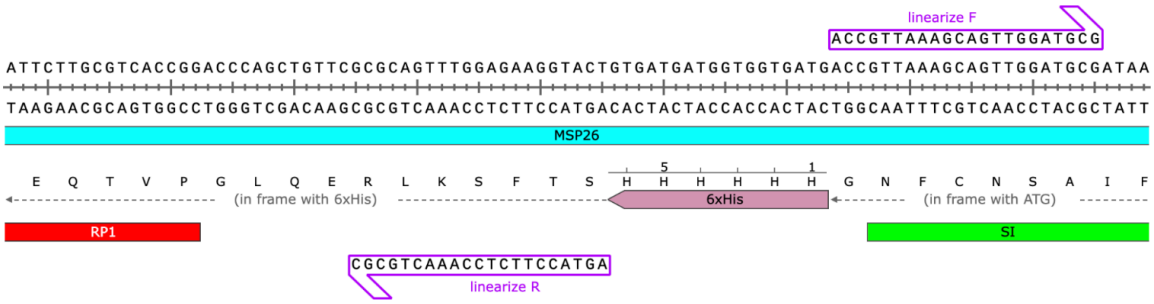


Figure 2.1.2 pET28a-MSP-His linearization cutting point and primers

Template plasmid (~50 ng/μL)	1ul
Forward primer (10 μM)	2ul
Reverse primer (10 μM)	2ul
2X Phusion Flash Master Mix (F-548L, Thermo Scientific)	25ul
Sterile water	20ul

Table 1.1.1 PCR reaction mixture content

Cycle step	Temperature	Time	Cycles
Initial Denaturation	98°C	30s	1
Denaturation Annealing Extension	98°C 58°C 72°C	5s 10s 5min	35
Final extension	72°C 4°C	5min Hold	1

Table 1.1.2 PCR program parameters

2.1.2 pET28a-MSP-His plasmid linearization

To replace the His tag gene, the plasmid was linearized from both ends of the His tag by PCR with linearize F & linearize R primers (Fig 2.1.1 step A, Fig 2.1.2, Table 1.1.1, Table 1.1.2).

After the PCR reaction, all the PCR product was mixed with 5x DNA Loading buffer (0.25% w/v Bromophenol Blue in 30% v/v glycerol). Then samples were loaded onto a 1.6% TBE agarose gel and run at 100 V for about 30 minutes. The linearized plasmid did not run far into the gel and was recycled by PureLink™ Quick Gel Extraction and PCR Purification Combo Kit.

2.1.3 Affinity tag replacement

Full length StrepII gene was synthesized and purchased from the GenScript company. Both ends of the synthetic StrepII gene have 18bp sequences overlapping with target location of the plasmid (Figure 1.1.3). The synthetic gene fragment was amplified by PCR (Table 1.1.3 & 1.1.4) and recovered through Gel extraction.

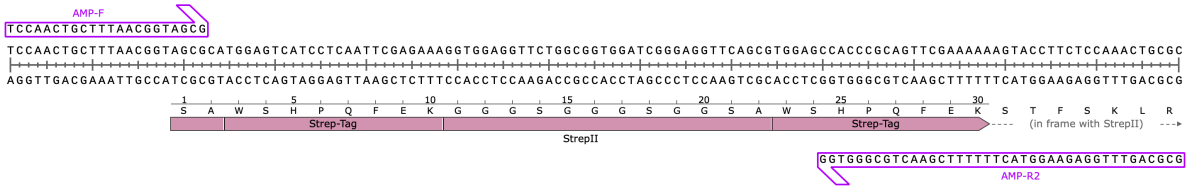


Figure 1.1.3 StrepII tag gene and its amplification primer

Template plasmid (~100 ng/μL)	1ul
Forward primer (10 μM)	1ul
Reverse primer (10 μM)	1ul
2X Phusion Flash Master Mix (F-548L, Thermo Scientific)	25ul
Sterile water	22ul

Table 1.1.3 PCR reaction mixture content

Cycle step	Temperature	Time	Cycles
Initial Denaturation	98°C	10s	1
Denaturation Annealing Extension	98°C 58°C 72°C	5s 10s 30s	40
Final extension	72°C 4°C	5min Hold	1

Table 1.1.4 PCR program parameters

In-Fusion® HD Cloning Kit from Takara Bio company and its standard protocol was applied to insert the StrepII gene to the linearized plasmid (Fig 1.1.3 step B).

2.1.4 pET28a-MSP-StrepII plasmid amplification

E.coli DH5α was used to further amplify the pET28a-MSP-StrepII plasmid, and the strain was spread and grown in liquid LB medium first and LB plates next. both LB mediums contained 25mg/L kanamycin in order to select the target strain

2.1.5 DAF cloning

The cDNA of human DAF (UniProt KB P08174) was ordered from Horizon Discovery Ltd, Cambridge, UK (cDNA clone ID: 3460621). The DNA encoding SCR 1-4 of DAF (residues 35-285aa) was amplified by PCR with primers

5'-TGTTACCGGTGACTGTGGCCTTCCCCCAGAT (forward)

5'-ACTTGGTACCTCCTCTGCATTCAGGTGGTGGGC (reverse).

Amplified cDNA was cloned into the pHL-Sec vector [219], with sequences encoding a C-terminal 6*His tag added.

2.2 Protein expression

In this section, the protocol of protein expression is described. cMSP (circularized membrane scaffold protein) was expressed in bacteria (*E.coli*), while SCARB2 was expressed with mammalian cells (HEK-293T). These two are well established methods for protein production and have their unique advantages. The *E.coli* expression system has a simple protocol, high production rate and requires less and cheaper materials. For HEK-293T expression, the signals for synthesis, processing and secretion of eukaryotic proteins are properly and efficiently recognized by the mammalian cells, which is necessary for studying human SCARB2 and DAF biological function *in vitro*.

2.2.1 cMSP26 from E.coli

One tube of BL21 (DE3) competent *E. coli* cells was completely thawed on ice (~ 10 minutes) until the last ice crystals disappeared. 50 µl of cells were gently mixed and carefully pipetted into a 1ml Eppendorf tube on ice and 10 ng of cMSP or cMSP-StrepII plasmid were added shortly after. The tube was carefully flicked 5 times to mix cells, placed on ice for 30 minutes, and then heat shocked at exactly 42°C in a water bath for 45 seconds. The tube was placed on ice for 5 more minutes, and 950 µl of room temperature LB medium was added into the mixture. The tube was vigorously shaken (250 rpm) at 37°C for 60 minutes. The cells were mixed thoroughly by flicking the tube and inverting, then 10-fold serial dilution into LB medium was applied to the cells. 50–100 µl of each dilution was spread onto a selection plate (kanamycin resistant) and incubated overnight at 37°C.

A single colony of *E.coli* from the selection plate was transferred to 5ml LB medium and the vessel was vigorously shake at 37 °C overnight. Then the sample was diluted and cultured in larger vessels for increased production. When the cell density rose to OD=0.9 (~ 7 hours after transfer), the incubator was adjusted to 20°C and 0.5mM IPTG was added to induce cMSP production. 24 hours after induction, cell pellets were spun down (4000rcf, 15min, 20°C) and collected. Subsequently the protein was purified using affinity purification and size-exclusion chromatography (section 2.3.1 & 2.3.2).

2.2.2 SCARB2 and DAF from HEK-293T

The expression plasmid for SCARB2 provided was provided by lab colleague Dr. Yuguang Zhao. The plasmid encodes the luminal domain of SCARB2 containing residues 28–431, with a C-terminal His tag. For a high scale protein expression, a large quantity of plasmid and HEK-293T cells are required before performing transfection and expression.

At first, HEK-293T cells (ATCC, Manassas, VA, USA CRL-11268) were cultured in T175 flasks (Greiner Bio-One) with 30 mL DMEM supplemented with 10% FBS, 1% 100x L-glutamine and 1% 100x MEM + NEAA. When confluent, cells in each flask were transferred into one CellMaster cell culture roller bottle (Greiner Bio-One) and cultured at 37 °C for 3 days (culture medium: 200 mL DMEM supplemented with 10% FBS, 1% 100x L-glutamine and 1% 100x MEM + NEAA). Then the old medium was replaced with new medium (200mL DMEM supplemented with 2% FBS, 1% 100x L-glutamine and 1% 100x MEM + NEAA) in each roller bottle.

While waiting for the HEK-293T cells to grow, plasmid amplification was performed in parallel. The plasmid of SCARB2 was transformed into E. coli DH5α competent cells (Invitogen). Then single colonies were picked, cultured in 10 mL LB medium supplemented with 50 μg/mL Ampicillin. Cells for each plasmid were added to 2.5 L of LB medium (with 50 μg/mL Ampicillin) to grow at 37 °C for 16 to 18 hours in an incubator shaking at 180 rpm. Cells were harvested by centrifugation at 6,000 g for 15 min. The DNA was purified from the cells following the protocol of HiSpeed Plasmid Giga EF Kits (Qiagen).

For the last step is transfection. 0.25 mg of the SCARB2 plasmid, 200 mL DMEM and 4mL 1 mg/mL polyethyleneimine (PEI) were mixed and incubated at room temperature for 10 minutes to produce the transfection cocktail. Then 50 mL of transfection cocktail was transferred to each roller bottle and the cells were cultured at 37 °C for 4 days before harvest.

The same method was applied to transfection of the recombinant plasmid pHL-DAF into HEK-293T and DAF expression.

2.3 Protein Purification

In this section, MSP, SCARB2 and DAF purification protocols are described in detail. MSP with two different tags is purified separately and with very different methods. The cMSP26 purification protocol was originally created by lab colleague Dr. Pranav Shah and modified by the author. The cMSP26 StrepII purification protocol was created by the author. The SCARB2 purification protocol was contributed by lab colleague Dr. Daming Zhou. DAF purification uses the same protocol as SCARB2. Samples from each step of MSP purification were collected and run on SDS-PAGE.

2.3.1 cMSP26

The cell pellets used to express cMSP26 were resuspended in Buffer (50 mM Tris pH=8.0, 400 mM NaCl, 0.5mM EDTA, 1 protease inhibit tablet, 1mM PMSF, 1%TX-100, Lysozyme) and stirred on ice for 30 mins. The solution was sonicated and resuspended (30%, 1s on, 3s off, 30min) in an ice bath. Cell debris was spun down (30min, 35000rcf, 4°C). Supernatant was collected to which 8M UREA and 5mM MgCl2 were added.

To purify the cMSP26-His protein, a 5ml HisTrap^{TM} excel column was first equilibrated with Buffer W (50 mM Tris, pH=8.0, 400 mM NaCl, 8M urea). Post equilibration, the protein containing supernatant was continuously flowed overnight through the column to maximise the overall yield of the protein. The next day, the column was washed (flow speed 0.1ml/min) with 10ml Buffer W, and eluted (flow speed 0.2ml/min) with 20ml Buffer (50 mM Tris, pH=8.0, 400 mM NaCl, 8M urea, 200mM imidazole).

The eluted sample was dialysed against Buffer (50 mM Tris, pH=8.0, 400 mM NaCl) overnight at 4˚C (10kDa cut off, overnight twice). The dialysed protein was then concentrated using a spin concentrator (50kD Millipore Amicon). The concentrated cMSP26 protein was further purified using a Superose 200 26/600 size exclusion column (Sigma-Aldrich). Results are presented in section 5.2.

Finally, the yield of the protein was measured using a nano-drop spectrophotometry and the concentration was adjusted to 20µM prior to being flash frozen in LN_2 and stored at -80˚C until further use.

2.3.2 cMSP26 StrepII

Cell pellets used to express cMSP26 StrepII were resuspended in Buffer (100 mM Tris/HCl pH 8.0, 150 mM NaCl, 1 mM EDTA) and stirred on ice for 30 min. The solution was sonicated (30%, 1s on, 3s off, 30min) in an ice bath. Cell debris was spun down (30min, 35000rcf, 4°C) and the supernatant was collected.

The top and lower cap of the Strep-Tactin XT column were removed in order. The column was equilibrated with 1 column volume of Buffer (100 mM Tris/HCl pH 8.0, 150 mM NaCl, 1 mM EDTA) twice. A 5ml sample from the supernatant was applied to the column and flowed through at 4°C. Once the cell extract had completely entered the column, it was washed through with 1 column volume of Buffer (100 mM Tris/HCl pH 8.0, 150 mM NaCl, 1 mM EDTA) 5 times. 3 column volumes of Buffer (100 mM Tris/HCl pH 8.0, 150 mM NaCl, 1 mM EDTA, 50 mM biotin) was used to elute the cMSP26 StrepII protein. Results are presented in section 5.3.

2.3.3 SCARB2 and DAF

The SCARB2 and DAF purification procedure mainly involved three steps: dialysis, affinity purification and gel filtration.

Following section 2.2.2, HEK-293T cells were harvested by centrifugation at 1,500 g for 20 min. Supernatant was collected and filtered using a 0.45 μm filter (Amicon) to remove cell debris. 1L of supernatant was poured into a dialysis tube (Medicell Membranes Ltd) to perform dialysis in 15 L of buffer (23.2 mM Na2HPO4, 1.7 mM NaH2PO4, 250 mM NaCl, pH 8.0). The buffer was stirred gently at 4 °C overnight, replaced with fresh buffer, and stirred for another day.

A 5 mL His trap HP column was used for affinity purification of the target protein. Filtered supernatant was pumped through the nickel column for protein binding. Then 50 mL of washing buffer (20 mM Tris, pH 8.0, 200 mM NaCl, 20 mM imidazole) was used to wash the column followed by 5 mL of elution buffer (20 mM Tris, pH 8.0, 200 mM NaCl, 500 mM imidazole) to elute the target protein.

Gel filtration chromatography was performed on the AKTA purifier system (GE Healthcare) with a Hiload 16/60 Superdex 75 column (GE Healthcare), with buffer (20 mM Tris, pH 8.0, 200 mM NaCl). UV (280nm) absorbance was used to detect the presence of protein. The flow rate was set at 1 ml/min and fractions of 0.5 mL were collected in tubes. Fractions showing high 280nm absorbance were harvested, mixed, concentrated to about 200 μL using a 10 kD centrifugal filter (Sigma-Aldrich) and stored at 4 °C.

2.4 Enterovirus culture and purification

Echovirus 11 and Enterovirus A71 share the same culture and purification procedure. The EV71 strain used in this study was EV71 genotype C4, isolated from Fuyang city, Anhui Province, China and provided by Prof. Xiangxi Wang (Chinese Academy of Sciences, China). Strain 18-2135 of echovirus 11 was used in this study. Rhabdomyosarcoma cells (RD cells) were used as the host cells for enterovirus replication.

2.4.1 RD cell culture and enterovirus infection

Frozen RD cell seed was first cultured in T175 flasks at 37 °C in 30 mL DMEM supplemented with 10% FBS, 1% 100x L-glutamine and 1% 100x MEM + NEAA, respectively. Once the cells in the flasks were confluent, the medium was removed and new medium (20 mL DMEM supplemented with 2% FBS, 1% 100x L-glutamine and 1% 100x MEM + NEAA) was added to the flasks. For large scale virus production, RD cells were suspended by adding buffer containing trypsin and transferred to CellMaster roller bottles (300ml medium per bottle) for further amplification. Once the cells in the bottle were confluent, EV71 or Echovirus 11 was added, and left until all the RD cells were dead and could be easily shaken down from the bottle walls.

2.4.2 Enterovirus purification

RD cells were resuspended by vigorously shaking the roller bottles and transferring them to 500ml centrifuge bottles containing 40g PEG6000 (Sigma). The bottles were left at 4°C overnight to precipitate the virus particles. Centrifugation (3,200g 1h 4°C) was applied and the precipitates were collected and resuspended with 10ml Buffer (50mM HEPES, 200mM NaCl, pH 7.5) per centrifugation bottle. The sample was stored at -80°C overnight (whilst the cells are not formally disrupted this freeze-thaw process allow majority of virus particles to be released). 0.5% NP-40 was added to the tube before spinning down the remaining cell debris (3,200g 1h 4°C). Precipitates were resuspended with Buffer (50mM HEPES, 200mM NaCl, pH 7.5) and centrifuged again (3,200 g 1h 4°C). Supernatants from both spins were transferred into ultracentrifuge tubes (11U2932, 40ml volume). 2ml sucrose buffer (50mM HEPES, 200mM NaCl, pH 7.5, 30% w/v sucrose) was injected to the bottom of the tube through a long needle before launching the ultracentrifugation (160,000g 3h 4°C, Beckman SW 32Ti rotor). Precipitates were resuspended with 0.5ml Buffer (50mM HEPES, 200mM NaCl, pH 7.5) per ultracentrifugation tube and transferred into a 1.5ml Eppendorf tube for centrifugation (16,000g 30min 4°C). If the supernatant was not crystal clear, more buffer was added and the tube centrifuged again. The supernatant was collected and stored on ice.

Ultracentrifuge tubes (11U2932) were used for 15-45% sucrose gradient ultracentrifugation. The empty tube was placed into a small metal container to draw a line in the middle of the tube. Sucrose buffer (50mM HEPES, 200mM NaCl, pH 7.5 15% w/v sucrose) was added up to the line and buffer (50mM HEPES, 200mM NaCl, pH 7.5 45% w/v sucrose) was gently injected to the bottom of the tube, until the layering line reached the middle line. The tube was gently placed onto the biocomp premier gradient forming instrument (check balance before use) and sealed with a long cap. The formation of the sucrose gradient completely relied on the machine, but a refractometer could be used to check it. The supernatant sample was gently added to the top of the sucrose gradient solution, and ultracentrifuged using the Beckman SW32Ti rotor (160,000g 3h 4°C). The band nearby the drawn line was collected and diluted with sucrose free buffer. The diluted sample was centrifuged with Beckman SW32Ti rotor (160,000g 3h 4°C). Virus at the bottom of the tube was resuspended and the concentration measured by Nanodrop.

2.5 Grid making and EM data collection

In this section, the protocols for negative stain and cryo-grid sample preparation are described. Negative staining was used to check the status of the VRNC using the Tecnai T12 TEM (120kV). The echo11-DAF complex and poliovirus-pAb complex samples were checked using the Glacios TEM (200kV, Thermo Fisher Scientific) and data collected using the Titan Krios TEM (300kV, Thermo Fisher Scientific).

2.5.1 Negative stain microscopy

Formvar grids (Agar Scientific) were glow discharged for 30s on high level, before adding 4 µl of sample on the carbon surface. The sample was incubated for 60s on the grids and blotted from the edge of the grids without anything touching the center area of the grid. The grids were then washed with MQ water and blotted three times, before applying the stain (2% uranyl acetate or uranyl formate). After 1 min staining, the sample was blotted again and visualized in the TEM.

2.5.2 cryo-EM sample preparation

Echovirus 11

Echovirus 11 (E11) particles (~2 mg/mL) were incubated with DAF protein (4.3 mg/mL) at room temperature for 1.5 h, with a molar ratio of DAF:E11 protomer of 3:1 (i.e., 180 DAF molecules per virus particle). All incubations were at room temperature or on ice rather than physiological temperature in an attempt to increase the chance of capturing the complex. 4 μL of the sample was applied to a glow-discharged ultra-thin carbon Lacey grid (Agar Scientific, London, UK S187-4), blotted by filter paper from the back of the grid (blotting time ~3 s) and vitrified by plunging into liquid ethane/propane mix (50%:50%) using a manual plunger (Max Planck Institute of Biochemistry, Munich, Germany).

Poliovirus-pAb

Sera containing anti-poliovirus polyclonal antibodies are from National Institute for Biological Standards and Control (NIBSC) (named pAb1) and from Prof. David Rowlands from University of Leeds (named pAb2). The sera were dissolved in Tris Buffer (20 mM Tris, 150 mM NaCl, pH 8.0) and centrifuged to remove undissolved precipitates. Then the sera were passed through a 5mL HiTrap Protein G HP column (Cytiva). The column was washed with Tris Buffer (20 mM Tris, 150 mM NaCl, pH 8.0) and eluted with 100 mM Glycine (pH2.6). The pH of the elute was neutralized to neutral pH by adding 9X volume of buffer (0.1 M Tris, pH 9.0).

Purified polyclonal antibodies were digested into Fab and Fc fragments using papain and Fc fragments were removed by 1mL NAb Protein A Plus Spin Column, following the protocol of the Pierce Fab Preparation Kit (Thermo Scientific). Purified Fabs were concentrated using a 10 kD Millipore Amicon centrifugal filter.

Virus-like particles (VLP) of poliovirus serotypes 1, 2 and 3 were produced from yeast, preserved in sucrose and kindly provided by Prof. David Rowlands from University of Leeds. For further purification, VLP samples were laid on the top of a 15%-45% sucrose gradient buffer (in 50 mM HEPES, pH 7.4, 150 mM NaCl) and centrifuged at 29000 rpm for 3h at 4°C using a SW41 Ti Swinging-Bucket Rotor (Beckman) in an Optima XBN-80 ultracentrifuge (Beckman). The layer in the sucrose gradient containing poliovirus VLP was harvested.

~ 30μg of VLP of either poliovirus serotypes 1, 2 or 3 were separately mixed with purified Fabs from University of Leeds (~5mg) or Fabs from NIBSC (~6mg) in 1.5mL eppendorf tubes and incubated on ice for two hours. Then the samples were spun at 24000 g for 4.5 hours using an F2402H rotor in the Allegra X-30 R centrifuge. The supernatant was removed and 20μL of buffer (50 mM HEPES, pH 7.4, 150 mM NaCl) was added to dissolve the VLP-Fab complexes at the bottom of the eppendorf tubes. Ultrathin carbon Lacey grids (Agar Scientific) and Quantifoil 300 mesh R2/1 grids were glow-discharged at high intensity for 20s using a Plasma Cleaner PDC-002-CE (Harrick Plasma). In a Vitrobot Mark IV (Thermo Fisher) machine, 3μL of samples were applied to the freshly glow-discharged grids at 4.5°C, 100 % reported humidity. Extra liquid on grids was blotted by filter paper from the back of the grid for 5s, with a force of −1. The grids were frozen in liquid ethane and stored in liquid nitrogen.

2.5.3 cryo-EM data collection

Echovirus 11

Cryo-EM data were collected using a 300-kV Titan Krios microscope (Thermo Fisher Scientific, Waltham, MA, USA), equipped with a Falcon III detector (Thermo Fisher Scientific) and modified to operate with infectious particles. Data were recorded as movies (24 frames, each 0.25 s) in linear mode using the EPU software (Thermo Fisher Scientific) with a defocus range of −1 to −3 µm. The magnification was nominally 130,000×, corresponding to a calibrated pixel size of 1.05 Å. The dose rate was ~7 e/Å^2/s, resulting in a total electron dose of 41 e/Å^2.

Poliovirus-pAb

Cryo-EM data were collected as described in the previous section, except that the detector was upgraded to a Falcon IV (Thermo Fisher Scientific) mounted downstream of Selectris X energy filter (Thermo Fisher Scientific). Data were pre-processed during collection in CryoSPARC™ live (Structura Biotechnology). Parameters are listed in Table 2.5.3

Poliovirus VLP type	PV1 SC6b		PV2 SC5a		hPV2	PV3 SC8	
Polyclonal antibodies	pAb1	pAb2	pAb1	/	pAb1	pAb1	pAb2
Raw pixel size (Å)	0.932	0.7303	0.7	0.415	0.7303	0.932	0.932
Spherical aberration (mm)	2.7	2.7	2.7	2.7	2.7	2.7	2.7
Total exposure dose (e/Å^2)	30	30	50	47.5	30	30	30
EER number of fractions	30	30	50	40	30	30	30
Processed defocus average (µm)	0 - 4777	0 - 2946	6 - 2578	0 - 3236	0-3257	0 - 3144	2 - 4163
Accepted exposures	17,728	18,113	11,506	1,862	14,415	20,642	24,613

Table 2.5.3 Data collection parameters and pre-processing settings

hPV2: PV2 SC5a VLP heated at 52˚C for 10 min to generate expanded poliovirus particles.

2.6 EM data processing

In this section, the process of forming the structural results (shown in the next two chapters) from raw images (collected from the last section) is described in detail. Relion and CryoSPARC™ are the two main programs used for computational work. ChimeraX, Coot and Phenix [174] [220] [221] are the three main programs used for polishing and analysing the structural results.

2.6.1 Echo11-DAF

This project was started at the beginning of my D.Phil. and taken as far as a complex determination processed using Relion3. The project was subsequently restarted to utilize the tools that became available to perform symmetry expansion in CryoSPARC™. This more detailed analysis of the receptor interaction has now been published [222].

Single particle image processing in RELION

Frames of each movie were aligned and averaged using MotionCorr2 (version 1.3.0, Shawn Zheng, University of California, San Francisco, CA, USA) [223] and contrast transfer function (CTF) parameters were determined with CTFFIND4 (version 4.0.7, The Grigorieff lab, University of Massachusetts Chan Medical School, Worcester, MA, USA) [224]. Micrographs with significant drift or astigmatism were discarded. Particles were automatically picked using Warp [225]. Reference-free 2D-class averaging was performed. Reference based 3D classification and refinement was run using initial models generated by calculating a map filtered to 50Å resolution using the crystal structure of echovirus 11 (PDB: 1H8T) [226]. The gold-standard refinement procedure was used at all times during the determination of the orientation parameters of the particles [157]. Post-processing and CTF refinement were run in Relion 3 [156] to further improve the resolution of the cryo-EM density map. The final density map was calculated using 6394 particles from 6469 micrographs, with an overall resolution of 3.1 Å, estimated by the 0.143 Fourier shell correlation [227].

Single particle image processing in CryoSPARC™

To do symmetry expansion, cryo-EM data were re-processed using CryoSPARC™ (v.3.3.2). Patch motion correction (multi) and CTF estimation (Gctf) BETA were applied to 7088 micrographs. Particles were picked by blob picker, extracted with 42nm boxes, and selected by 2D classification. 10479 particles were subjected to Non-uniform Refinement (I1 symmetry), and the final result from Relion was used as an input volume. The particles were then expanded 60-fold by I1 symmetry expansion. A mask focusing on two symmetrical DAF densities at an icosahedral 2-fold area was created from a fitted DAF model with 10Å dilation radius and 3 Å soft padding width. An inverse mask was created for particle subtraction of the symmetry expanded particles. 3D variability analysis was applied, and 3 clusters were obtained, two of which showed one DAF and the other no DAF (corresponding to 31.5% DAF occupancy). Local refinement was performed on one of the clusters containing DAF (the other simply being symmetry related to this). After global and local CTF refinement, another round of local refinement was applied, and the final map was sharpened with a B factor of -181.5 $Å^2$.

Molecular model building

The crystal structure of E11 strain EV11-207 (PDB: 1H8T) [226] and the structure of DAF (PDB: 1OK3) [228] were fitted into the electron potential map in Coot 0.9.8.1 (Paul Emsley, MRC Laboratory of Molecular Biology, Cambridge, UK) [221]. The amino acid sequence was corrected to E11 strain 18-2135. The pixel size of the map was calibrated to 1.05 Å by assuming the particle size of the crystal structure was exactly right. The model was further improved using Phenix Real-space-refine (version 1.19.2-4158, The Phenix development team, multi-country) [174]. Refinement statistics are given in Table 2.6.1. The residues forming the E11-DAF interface were identified with PISA 1.48 (European Bioinformatics Institute, Hinxton, UK) [229]. Roadmaps were calculated using Rivem 5.1 (Chuan Xiao, University of Texas, El Paso, TX, USA) [230]. All figures were prepared with PYMOL2.5.2 (Schrodinger, Inc., New York, NY, USA) [231], Chimera 1.15 (University of California, San Francisco, CA, USA) [176] and ChimeraX 1.5 (University of California, San Francisco, CA, USA) [220].

E11-18-2135/DAF		
Data collection		
Voltage (kV)	300	
Frames	24	
Dose rate (e^-/ Å^2/ s)	7	
Total dose (e^-/ Å^2)	41	
Calibrated pixel size (Å)	1.05	
Defocus (μm)	-1 to -3	
Data reconstruction and model refinement		
	relion	cryosparc[1]
Movies	6469	7088
Particles	6394	201358[2]
Map resolution (Å)	3.1	3.93
Map sharpening B-factor (Å^2)	-178.1	-181.5
Model-to-map fit, CC_mask	0.88	0.54
R.m.s.d., bonds (Å)	0.003	0.003
R.m.s.d., angles (°)	0.55	0.581
All-atom Clash score	5.51	9.36
Rotamer outliers (%)	0.68	0.80
Ramachandran plot		
Favored (%)	97.57	98.01
Allowed (%)	2.43	1.95
Outliers (%)	0.00	0.04

Table 2.6.1 Data collection, reconstruction and model refinement. 1: CryoSPARC™ was used to refine DAF binding area. 2: I1 symmetry expansion was applied to particles, which increases the particle numbers 60 times.

2.6.2 Poliovirus VLP – pAB

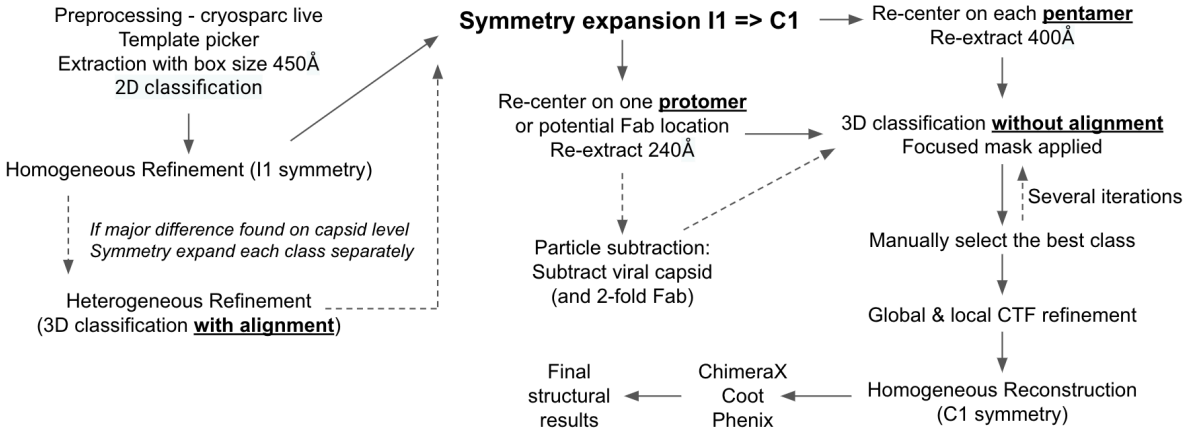


Figure 2.6.2.1 EM data processing workflow for poliovirus VLP – pAb datasets

Poliovirus VLP – pAb data collected on a Titan Krios microscope (Thermo Fisher Scientific, Waltham, MA, USA) were pre-processed by CryoSPARC™ live. Particles were picked by a template picker using poliovirus VLP from another dataset as template, extracted (box size 450Å) and 2D classified. The best 2D classes were chosen for homogeneous refinement using poliovirus VLP from another dataset as template (Figure 2.6.2.1 left). Heterogeneous refinement was performed with I1 symmetry to all datasets and different classes were only found for PV1 (these were natural and expanded particles). 3D reconstructed volumes either from homogeneous or heterogeneous refinement were symmetry expanded from I1 symmetry to C1 symmetry, which generates 60 times more data per particle. Then the data processing diverges depending on whether the purpose is a Fab check or a Pentamer check.

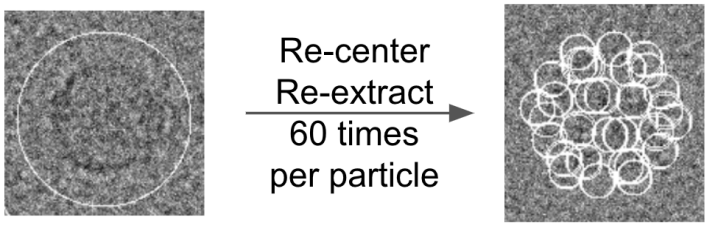


Figure 2.6.2.2 Demonstration of re-center and re-extract after symmetry expansion

For further investigation of the Fab binding pattern, a smaller box (box size 240Å) was re-centered at potential Fab binding epitopes (on the surface of viral capsid) and re-extracted 60 times for each virus particles in icosahedral symmetrized locations of the viral surface (Figure 2.6.2.2). Given that poliovirus VLP is assembled from 60 protomers arranged with icosahedral symmetry, each re-extraction box is in the same relative position with its nearby protomer. Therefore, the re-extracted particle can present every single epitope rather than averaging the 60 signals, as was done in the previous refinement jobs.

A similar approach was used for analysis on a per-pentamer base, with the extraction box centered at the center of each pentamer outer surface, and the box size was larger (400Å). In this case, each particle was re-extracted 60 times, with each of the 12 pentamers re-extracted 5 times in 5 equally split orientations (Figure 2.6.2.2).

After re-centering and re-extraction, a homogeneous reconstruction job (C1 symmetry) was performed as validation, and in some cases (PV1-NIBSC) an extra particle subtraction step was necessary to remove strong signals (viral capsid and 2-fold Fabs) and reveal weak signals (minor Fab clusters). Afterwards, iterations of 3D classification without alignment with different parameters and mask settings were executed. At the end of each classification job, the output volumes and classes were examined manually using ChimeraX, and particles from the ideal classes were selected for the next iteration (Figure 2.6.2.1 right).

Number of classes		2/5/10	5/10/20/100	5/10/20/40/100
Initial volume mode		Input	Simple	PCA
	Particles per reconstruction	/	1/1000	1
	Number of reconstructions	/	/	100/2000/10000
	Number of components	/	/	1/2
Focus mask		5-10A dilation of input, cylinder R30-60 H40-60, sphere R30/R40/R50		
Solvent mask		same as focus mask / auto solvent mask (threshold 0.1-0.2, 10A-20A)		
Per-particle scale		none / input / optimal		
Target resolution		4-8-12		

Table 2.6.2.1 3D classification without alignment - initial step

Online expectation maximization		
	Number of epochs	1,2,3,5
	Batch size per class	100, 1000, 10000
	Learning rate initial	0, 0.4, 0.75, 1
	Learning rate half-life	50% 80% 100%
Full expectation maximization		
	Number of iterations	1,2,25
	Convergence criterion	1% 2% 5%
	RMS density change	/ 0.01 0.005 0.001
Class similarity		0, 0.5
Force hard classification		yes / no

Table 2.6.2.2 3D classification without alignment - iteration steps

To extract the weak signal of multiple different Fabs, I performed extensive testing of 3D classification jobs with different parameter and focused masks combinations. The parameters tested are listed in table 2.6.2.1 (initial step parameters) and table 2.6.2.2 (iteration step parameters). Parameters marked in red were found to be the ideal combination, however this is heavily case-dependent and other black parameters may produce better results in other situations. Those section of the table without red marked parameters are of less significance to the final results.

Explanation of key parameters:

Initial volume mode:
simple mode: reconstruct initial volumes from randomly selected particle subsets.
PCA (Principal Component Analysis) mode: reconstruct initial volumes from cluster-average maps computed after applying PCA to a large set of reconstructions.
input mode: use input volumes.

PCA/simple - particles per reconstruction: Number of particles used to compute each cryo-EM density initialization. I normally use simple and 1 particle for each initial density.

PCA - number of reconstructions: Number of reconstructions which will be used in PCA.

Masks: 3D Classification accepts two different types of masks. A solvent mask *S*, and a focus mask *F*. During optimization we use the following real-space volume for all likelihood computations of class *k* ($\bar{V}$ is the consensus reconstruction) :

$$V_k \leftarrow S * (F * V_k + (1 - F) * \bar{V}),$$

The masks were generated in ChimeraX, a cylinder mask with certain radius(R) and height(H), or sphere with specific radius. All masks manually generated were soft padded 12Å in width. Mask generation is very case dependent, see Chapter 4 for details.

Per-particle scale: No-scales means all particles will have their per-particle scales reset to 1.0 (useful for very small particles or strange cases). Input scales means input scale factors will be used (which may have come from another refinement). Optimal means optimal per-particle scales will be computed prior to classification. I use input.

Target resolution (Å): Set this based on the resolution at which you expect to find significant variation in conformations.

Online expectation maximization (O-EM): compute with partial dataset

Number of epochs: Number of epochs (traversals through the entire dataset) to perform during online expectation maximization (O-EM). Default setting is 2, I use 1 for first round and 2 or 3 for later rounds.

Batch size per class: Number of particles per class to use during online EM. Default setting is 1000, I use 1000-10000 for first few rounds of classification and 100 for final round.

Learning rate initial: Learning rate defines the linear update rule at each O-EM class density update. 1 means total replacement with new volumes, 0 means no change from previous iterations. The developers recommend increasing/decreasing this value in 0.1 increments, with smaller values encouraging a larger set of classes with smaller density variation, and vice-versa. Default setting is 0.4, I normally use 1 and raise the number of epochs to ensure learning rate is 0 in the end.

Learning rate half-life: Half-life (expressed as % of total online EM iterations) for learning rate annealing during online EM. Set to 0 for a fixed learning rate. Default setting 50% is good.

Full expectation maximization (F-EM): compute with whole dataset

Number of iterations: Classification will stop after this many F-EM iterations even if convergence criteria are not met. Default setting is 25, but I find the results are very similar after 5+ rounds, so I normally set it to 1 for first round of classification, 5-10 for further steps.

Convergence criterion: Primary stopping criterion. Stop full-EM when the percentage of particles that have changed classes across iterations falls below this value. Default setting is 2%, I use 2% for primary steps and 1% for final steps.

RMS density change: In addition to class switches, monitor the root mean square (RMS) of the density change of each class across iterations. This can help stop the optimization when some particles have high probability of belonging to multiple classes. Threshold on the RMS of density change across iterations (averaged across voxels and classes, normalized by the RMS of the consensus volume voxels, and weighted by relative class size). Optimization will stop when the mean of this metric across 2 consecutive full-EM iterations falls below the supplied threshold. Default setting is 0.01, I turn off this function for the first round of classification, normally use 0.01 for middle rounds, and 0.001 for final classification.

Class similarity: Expected similarity of structures from different classes. A number between 0 and 1, where 0 means classes are independent, and 1 means classes are very similar. Default setting is 0.5, I use 0.

Force hard classification: This function will force each particle to only be assigned to one class at every iteration, rather than having partial assignment to all classes. Default setting is no, I set yes.

Once the best class of Fab was picked out, global and local CTF refinement were applied to the particles and a round of homogeneous reconstruction to finalize the result. After that, the volume was output from CryoSPARC™ and input to Coot/ChimeraX for further analysis. Since the amino acid sequence of the polyclonal Fabs are unknown, structures were not built into the cryo-EM density volume, only poliovirus protomers and pentamers were fitted to the viral capsid volume using Coot/ChimeraX/Phenix (Figure 2.6.2.1).

2.6.3 SyRe protocol

SyRe protocol is the short version of a series of jobs running in CryoSPARC™ (version 2 to version 4) that I developed for the experiments in chapter 4. The SyRe protocol only refers to 4 jobs including symmetry expansion, re-center, re-extraction and re-construction, running after any 3D reconstruction / 3D refinement jobs that involve enforcing point-group symmetry, e.g. homogeneous refinement.

Symmetry expansion

Input the particles from homogenous refinement job. Apply I1 to the symmetry group setting and run the job.

Volume alignment tool (re-center)

Input the volume from the output of homogeneous refinement job. Input the particles from the symmetry expansion job. Type in the 3D coordinates of new center (voxels) under the list of re-center parameters and run the job. There are many ways to find the desired coordinates. I use the mark tool in ChimeraX, and it will show the coordinates you marked in the log panel.

Extract from Micrographs (re-extraction)

Input the output particles of volume alignment tool. Choose the extraction box size of 400Å for pentamer-scale study or 240Å for protomer- / Fab- scale study. Since the output is 60 times multiplied the original particles, it is recommended to Fourier-crop to a ¼ smaller box size (pixel).

Homogeneous Reconstruction only (re-construction)

This step is a sanity check for SyRe protocol. Input the extracted particles and check the output volume in ChimeraX.

2.7 Nanodisc experiments

The original protocol of lipid preparation and nanodisc assembly were provided by Dr. Pranav Shah and modified by the author.

2.7.1 Lipids preparation

50µl NTA (5mg/ml), 200µl POPG (25mg/ml), 300µl POPC (25mg/ml) were drawn from chloroform stocks, mixed in a clean glass tube (length>10mm). Argon was pumped into the tube to dry out the lipids and the tube was vigorously vortexed to evenly distribute the dried lipids. The tube was placed in a vacuum desiccator overnight to dry out the lipids further. 500ul Buffer (20mM Tris, pH=7.5, 200mM NaCl, 75mM Na-Cholate) was added to the tube to dissolve the lipids. This was vortexed followed by 5s water bath sonication and these steps were repeated several times till the glass tube became clear again. Note that the dissolving step needs to be done at 4℃.

2.7.2 Nanodisc assembly

500µl MSP solution (from 3.1 or 3.2), 500µl Lipids solution (from 7.1) and 500µl Buffer (20mM Tris, pH=7.5, 200mM NaCl, 75mM Na-Cholate) were mixed and slowly spun at 4°C for 1h. 500µl dried biobeads were added to the mixed sample and the sample was slowly spun at 4°C for 2h. The sample was then spun at 1500rpm for 1 min to remove the biobeads. After that, the sample was loaded on Superose 6 10/300 (Sigma-Aldrich) on an AKTA and eluted with Buffer (20mM Tris, pH=7.5, 200mM NaCl), with the flow rate set to 0.05ml/min. The elution fraction under the UV280nm absorption peak at around 12.5ml position was collected for further usage.

2.7.3 SCARB2 incorporated nanodiscs

An excess of SCARB2 was mixed with nanodisc at 4°C for 1h before loading on a size exclusion column again (as in the previous step). The two UV absorption peaks for SCARB2 incorporated nanodisc and unbound SCARB2 were collected separately.

2.8 Thermofluor experiment

PaSTRy: Particle Stability Thermal Release Assay [232] was used for studying the environmental trigger of EV71 cell entry. Fluorescent dyes were obtained from Molecular Probes (Life Techologies, Paisley, UK); SYPRO red (S-6653) and 5 mM stock of SYTO9 (S-34854) are supplied in DMSO (dimethylsulphoxide). Virus particles and virus receptor were purified as described in the previous section.

50 μL volume reactions were set up in each well of a transparent 96 well plate (low profile skirted plates AB-1000/w, Thermo, for the BioRad instrument), including 2nM EV71, 4uM SCARB2, 5uM SYTO9 or 3X SYPRO red, and filled up by Buffer (citric acid - NA_2HPO_4 pH4.5-7.0) at 4°C or on ice.

Buffer Na_2HPO_4, MW 141.98; 0.2 M contains 28.40 g/L and citric acid monohydrate, $C_6H_8O_7$ • H2O, MW 210.14; 0.1 M contains 21.01 g/L

pH	4.5	5.0	5.5	6.0	6.5	7.0
0.1M citric acid	54.6%	48.5%	43.1%	36.8%	29.0%	17.6%
0.2M NA_2HPO_4	45.4%	51.5%	56.9%	63.2%	71%	82.4%

Table 2.8 Buffer component

Once the reactions in each well were set up and mixed properly, the 96 well plate was centrifuged at 2000 × *g* to remove any bubbles. The plate was then sealed using optically clear foil (BioRad Microseal B, MSB-1001) and set up in an MX3005p qPCR machine (Agilent, Edinburgh, UK). The plates were heated from 25 to 99 °C, and the fluorescence readings were recorded in triplicate every 1 °C, taking approximately one hour to complete.

2.9 Phylogenetic analysis

A structure-based phylogenetic tree was drawn (Chapter 3) using SHP (David Stuart, University of Oxford, Oxford, UK) [233] and a sequence-based tree using ETE3 3.1.2 (Jaime Huerta-Cepas, EMBL, Heidelberg, Germany) [234]. This part was performed by Dr. Daming Zhou.

Chapter Three

Echovirus11 – DAF

Major achievements:

1. Structure of the complex of echovirus 11 and the full length ectodomain of its attachment receptor DAF is determined for the first time.

2. A glycan connecting DAF and Echovirus 11 is discovered, but the function of the glycan remains unknown.

3. Only a maximum of 30 DAFs can attach to one Echovirus 11 at the same time, not 60 DAFs as reported previously.

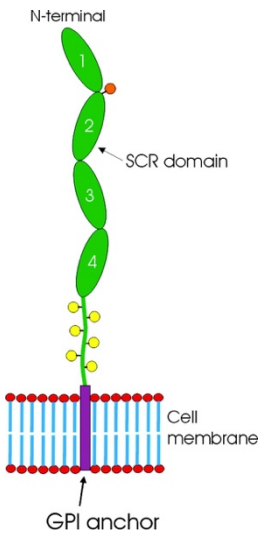
4. Two distinct binding modes of DAF with 19 different enteroviruses are classified, and a potential evolutionary history of those enteroviruses is proposed based on phylogenetic analysis.

3.1 Introduction

Echoviruses are responsible for a range of human diseases, usually mild, like hand, foot and mouth disease, but sometimes severe including aseptic meningitis, myocarditis and encephalitis [235] [236] [237]. Of all types of echoviruses, Echovirus 11 is the most frequent cause of serious neonatal disease and death [238]. Currently, there are no licensed drugs for echovirus infection and no available vaccines.

Echoviruses, non-enveloped viruses with a positive single-stranded RNA genome of ~7500 bp, belong to the species enterovirus B of the genus Enterovirus, the most populous genus of the family Picornaviridae. Enteroviruses are structurally characterized by a depression called the "canyon", encircling the 5-fold axes of symmetry of the capsid, that was initially proposed to be the binding site of IgG-like picornavirus receptors [239]. A number of uncoating receptors were subsequently confirmed to bind the canyon [17] [18], although this is not universal [19]. In echoviruses the canyon is not continuous (as is the case with species A and C enteroviruses, which include polioviruses, a range of Coxsackie viruses and Enterovirus A71 (EV71)) but is split into five pits where the uncoating receptor (neonatal Fc receptor or FcRn) binds [240].

DAF is one of the regulators of the complement system, inhibiting formation of the complement convertases in both the classical and alternative pathways [17] [18] [241] [242] [243]. DAF also functions in signal transduction in T cells [244]. It is a membrane glycoprotein, widely distributed on the surface of all types of cells that are in contact with plasma complement proteins and attached to the lipid bilayer by a C-terminal glycosylphosphatidylinositol (GPI) anchor (see figure below). The extracellular region of DAF is composed of four short consensus repeats (SCR1-4, see figure at right)) [228] [245]. Many echoviruses have been shown to use DAF as an attachment receptor [246] [247] and several structures of enteroviruses in complex with portions of DAF have been published [240] [248] [249] [250] [251].



The published structures reveal that DAF has been seen to bind in different ways to different enteroviruses. Since there is substantial divergence in the sequence of P1 between E11 and other DAF-binding enteroviruses, we determined the structure of E11 in complex with DAF at a resolution of 3.1 Å to establish the precise mode of interaction. This structure reveals that SCR 3 and 4 of DAF and the VP2 EF loop and VP3 BC loop of E11 are involved in the interaction and an N-linked glycan on DAF also interacts with the E11 capsid. We were able to classify the modes of DAF binding into two distinct poses which we propose evolved independently.

3.2 Structure of the Echovirus 11 - DAF complex

The cryo-EM structure of the E11-DAF complex at neutral pH (pH 7.4) was determined at a nominal gold-standard resolution of 3.1 Å (see Methods). The cryo-EM density for the virus is of high quality (Figure 3.2.2C) and the structure closely resembles the crystal structure of isolated mature E11 (PDB: 1H8T) [226], RMSD in Cαs 0.4 Å, although the identity of amino acids between these two strains is only 90.3%. In contrast, the density of the DAF was weak. Whilst at low resolution the molecular envelope of DAF was clear (Figure 3.2.2AB), at high resolution the density became fragmentary at a contour level where the capsid density was still continuous.

As expected for engagement with an attachment receptor with relatively weak binding (reported K_D for E11 ~3.0 μM, k_{on} ~10^5 $M^{-1}{\cdot}s^{-1}$,k_{off} ~0.3 s^{-1} [252]), which is not responsible for internalisation and genome release [240], the E11 structure is in its un-expanded state with the natural pocket factor (modelled as sphingosine) bound in the VP1 pocket (Figure 3.2.2D).

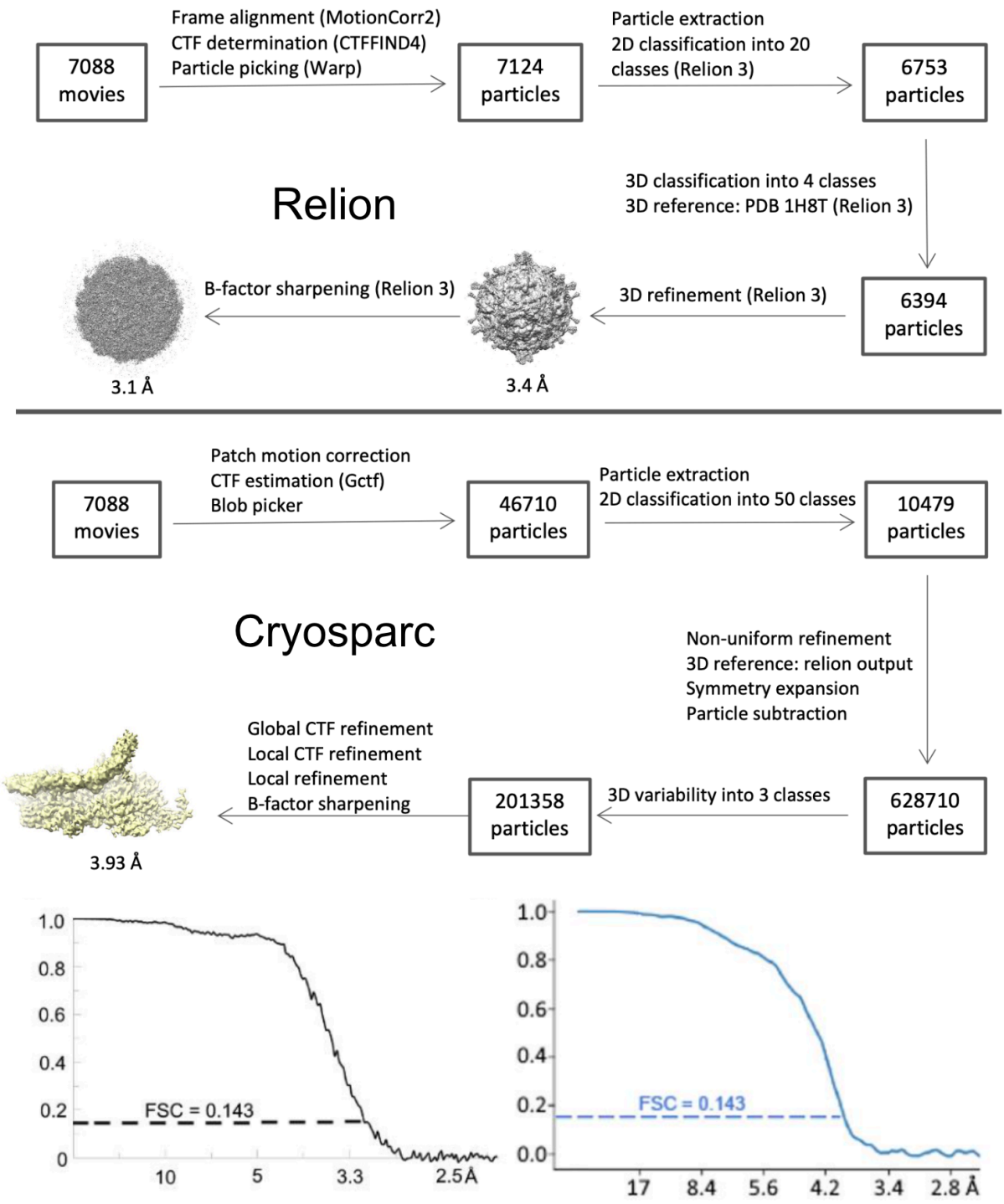


Figure 3.2.1 Computational workflow for Echovirus11 - DAF complex data analysis (relion) and single DAF focused structure data analysis (CryoSPARC™). **Bottom: FSC curve** (black) of the E11-DAF complex with the threshold 0.143, the final resolution is 3.1 Å (calculated by Relion). FSC curve (blue) of the local refined map centred on DAF with the threshold 0.143, the overall resolution is 3.9 Å (calculated by CryoSPARC™).

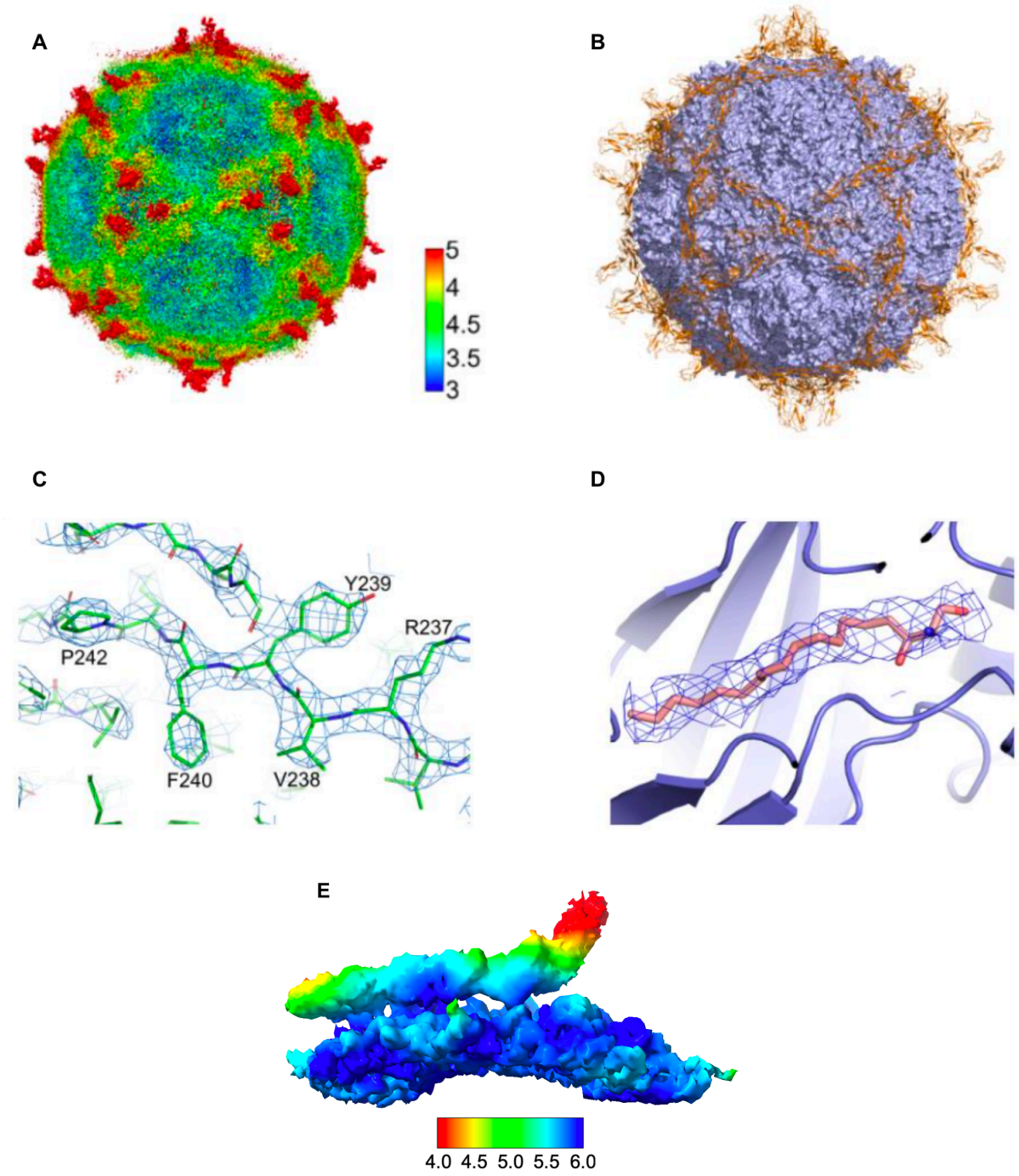


Figure 3.2.2 Overall structure of E11-DAF complex. (A) Local resolution map of E11-DAF complex. (B) 3D reconstruction of E11-DAF complex with fitted DAF shown as cartoon. (C) Representative density of E11 viral capsid. (D) Cryo-EM density of the pocket factor. (E) Local resolution map of E11-DAF complex solved by cryosparc.

3.3 Improved DAF cryo-EM density

In order to improve the density and characterize the interaction, symmetry expansion and selection of DAF-occupied sites by variability analysis and 3D classification was performed (see method). This analysis was performed in CryoSPARC™ and improved the density allowing, where there were contacts with the virus, some larger side chain orientations to be determined. Thus, the analysis selected the occupied sites, producing density of sufficient quality that the virus-receptor interactions described below are secure.

The internal structures of the four SCR domains of DAF are closely similar to those of the crystal structure (PDB: 1OK3) [228], although the relative position of SCR 1 is significantly different, which may be caused by crystal packing in the isolated molecule (Figure 3.3.1 right).

To investigate the potential clashes between two DAF molecules bound close to the same icosahedral 2-fold axes (Figure 3.3.1 left), a 3D classification job in CryoSPARC™ with focused mask was also performed (Figure 3.3.2, not described in method). The classification clearly points out that two DAF cannot bind at the same 2-fold axes and indicated that the average number of DAF molecules bound per particle was ~20.

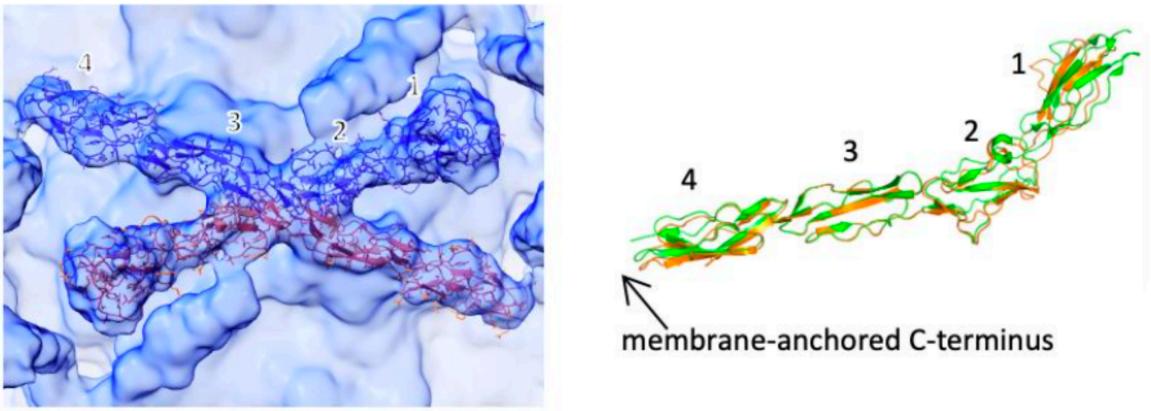


Figure 3.3.1 Left: Close-up of the Cryo-EM reconstruction of the E11-DAF complex, showing density for two DAF molecules (orange and red) related by the icosahedral 2-fold. **Note:** domains SCR 2 and 3 of these two DAF molecules clash with each other. **Right:** Superimposition of the E11 bound DAF (orange) with that determined by crystallography (green, PDB: 1OK3).

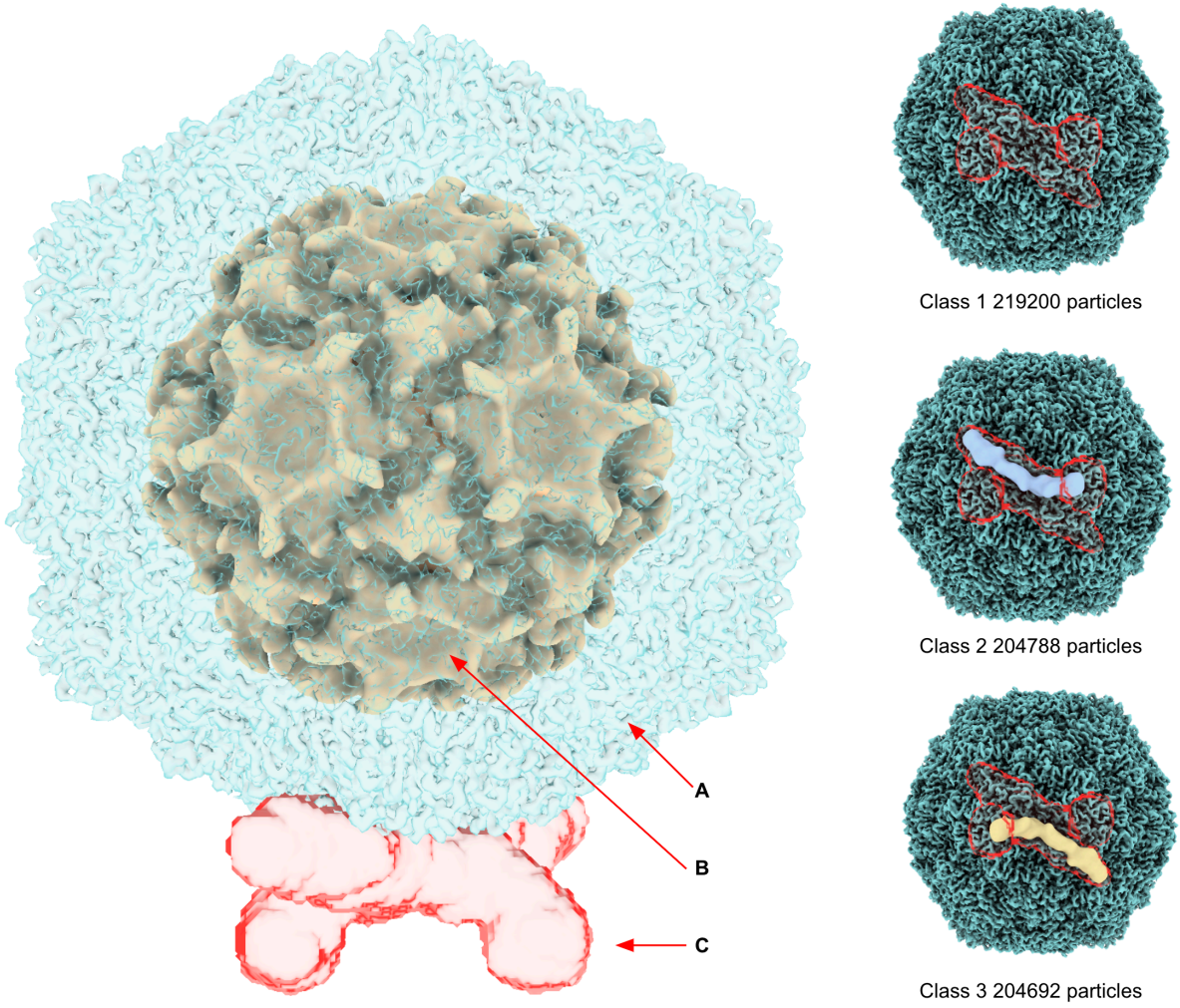
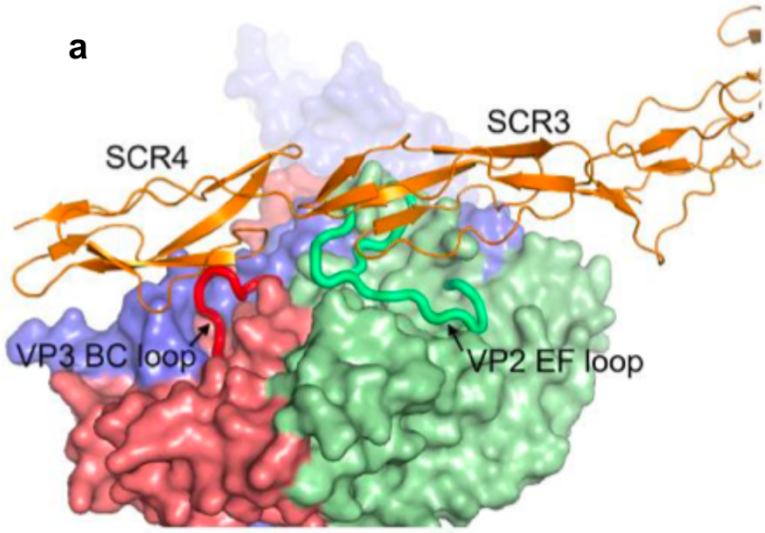


Figure 3.3.2 DAF-focused 3D classification. A. Particle subtraction: viral capsid. B. Remaining signal (genome). C. 3d classification with focus mask

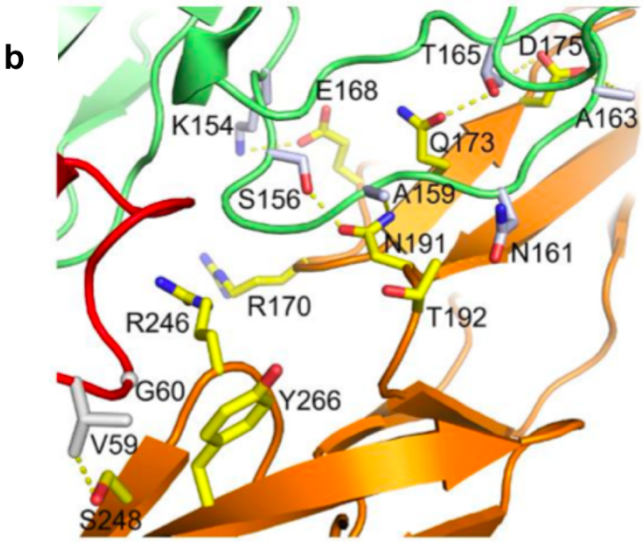
3.4 Echovirus 11 - DAF interaction

DAF binds E11 at the southern rim of the canyon, rather than in the canyon itself. This binding pattern is reminiscent of that of SCARB2 binding to EV71 [19], however, SCARB2 is an uncoating receptor whilst DAF is not. The footprint of the DAF receptor on the virus is ~900 Å2 (Figure 3.4.2top). The VP2 EF loop of E11 and SCR 3 of DAF dominate the interaction, although the VP3 BC loop of E11 and DAF SCR 4 are also involved (Figure 3.4.1ab). Detailed interactions are listed in Figure 3.4.2 bottom.

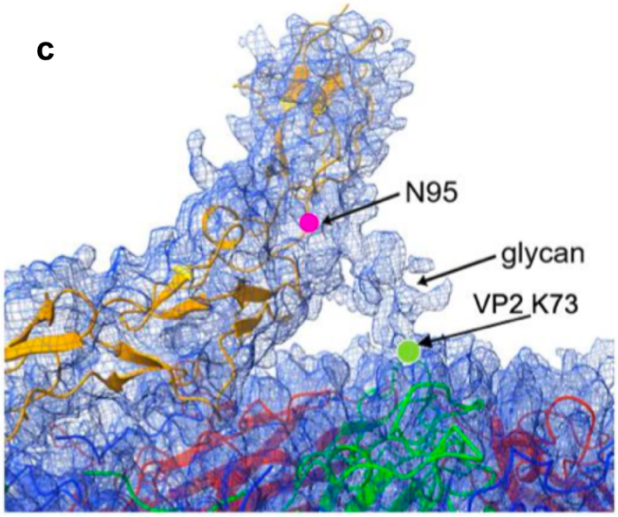
Density for the glycan at residue 95 of DAF SCR1 can be clearly seen in the cryo-EM map and this glycan makes an interaction with the capsid of E11 (Figure 3.4.1c), which was neither observed in a previously published E11-DAF structure (PDB: 6LA5), since that DAF construct only included SCRs 3 and 4, nor in other enterovirus-DAF structures. The density for the glycan is not well enough defined to describe the interaction in detail, however it is clear that the BC loop of VP2 of E11 is involved, centered on Lys73. Glycans are frequently used as attachment receptors for viruses, and we note that for foot and mouth disease virus a glycan on the integrin receptor was observed to make an interaction with the virus capsid at the point where heparan sulphate also bound [253]. It is therefore interesting that heparan sulphate has also been found to act as an attachment receptor in some echoviruses, including some that also bind DAF [254].



(a) SCRs 3 and 4 of DAF (orange), and the VP2 EF loop (green)and VP3 BC loop (red) of E11 are involved in E11-DAF interactions. The viral protomer is drawn as surface representation with the two loops involved in contacts with DAF shown as coils. VP1, 2 and 3 of E11 are coloured in blue, green and red, respectively.

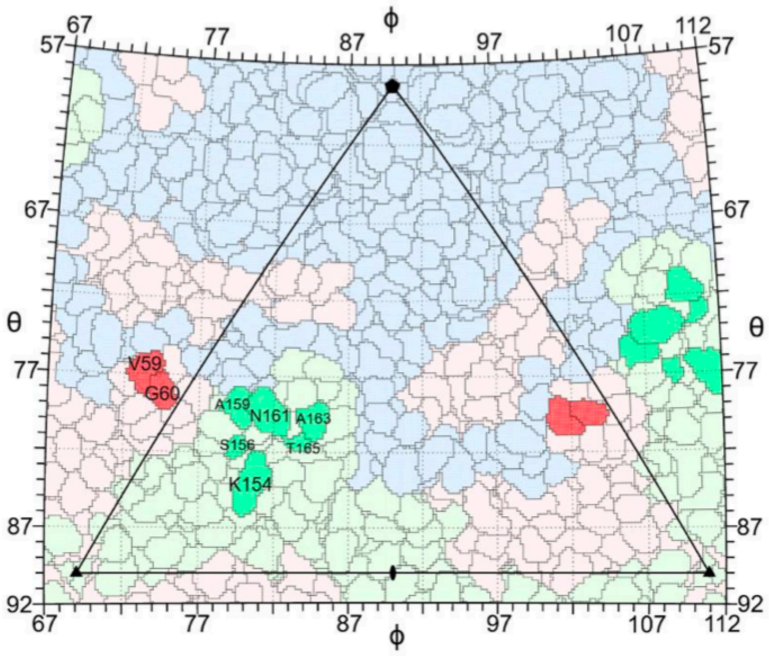


(b) Binding residues at the E11-DAF interface (E11: VP2 green, VP3 red, DAF orange). Side chains of E11 are shown as grey sticks and those of DAF shown as yellow sticks.



(c) Density showing contact between the Glycan attached to residue N95 of DAF (shown as a magenta circle) and residue K73 of VP2 (marked with a green circle).

Figure 3.4.1 interactions between E11 and DAF



Residue in E11	Residue in DAF	Distance (Å)
Potential hydrogen bond		
VP2 154 LYS	168 GLU	2.60
VP2 156 SER	191 ASN	3.05
VP2 159 ALA	192 THR	3.16
VP2 161 ASN	173 GLN	3.57
VP2 161 ASN	192 THR	3.66
Potential salt bridge		
VP2 154 LYS	168 GLU	3.52
Potential hydrophobic interaction		
VP2 159 ALA	191 ASN	3.93
VP2 163 ALA	175 ASP	2.74
VP2 165 THR	173 GLN	3.77
VP2 165 THR	175 ASP	3.74
VP3 59 VAL	248 SER	3.70
VP3 60 GLY	246 ARG	2.63

Figure 3.4.2 Top: Roadmap [230] showing the residues of E11 involved in DAF binding
Bottom: List of protein interaction between E11 & DAF

3.5 Two binding modes of DAF to enteroviruses

At least 19 enteroviruses (E3, E6, E7, E11-13, 19-21, E24-25, E29-30, E33, Enterovirus 70 (EV70), Coxsackievirus A21 (CVA21), CVB1, 3 and 5) use DAF as an attachment receptor. The reported structures of DAF with 6 different enteroviruses cluster into two distinct patterns of DAF binding which we term the E6 pose and the E11 pose (Figure 3.5.1a). The orientation of DAF is markedly different between these poses. In the first pose (E6, E30 and CVB3) DAF binds with SCRs 3 and 4 sitting above and interacting with mainly VP2 as the DAF runs across the southern rim of the canyon at a slight angle with SCR2 interacting with the VP1 & VP3 C-termini from a neighbouring protomer, (Figure 3.5.1a). The second pose is exemplified by our structure of E11-DAF and is shared by E7 and E12. In this second pose DAF SCRs 3 and 4 bind at the southern rim of the canyon but are displaced clockwise around the rim by almost the length of an SCR and are pivoted clockwise by approx. 60° relative to the E6 pose so that SCRs 3 and 4 run along the canyon rim interacting with VP2 and VP3, whilst SCRs 1 and 2 project outwards from the canyon. (Figure 3.5.1a).

In the E6 pose, SCRs 2, 3 and 4 of one DAF molecule and two protomers of the capsid are involved in the interaction whilst in the E11 pose, only SCRs 3 and 4 and one protomer are directly involved, with the glycan of SCR1 interacting with a second protomeric unit. As a result of the differences a maximum of 30 DAF molecules can attach to E11, due to steric clashes near the 2-fold axis, whereas 60 copies of DAF can attach to the capsid in the E6 pose.

A structure based phylogenetic tree shows that the capsid structures cluster in-line with DAF binding with E6, E30 and CVB3 forming one branch and E7, E11 and E12 the second (Figure 3.5.1b). To investigate how the virion structure/sequence correlates with DAF binding, a sequence based phylogenetic analysis of the 19 identified DAF binding enteroviruses was performed (Figure 3.5.1c). Whilst E7, 11 and 12 partition to a single branch, E6, E30 and CVB3 are spread across the tree, suggesting that the viruses with each binding pose of DAF have coherent and distinct evolutionary histories. It seems plausible that the E6 binding mode is more extensive and more ancient, with the E11 pose viruses arising from a single, later, switch (Figure 3.5.1c).

Close examination of the capsid sequences of the viruses in the two distinct DAF binding clades shows that E11-pose viruses (E7, 11 and 12) have a glycine at residue 162 of VP2 while E6-pose viruses mostly have larger asparagine or aspartic acid residues at this position: VP2 162N in E6 and VP2 162D in E30, although CVB3 has VP2 162S. In support of this, it has been reported that a single amino acid substitution G162E in VP2 caused the loss of E11 affinity to DAF [255]. Our structure confirms that a longer side chain at this position would clash with DAF in the E11 pose (Figure 3.5.2 bottom), so VP2 162 is a key residue controlling DAF binding pose. In addition, further residues involved in binding, VP1 269/270, VP2 165, VP3 76 of E11-pose viruses and E19 are conserved (Figure 3.5.2 bottom), suggesting a role in controlling the DAF binding pattern, and corroborating the inference from the phylogenetic analysis that E19 belongs to the E11-pose group.

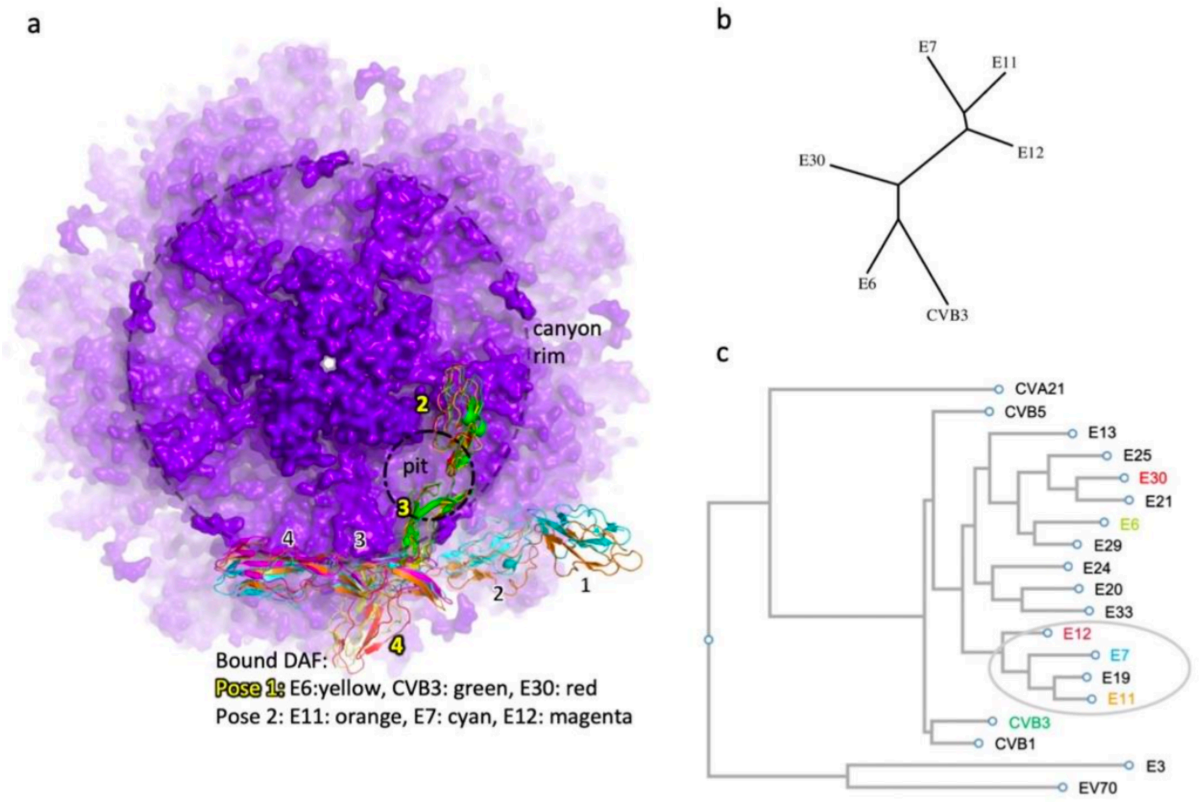
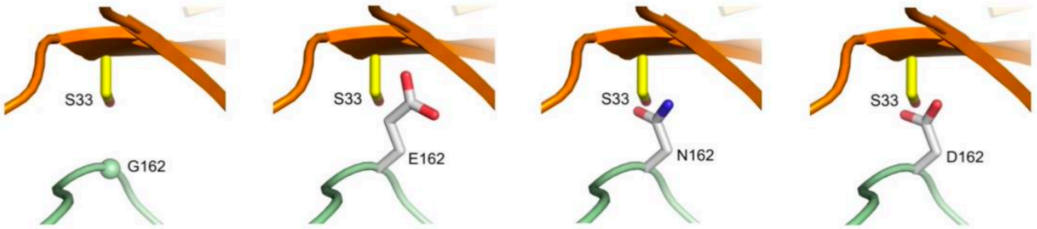


Figure 3.5.1 Structural and phylogenetic analysis of 2 binding modes (a) Structural comparison of DAF bound with different enteroviruses. The viral capsid is shown as surface representation, one pit region in the canyon region of the capsid is marked by a dashed circle and the outer rim of the canyon is marked by a larger dashed circle. DAF molecules are shown in cartoon representation with different colours indicating the different viruses they bound with.
green: CVB3, PDB: 7VY5; yellow: E6, PDB:6ILK; red: E30, PDB:7C9W; cyan: E7, PDB:3IYP; orange: E11, as reported here [222], PDB:8B8R; magenta: E12, PDB:1UPN. (b) Phylogenetic tree of 6 DAF binding enteroviruses based on an alignment of VP1-3 concatenated into a single PDB. (c) Phylogenetic tree of 19 DAF binding enteroviruses based on the capsid sequences (colours as in (a)).



| E11 pose | VP1 | | | | | | | | | | | | VP2 | | | | | | | | | | | |

3.6 Discussion

Structures of enterovirus-DAF complexes reveal two distinct DAF binding patterns which we denote the E6 and E11 poses, with the complex structures observed for six different enteroviruses partitioning equally between the two groups. The E11 pose observed has been corroborated by mutational analysis [255]. Taking our structure of E11/full-length DAF together with previously reported results [240 248 249 250 251] suggests that VP2 162 is important in determining the pose adopted by DAF. Although this diversity of poses for a common receptor on related viruses might appear surprising it is known that whilst the underlying mechanism of virion assembly and hence overall capsid structure is usually highly conserved within virus lineages, the surface of the virion, which modulates antigenicity and interactions with cell surface receptors, can evolve quickly [256] allowing viruses to modify tissue tropism. It is indeed likely that escape from antibody neutralization contributes to more rapid receptor diversification. In line with this, different enteroviruses use a wide variety of receptors. DAF-binding enteroviruses use DAF as an attachment receptor whilst other receptors, typically FcRn, trigger capsid expansion and uncoating. In line with this DAF binding is relatively low affinity for both poses, being reported as ~3 μM for E11 and ~0.4 μM for E6 [240 252]. The viruses attached to similar domains of DAF for both poses, resulting in a similar distance between the virus and cellular membrane. However, the two DAF poses described are quite

different, with no common interactions between the two. It might therefore be supposed that DAF binding evolved independently in each clade, presumably conferring increased infectivity and a selective advantage. Taking the structural information with the sequence-based phylogeny (Figure 3.5.1b,c) suggests indeed that the two clades are distinct, however it also suggests that the E6 pose was discovered first and is still the most common pose, whereas the E11 pose arose at some point through a switch in binding mode, since although there are no common interactions between the two poses, they cannot be occupied at the same time (Figure 3.5.1a). It is conceivable that the addition of the glycan interaction conferred a slight advantage, enough to fix the E11 binding pose in the population and create a new virus species, although as noted above the binding is reported to be relatively low affinity for both poses.

In summary, it is clear that the functional role of cell attachment can be fulfilled by a variety of binding modes, and even specific protein–protein binding modes can evolve relatively easily, mirroring the ease with which many picornaviruses can adapt to tissue culture by acquiring the ability to bind cellular glycans, e.g., heparan sulphate [257 258]. Once acquired such binding will then act as a constraint (unless supplanted by a more effective interaction), leaving an evolutionary footprint on both the structure and sequence of the virus, which is reflected in the clean separation of the DAF poses into two clades on the basis of the virion structure (Figure 3.5.1b).

Chapter Four

Poliovirus VLP - polyclonal antibodies

Major achievements:

1. Developed SyRe protocol that can find neglected absent pentamers in enteroviruses and is capable of separating out minor classes of polyclonal antibodies (to a minimum number of 1000 particles per class)

2. Using the SyRe protocol, 3-4% absent pentamers are found in non-expanded poliovirus VLPs and this led to the discovery of an unexpected antibody-antigen epitope at the interface of adjacent pentamers which only becomes available at the edge of an absent pentamer

3. Discovered a semi-attached pentamer status

4.1 Introduction

Poliovirus is a small non-enveloped RNA virus, measuring around 30nm in size. It falls within the Enterovirus genus of the Picornaviridae family and is responsible for causing poliomyelitis. The viral icosahedral capsid comprises four proteins: VP1, VP2, VP3, and VP4, which encloses its genetic material [259], and shares structural similarities with other enteroviruses. Poliovirus enters cells by binding to its receptor, CD155 (also called poliovirus receptor or PVR) [26], an immunoglobulin-like molecule located at the junctions between epithelial cells [260]. This binding leads to the release of the "pocket factor" [261] , a stabilizing ligand [262] found within VP1's hydrophobic core [263]. Structurally, receptor attachment causes a 4% expansion of the icosahedral capsid [264], resulting in a 135S or A-particle. The 135S particle is believed to represent a critical step along the pathway to virus infection [265]. The 135S particles have holes in the capsid at the icosahedral 2-fold and quasi-3-fold axes, unlike native virions whose capsids form a closed surface. The holes permit the externalization of the N-terminal extension of viral capsid protein VP1, which interacts with membrane [266] [267] and presumably VP4, which is myristoylated [268].

Similar expansion of the viral capsid triggered by receptor attachment can also be achieved by heating [269], converting poliovirus from native D antigen to C antigen form (non-infectious to human but weakly infectious to Chinese hamster ovary and murine L cells) [270] [271]. Convalescent sera primarily react with the D antigen, while sera from the acute phase of poliomyelitis primarily target the C antigen [272]. As individuals recover from the disease, antibodies against the D antigen are developed. This led to the assumption that the D antigen held the protective immunogenic properties, suggesting that the content of D antigen was crucial for the efficacy of inactivated polio vaccine [273].

To avoid confusion in what follows the 160S D antigenic poliovirus will be termed the natural particle and the 135S C antigenic particle will be termed the expanded particle.

The identification of three key antigenic sites (sites 1, 2, and 3), responsible for poliovirus neutralization, has been achieved through the isolation and characterization of Sabin mutant strains that display resistance to poliovirus-specific antibodies, along with epitope mapping utilizing mouse neutralizing monoclonal antibodies [259] [274]. Site 1, encompassing amino acids 89 to 100 of VP1, stands as a major immunogenic region for serotype 2 and 3 polioviruses, though it is generally immune recessive in serotype 1 poliovirus [275]. Site 2 is intricate, incorporating residues 220 to 222 of VP1 (site 2a) and residues 169 and 170 on VP2 (site 2b) [274]. Both sites 2a and 2b have been identified in serotype 1 poliovirus, while only site 2b is present in serotype 3 poliovirus. Antigenic site 3 is also multifaceted, encompassing residues 286 to 290 from VP1 (site 3a) as well as residues 58 and 59 and others on VP3 (site 3b) [274]. Both sites 3a and 3b are present in serotype 3 poliovirus, whereas only neutralizing monoclonal antibodies targeting site 3b have been detected in poliovirus serotype 1 [275]. The location of the amino residues within the three-dimensional structure of the virion indicates that the majority of these antigenic sites are highly exposed to the capsid surface [276] (Figure 4.1.1). The antigenic sites themselves are not involved in poliovirus receptor binding, which is in between the 2-fold and 5-fold axis [261], but antibodies binding to these spots may cause steric hindrance, therefore hindering receptor binding and virus entry [277].

A recent structural biology study of poliovirus neutralizing monoclonal antibodies suggests that antibody C3 is capable of bivalently binding to both 160S and 135S particles at the edge of 5-fold mesa (close to previously determined antigenic site 1) and causing residues of the BC loop to move by an estimated 5 Å [278] (Figure 4.1.1). The orientation of the attached Fabs (antibody fragment ab, without fragment c) in their reconstructions indicates that C3 achieves poliovirus neutralization by attaching to two adjacent BC loops, impeding the viral capsid from conformational changes [278]. Another neutralizing monoclonal antibody A12 was found interacting with poliovirus type 1&2 at slightly different angles and poliovirus type 3 with 10 times lower affinity [279]. A12 binds to viral capsid at the bottom of the canyon surrounding the 5-fold axis of symmetry that was previously shown to interact with cellular poliovirus receptor CD155 [17] [279]. These structural studies of poliovirus - monoclonal antibody complexes prove that some antibodies can bind both natural and expanded poliovirus, and the binding pattern of some antibodies can be different between poliovirus serotypes.

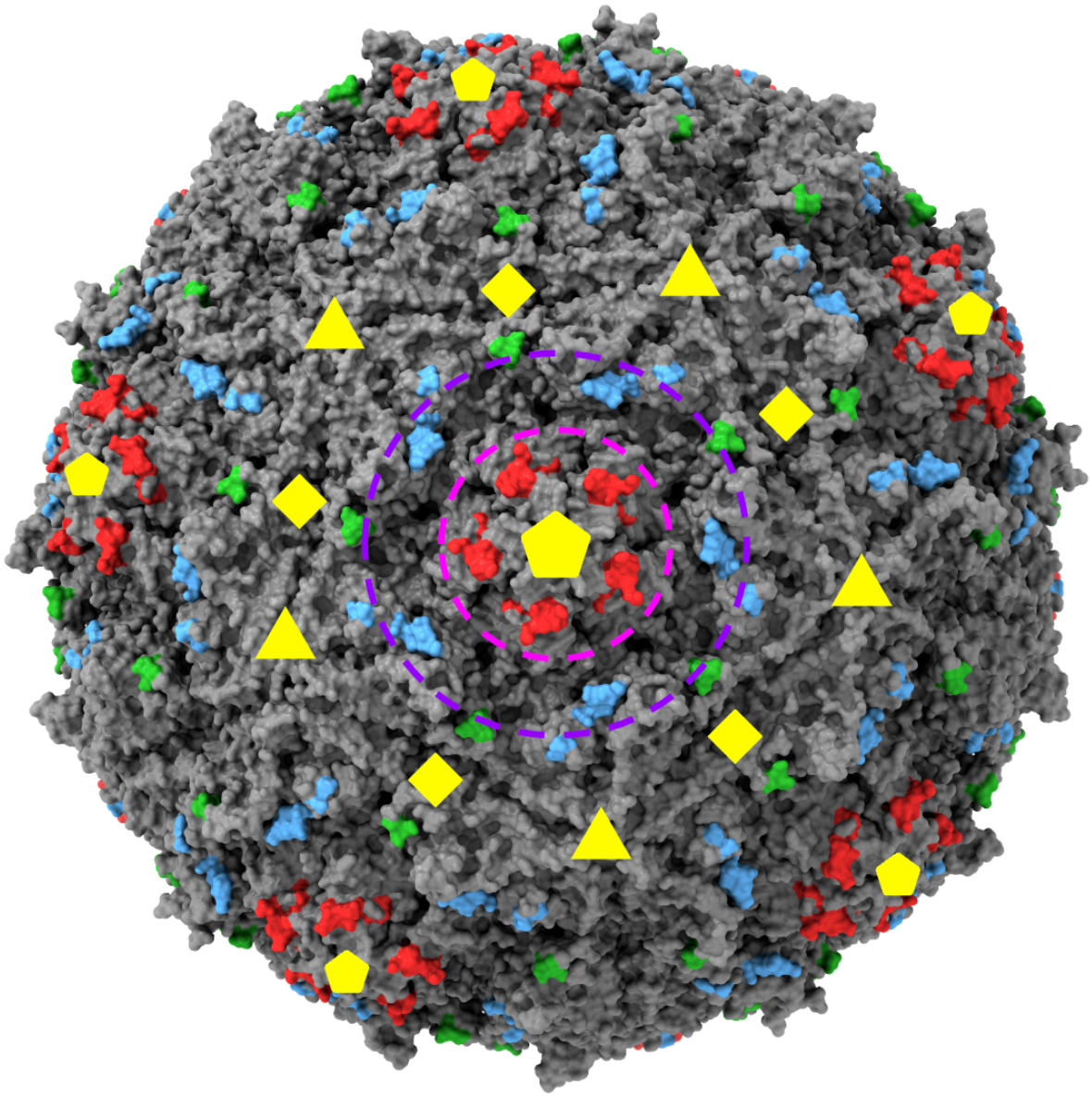


Figure 4.1.1 Prominent structural features of poliovirus. Symmetric centers are marked in yellow shapes. Pentagon means 5-fold axis. Triangle means 3-fold axis. Diamond means 2-fold axis. Southern rim of canyon is marked in purple. Northern rim of canyon is marked in pink. Antigenic Site 1 (red): 89-100aa of VP1, Site 2a (green): 220-222aa of VP1, Site 2b (green): 169-170aa of VP2, Site 3a (blue): 286-290 of VP1, Site 3b (blue): 58-59 of VP3

4.2 Overall structures

VLP + Antibody	PV1 + pAb1		PV1 + pAb2		PV2 +pAb1	PV3 +pAb1	PV3 +pAb2	PV2 alone
Status	natural	expanded	natural	expanded	natural	natural	natural	natural
Quantity Percentage	76,867 77%	22,952 23%	213,251 56%	170,263 44%	313,748	38,886	136,920	75,420
Absent pantamer	34,129 3.7%	/	89,566 3.5%	/	141,467 3.75%	15,484 3.3%	59,493 3.6%	30,032 3.3%

Table 4.2.1 overall data collected and analysed in this chapter

pAb1: polyclonal antibodies purchased from NIBSC (Anti Poliovirus serum types 1,2 and 3 (3rd International Standard) 82/585)

pAb2: polyclonal antibodies collected from Prof. David Rowlands from University of Leeds.

Absent pentamer percentage = absent pentamer quantity / total pentamer quantity.

In total, six cryo-EM datasets are collected and analysed in this chapter (table 4.2.1), including poliovirus type1 (PV1) VLP mixed with two types of polyclonal antibodies (pAb1 & pAb2, derived from different source, but both from human), poliovirus type2 VLP (PV2) with pAb1, poliovirus type3 VLP (PV3) mixing with pAb1 & pAb2, and negative control PV2 alone (Figure 4.2.1). Among these, PV1 VLPs are found in two distinct conformations – natural and expanded, confirmed by fitting the molecular model of 160S and 135S PV1 (Figure 4.2.2). This is seen normally in batches of PV1 VLP and the ratio of the two particles can vary markedly between different batches, which makes it hard to judge whether pAb-binding leads to any conformation changes. In contrast nearly all of the PV2 and PV3 VLPs are in natural state, and the number of expanded particles is negligible.

Upon initial inspection of the outer surfaces of the six icosahedral-averaged reconstructions, the PV1-pAb1 expanded particles stand out, as they clearly attracted Fabs consistently attaching to the 2-fold axis (Figure 4.2.1). Although

less obvious visible traces of potential signal from Fab attachment can be found after careful inspection in all other pAB containing groups, as their viral surfaces are not smooth in comparison to the PV2 control (Figure 4.2.1).

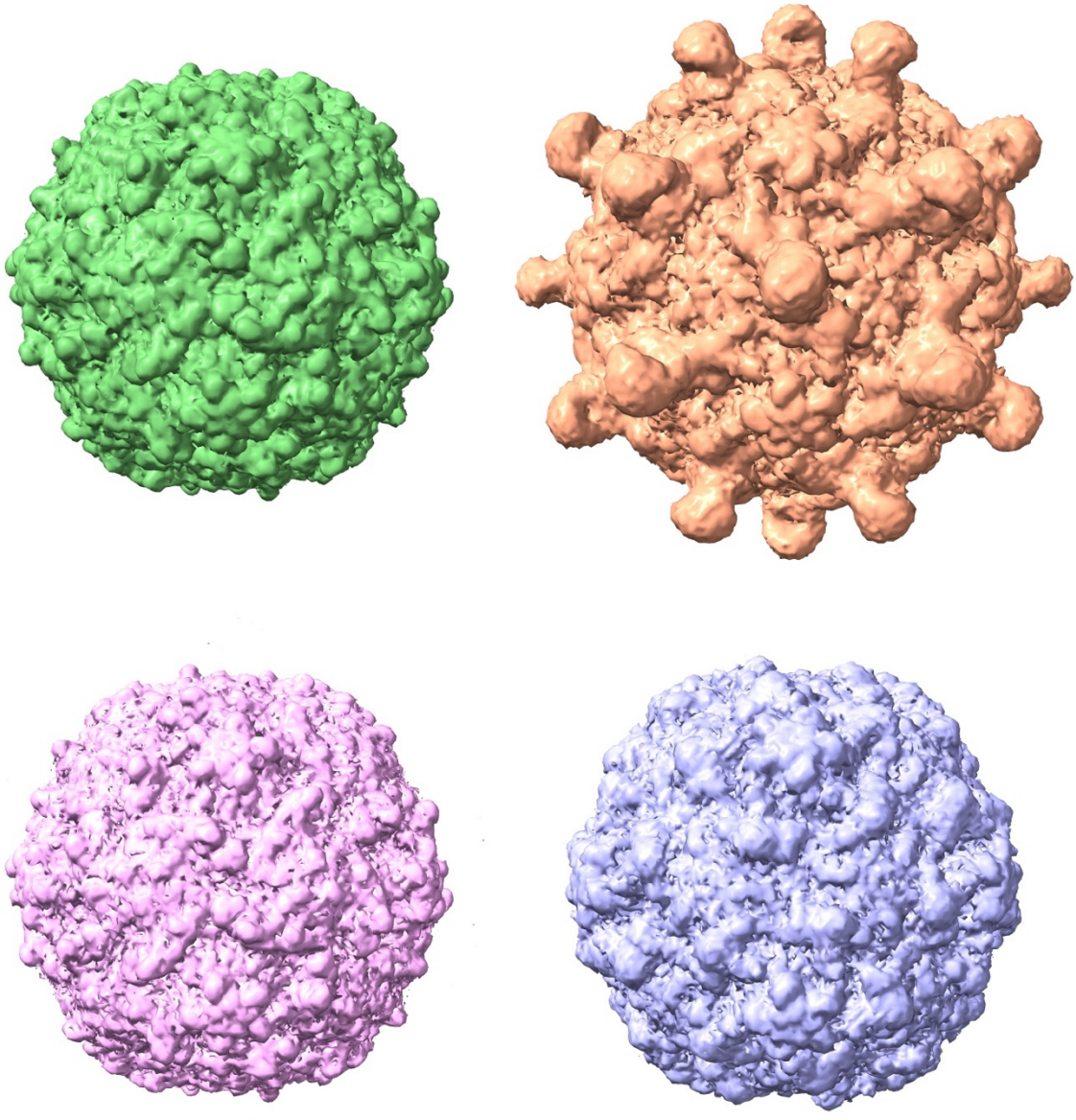


Figure 4.2.1a Overall structural result of 6 datasets. green: PV1-pAb1 natural particles, orange: PV1-pAb1 expanded particles**,** pink: PV1-pAb2 natural particles, light purple: PV1-pAb2 expanded particles**,** These four structures are heterogeneous refinement results of bin4 data. Bin4 means Fourier crop to ¼ of the original box size (pixel).

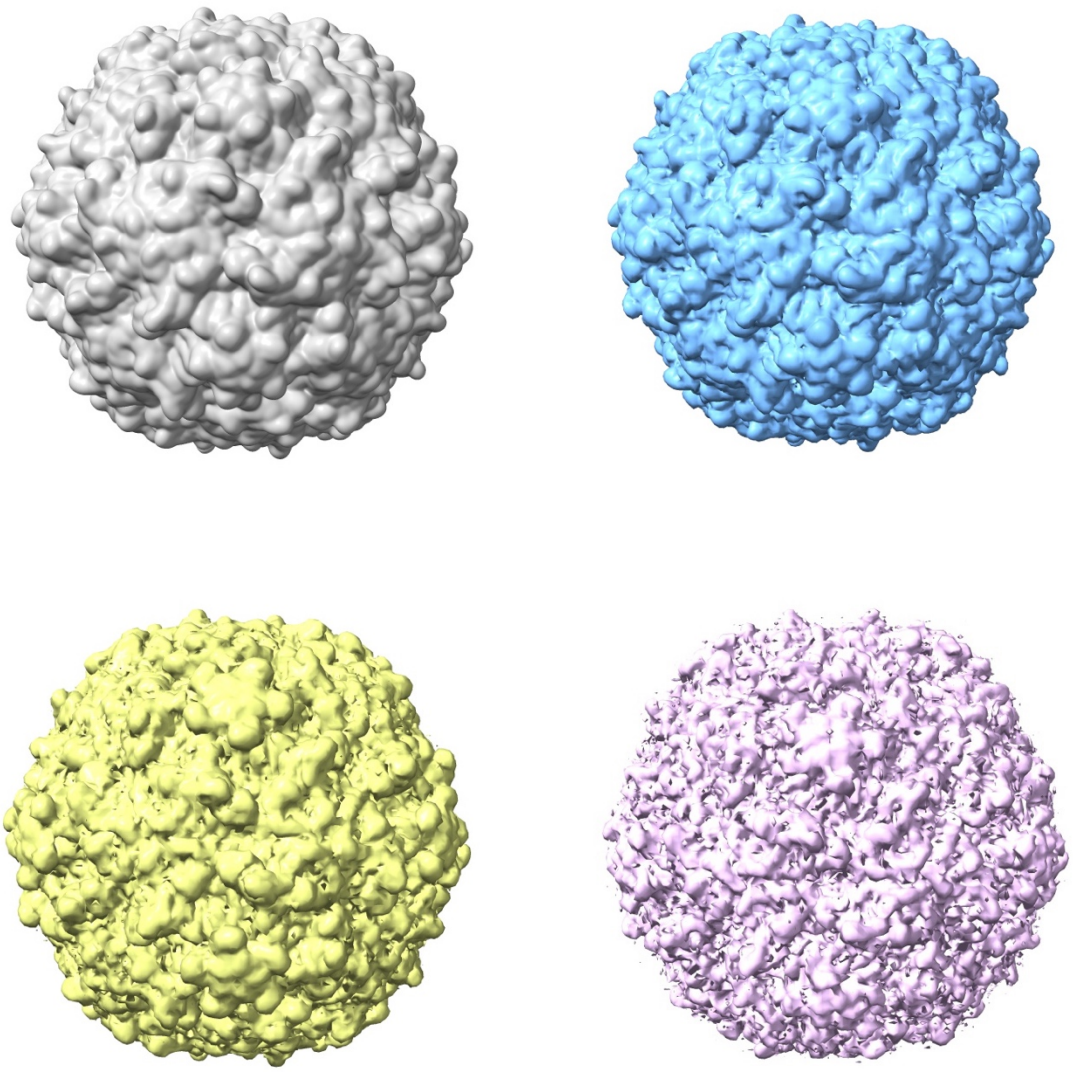


Figure 4.2.1b Overall structural result of 6 datasets. grey: PV2 alone as control, blue: PV2-pAB1 natural particles, yellow: PV3-pAB1 natural particles, light pink: PV3-pAB2 natural particles**.** These four structures are the homogeneous refinement results of bin4 data. Bin4 means Fourier crop to ¼ of the original box size (pixel).

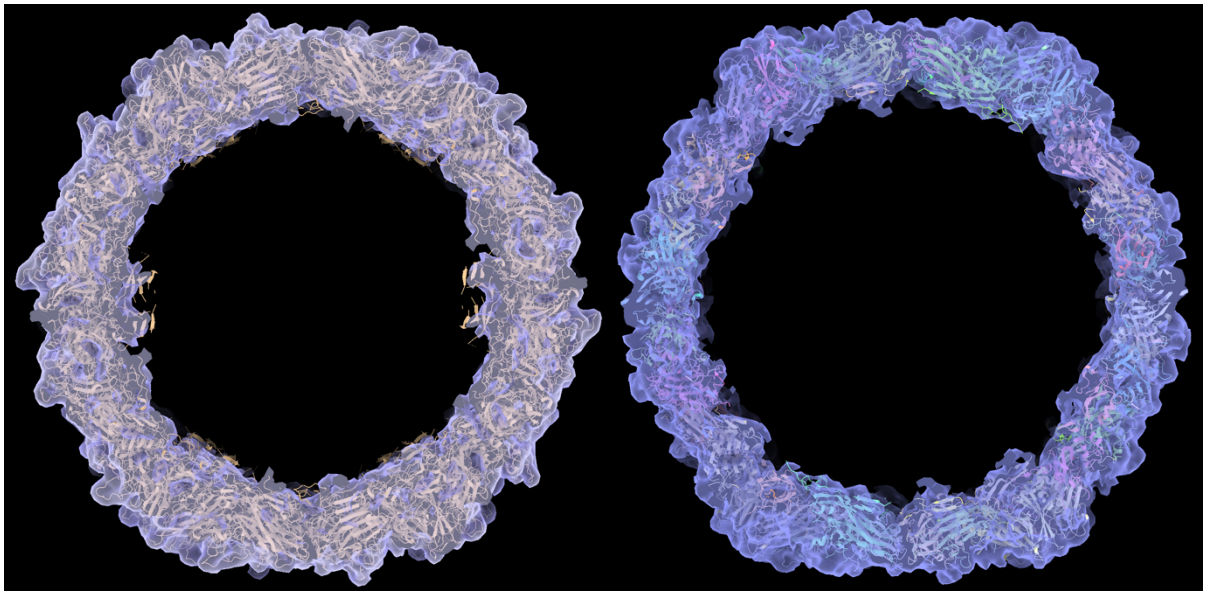


Figure 4.2.2 Central sections of natural and expanded PV1. Cryo-EM density of natural VLP (at left in purple) and expanded VLPs (at right in purple). 160S (yellow PDB:1PO2) and 135S (rainbow PDB:6P9O) PV1 particles are fitted respectively.

Enterovirus viral capsid consist of 60 identical protomers (described in section 1.1.3), meaning each antibody binding epitope has 60 identical copies per capsid. In this section, homogeneous refinement is performed on the level of whole viral capsids, and icosahedral symmetry (I symmetry) is applied to the refinement program, assuming that all VLPs are icosahedral-symmetrized. Since there are potentially countless numbers of polyclonal Fabs attaching to the capsid, I symmetry must be applied at the capsid level. The disadvantage of this is reducing the signal of different Fabs significantly due to their inconsistency. To overcome this, a Symmetry expansion + Re-center, Re-extraction, Reconstruction method (SyRe method described in Chapter 2 section 2.6.3) is applied focusing on either protomer level (section 4.3, 4.4, 4.5) or pentamer level (section 4.6, 4.7). I will start by detailing the analysis of the particles showing the most prominent decoration, the PV1-pAb1 expanded particles.

4.3 2-fold pAb1 attaching to expanded PV1

As shown in Figure 4.2.1a, PV1 expanded particles have already reconstructed a consistent Fab attachment to the 2-fold axis, but SyRe protocol (Figure 4.3.1-4.3.4) still managed to sort out one major class (Figure 4.3.3) and several distinguishable minor classes of Fabs attaching to PV1 in slightly different manners (Figure 4.3.4).

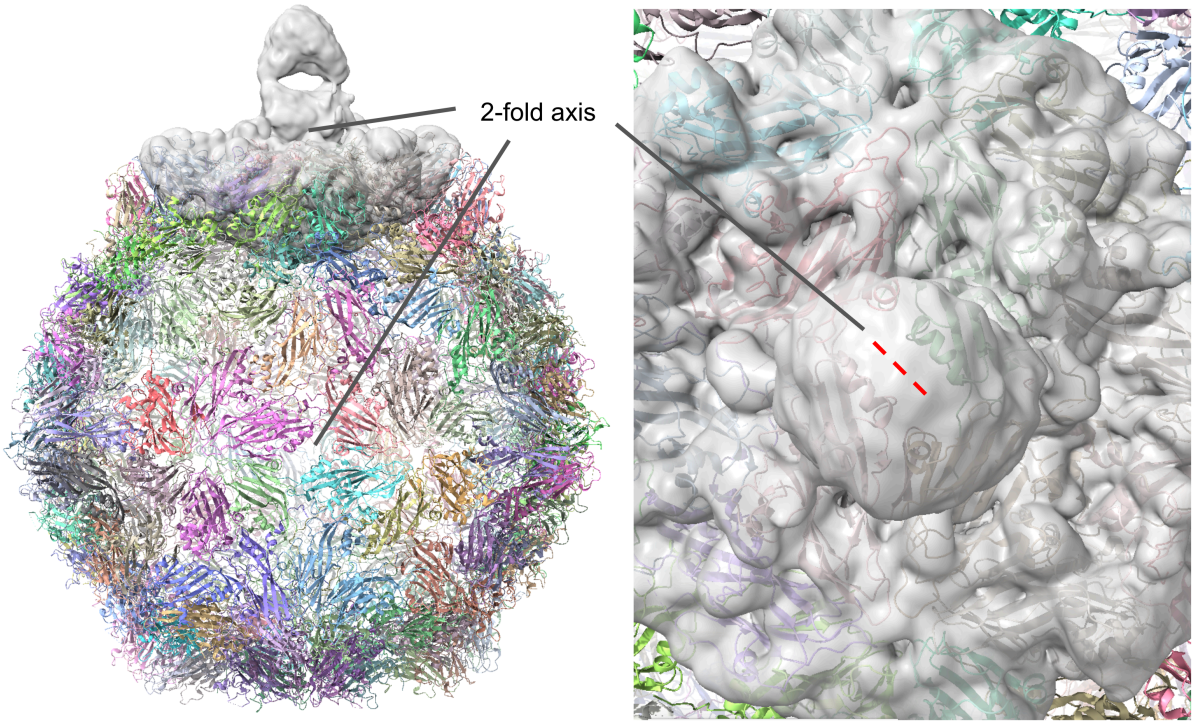


Figure 4.3.1 2-fold Fab binding pattern. Left: front view. Right: top view. Poliovirus VLP coordinates coloured in rainbow to distinguish each viral protein (VP). Density map coloured in grey is the re-extraction of Fab using a smaller box re-centered at the Fab-capsid interface.

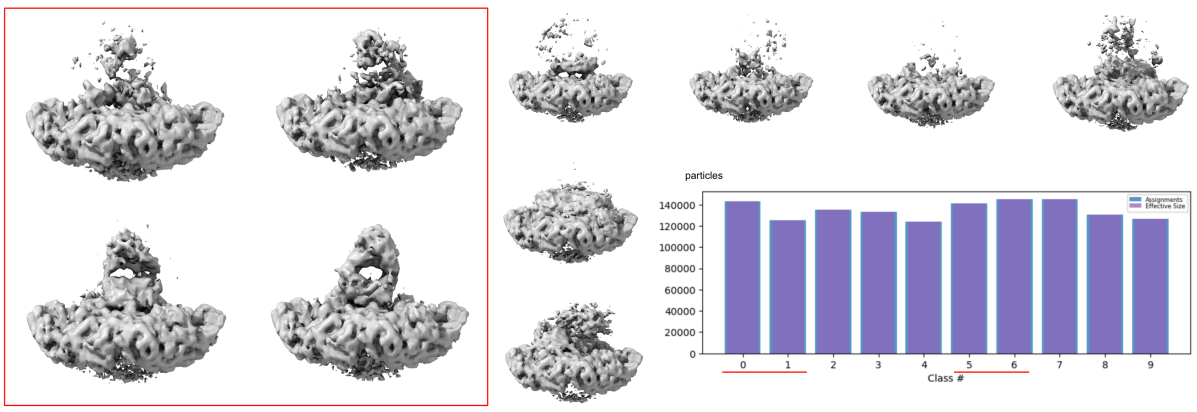
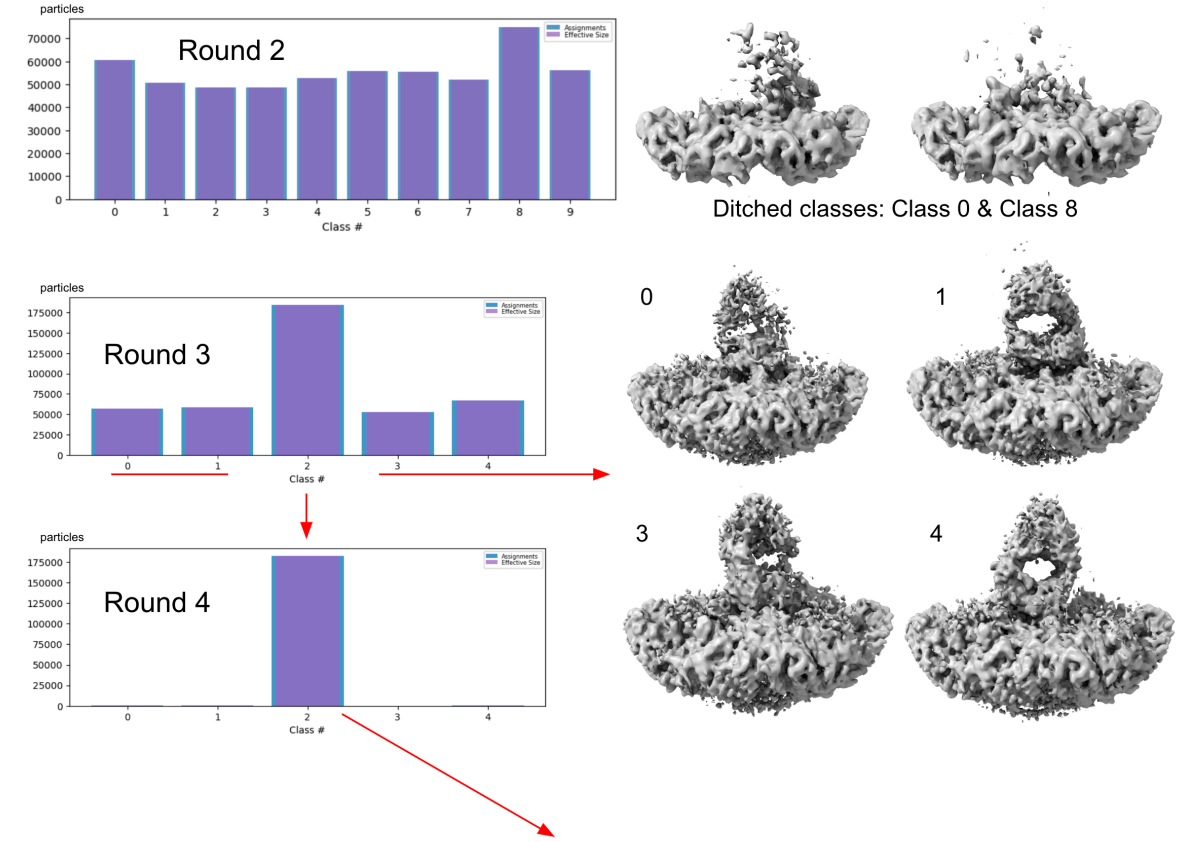


Figure 4.3.2 2-fold Fab classification round 1. Density map coloured in grey is the classification outcome. Red line indicates the promising classes selected for next round.



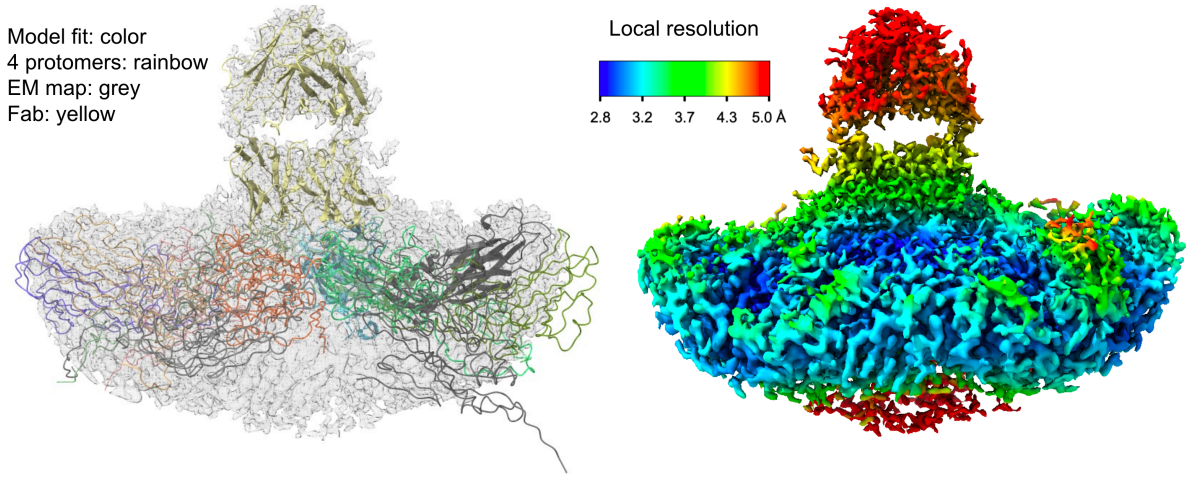


Figure 4.3.3 3D classification round 2-4 and the outstanding results. Round 2 showed two bad classes without apparent Fab looking density. Combining the other 8 similarly good classes from round 2 and run round 3 in 5 classes, one major class (class 2) stands out and can no longer be separated by round 4. Fitted Fab model comes from PDB: 1fpt, and protomer model from PDB: 6p9o.

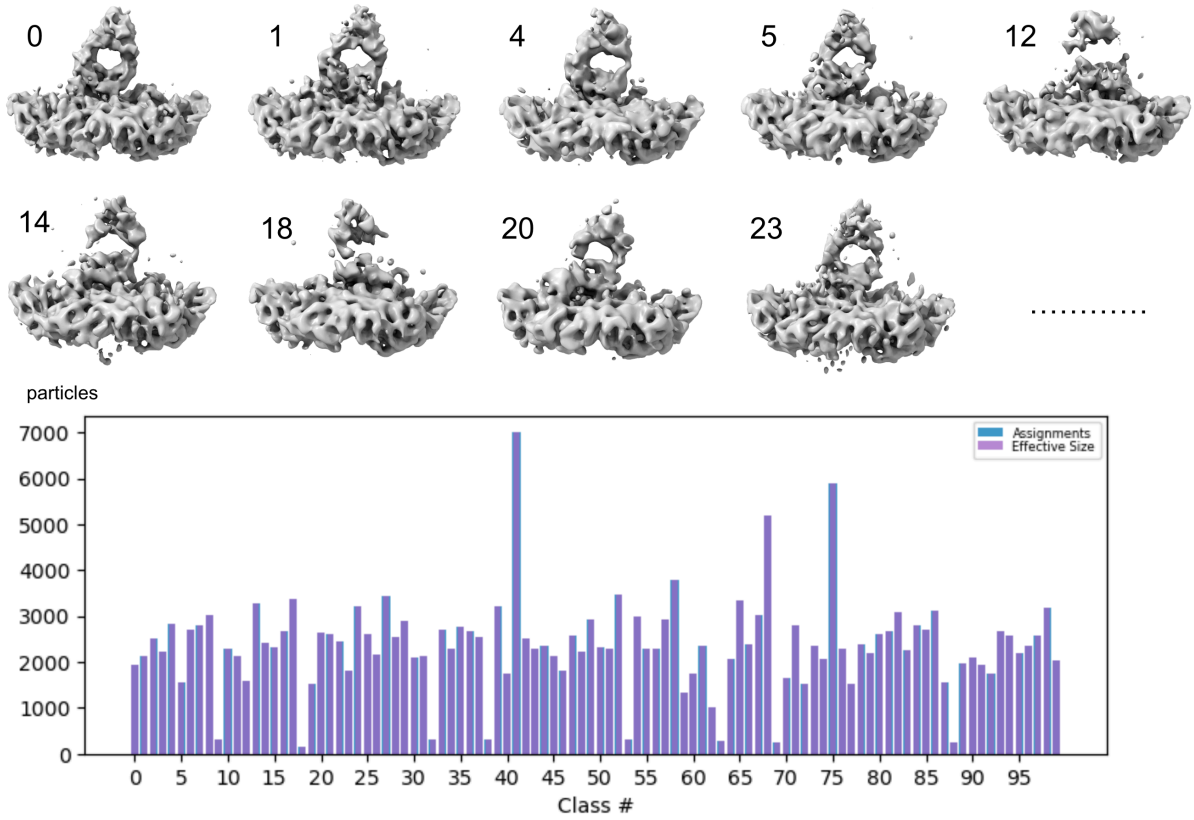


Figure 4.3.4 3D classification round 4+. Input: Classes 0,1,3,4 of round 3. Output: several distinguishable minor classes of Fabs attaching to the 2-fold axis in slightly different manners

4.4 3-fold pAb1 attaching to expanded PV1

To further identify other potential Fab attachment, the SyRe method was repeated focusing on the center of the protomer outer-surface, and also at points corresponding to the middle point of 2-fold, 3-fold and 5-fold. Since the 2-fold Fab signal and VLP protomer signal was very strong and consistent, a focused mask was applied to 3D classification jobs to exclude those signals (Figure 4.4.2 second line, mask showed in transparent green).

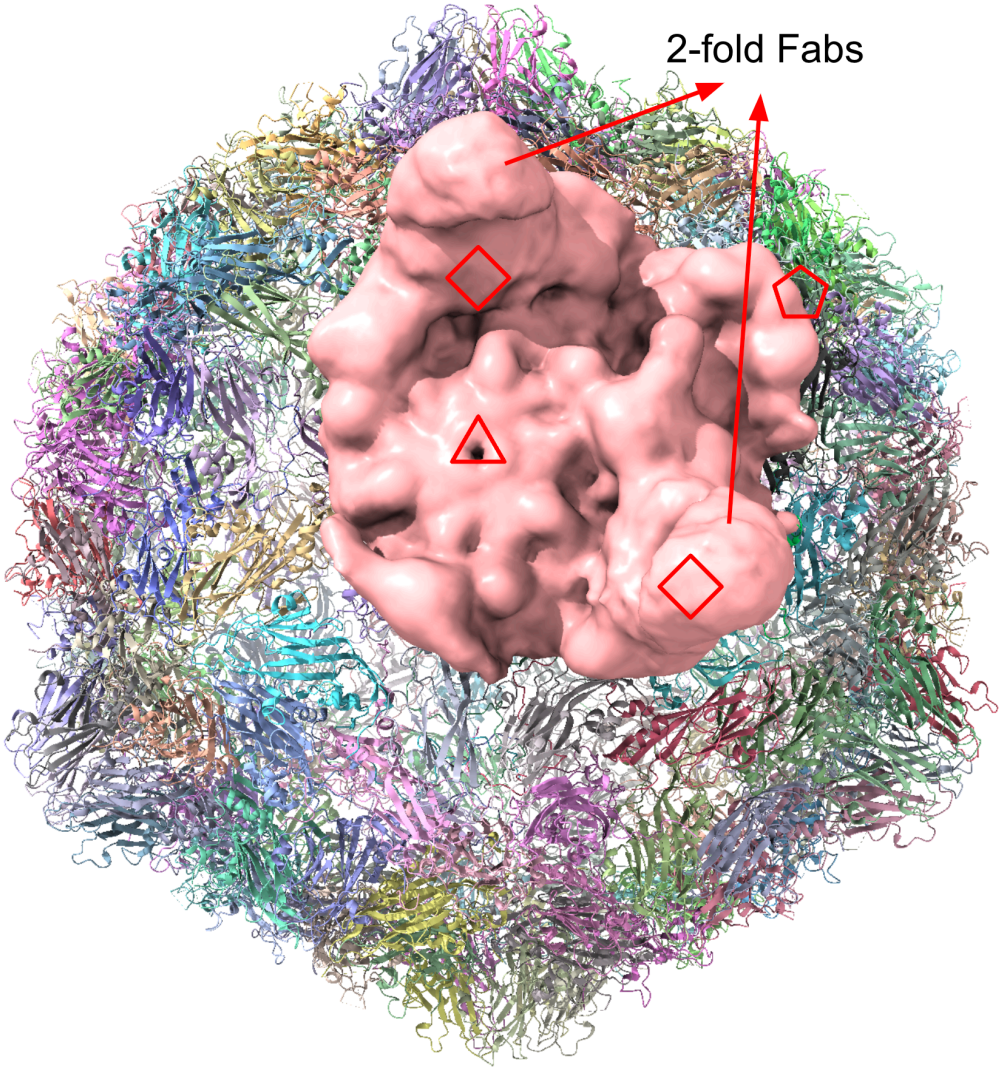


Figure 4.4.1 re-center, re-extraction and re-construction. 2/3/5-fold symmetric center is marked in red shapes. Post-SyRe structure is coloured in pink. Beneath that is viral capsid coloured in rainbow. Two 2-fold Fabs are included in the re-extraction box as shown on top and right side.

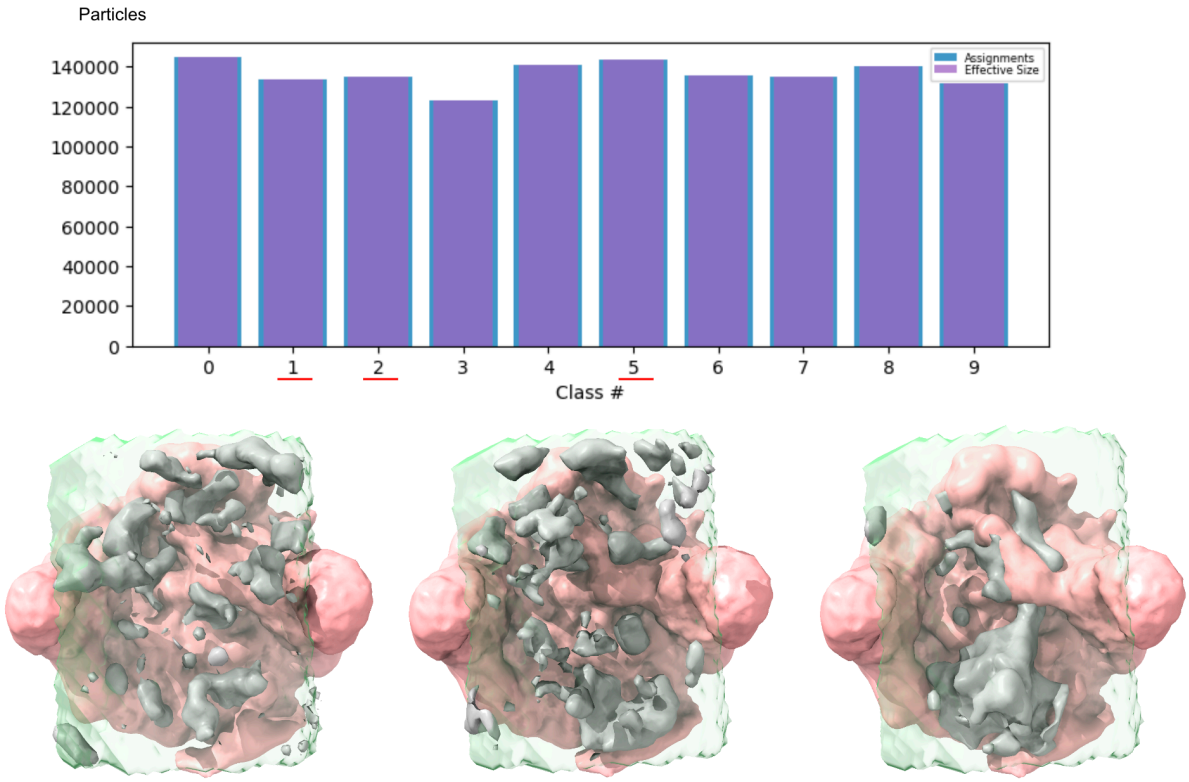


Figure 4.4.2 Round 1 of 3D classification. Input particles are equally distributed into 10 classes. Within the mask (transparent green), cryo-EM density (grey) seems randomly distributed in all the classes. Classes 1, 2, 5 were chosen for further classification as they contain Fab-like signal around the 3-fold axis.

Two rounds of 3D classification excluded 97% of particles, and the remaining 3% of particles formed a relatively clean Fab structure (Figure 4.4.3). Unlike Figure 4.3.4 in the previous section, this 'good' class of 3-fold Fab cannot be further separated, likely because there too many minor classes of Fabs sitting close to 3-fold to be cleanly separated (see section 4.5).

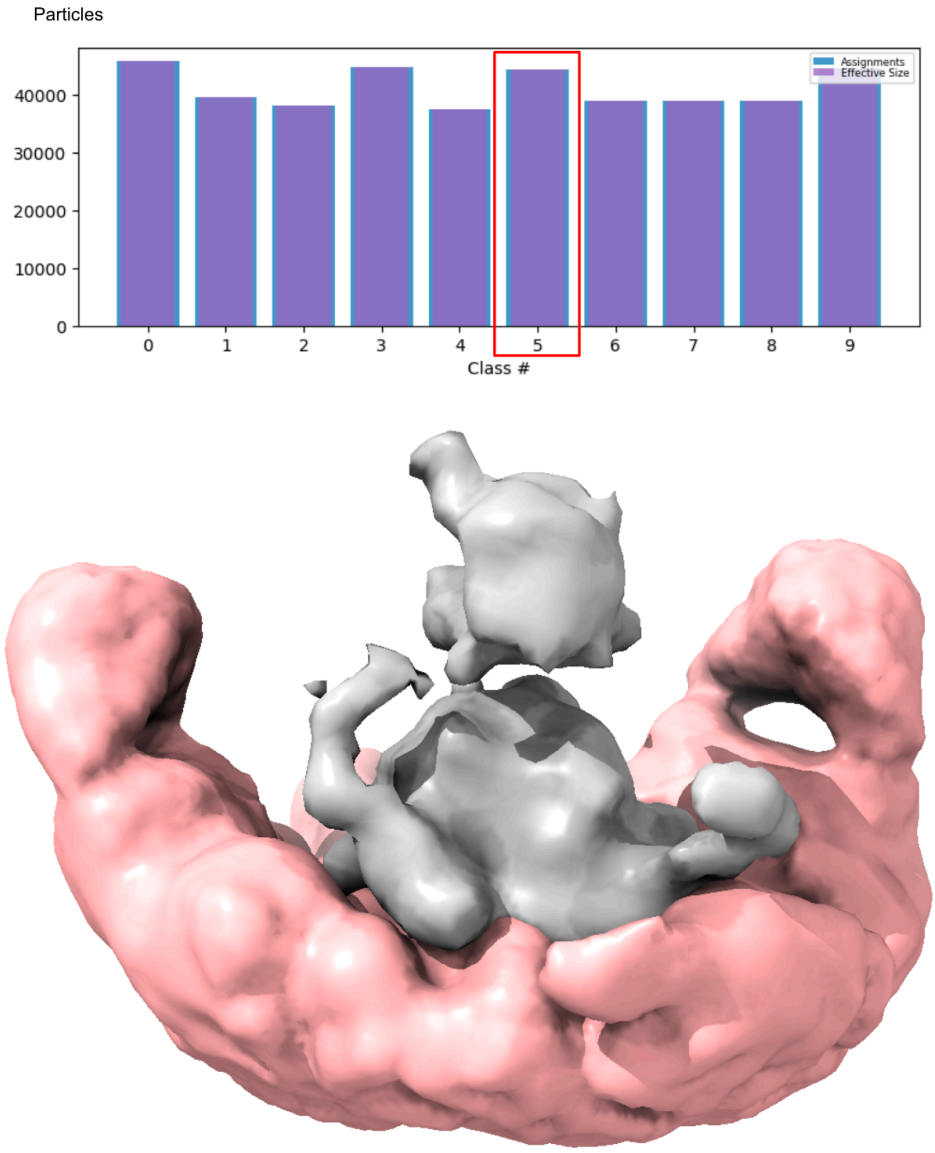


Figure 4.4.3 Round 2 of 3D classification

4.5 Other pAb1 attaching to expanded PV1

Now that 2-fold Fabs and 3-fold Fabs are identified, the SyRe procedure was focussed slightly towards the 5-fold mesa to avoid the 3-fold Fabs (Figure 4.5.1 left, pink volume) and a mask was applied to 3D classification jobs to exclude 2-fold Fabs (Figure 4.5.1 right blue volume). Similar to the detection of 3-fold Fabs, the outcome of the first two rounds of classification was extremely messy (Figure 4.5.2). Outputs of round 2 were manually separated into two groups, based on whether the results had strong signal at the **southern rim** of the canyon (Figure 4.5.2 mask 1 in blue) or had strong signal at the **northern rim** of the canyon (Figure 4.5.2 mask 2 in yellow). The first group went through classification round 3-1 (Figure 4.5.3) & 4-1 (Figure 4.5.4) and purified into 9 Fab classes. The second group went through classification round 3-2 (Figure 4.5.5) & 4-2 (Figure 4.5.6) and purified into 12 Fab classes. The process of selecting proper classes for the next round is purely subjective. Good classes/results normally meant that there were large and obvious density features within the map that could be part of a Fab. Based on my experience, the minimum particle number for 3D classification is 1000 particles per class, otherwise differences will be ignored due to low resolution. Even though those 9 + 12 classes may contain different Fabs per class, they can no longer be separated using the current computational procedures.

The final outcomes of 4 such rounds classification are several Fab-like densities (Figure 4.5.4 & 4.5.6), but how Fab-like are they? By low-pass filtering those Fabs to the same resolution and calculating the cross-correlation coefficient between a Fab model and the Fab density, a quantitative method can be established to determine the similarity of Fab and density map. However, it would only provide a possible value as the Fab sequence is unknown and how many classes of Fabs contributing to one of the resultant densities is unknown. So such a quantitative method is not applied here.

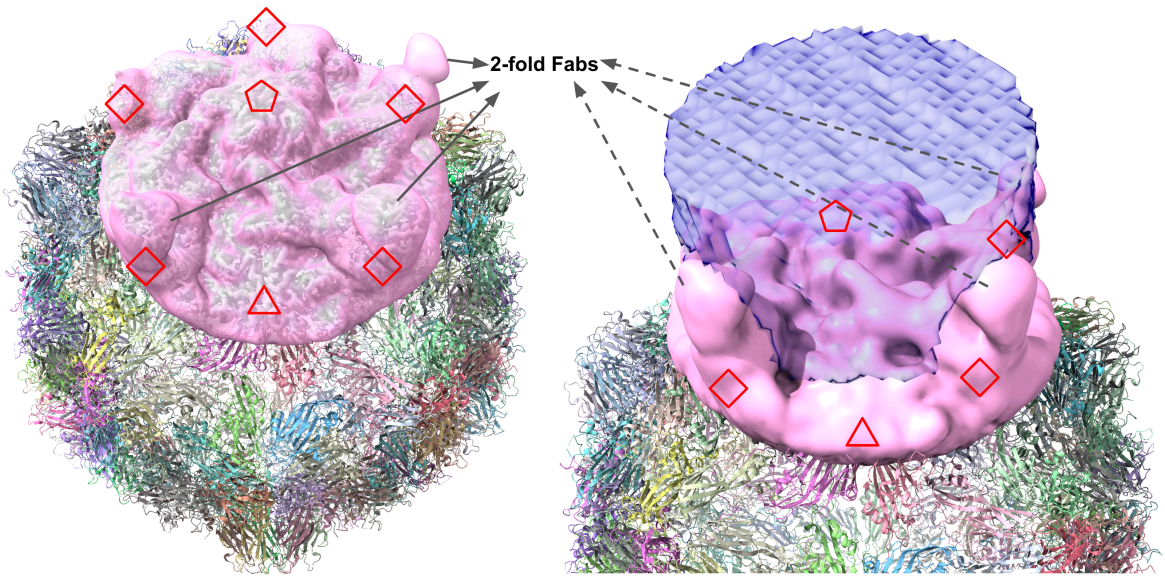


Figure 4.5.1 Searching for other Fabs by SyRe. The 2/3/5-fold symmetric center is marked in red shapes. Post-SyRe structure is coloured in pink. Beneath that is the viral capsid coloured in rainbow. Three 2-fold Fabs are included in the re-extraction box as shown on the top and right side.

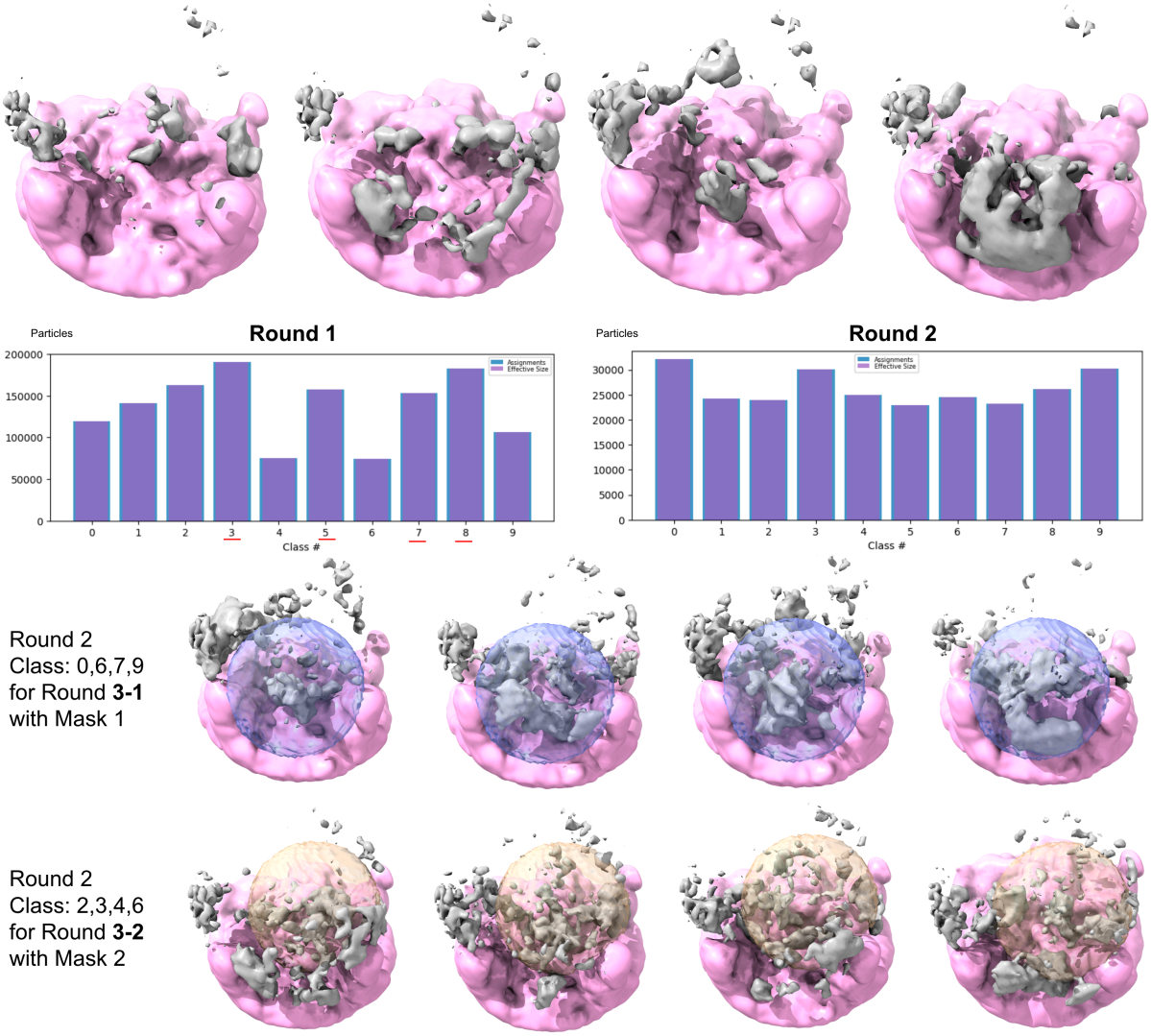


Figure 4.5.2 Round 1 & 2 of 3D classification for other potential Fab attachment. First row: output of round 1, class 3,5,7,8 showed relatively strong signal within the mask. Second row: particle distribution of round 1&2. Third row: mask 1 focusing on the southern rim of canyon. Fourth row: mask 2 focusing on the northern rim of canyon.

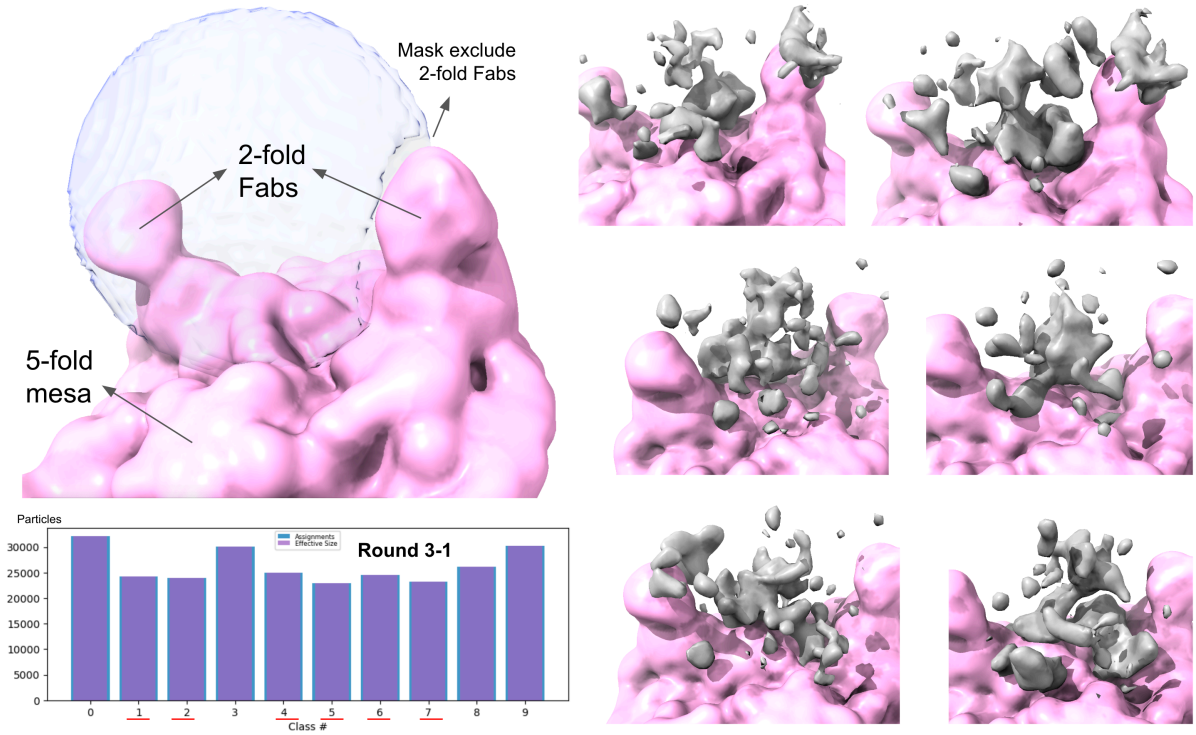


Figure 4.5.3 Round 3-1 of 3D classification (southern rim of canyon). Top left: side view of SyRe structure and mask position. Bottom left: particle distribution. Right: demonstration of good results - class 1,2,4,5,6,7. Good results were purely subjective since although cross-correlation against Fab electron density could provide a quantitative metric it is possible that several Fabs contribute to the density features which makes this less reliable as is now discussed.

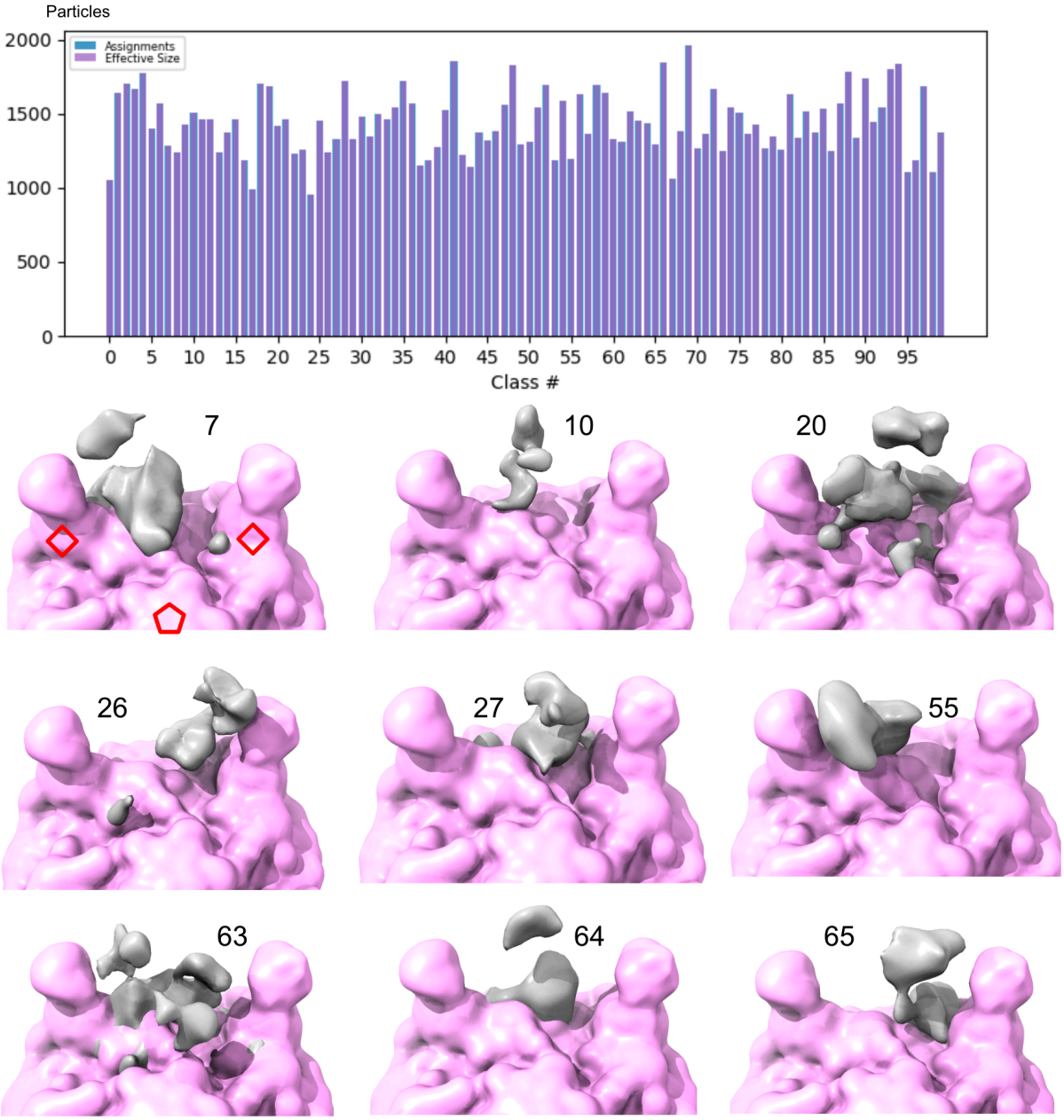


Figure 4.5.4 Round 4-1 of 3D classification (southern rim of canyon). Top row: particle distribution. Bottom rows: class 7,10,20,26,27,55,63,64,65 showed potential Fabs in the maps.

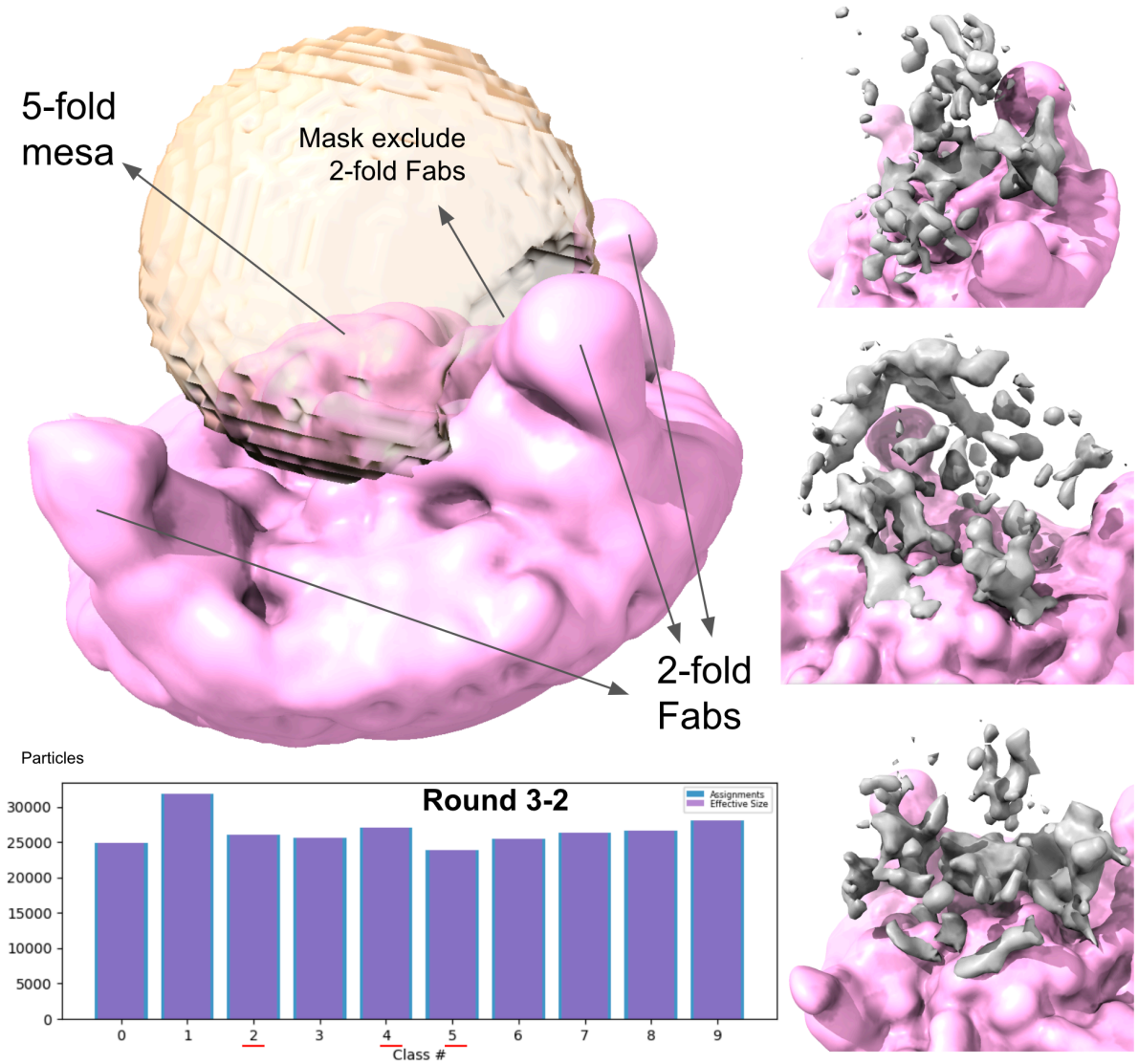


Figure 4.5.5 Round 3-2 of 3D classification (northern rim of canyon). Top left: side view of SyRe structure and mask position. Bottom left: particle distribution. Right: demonstration of good results - class 2,4,5. Good results were purely subjective since although cross-correlation against Fab electron density could provide a quantitative metric it is possible that several Fabs contribute to the density features which makes this less reliable as is now discussed.

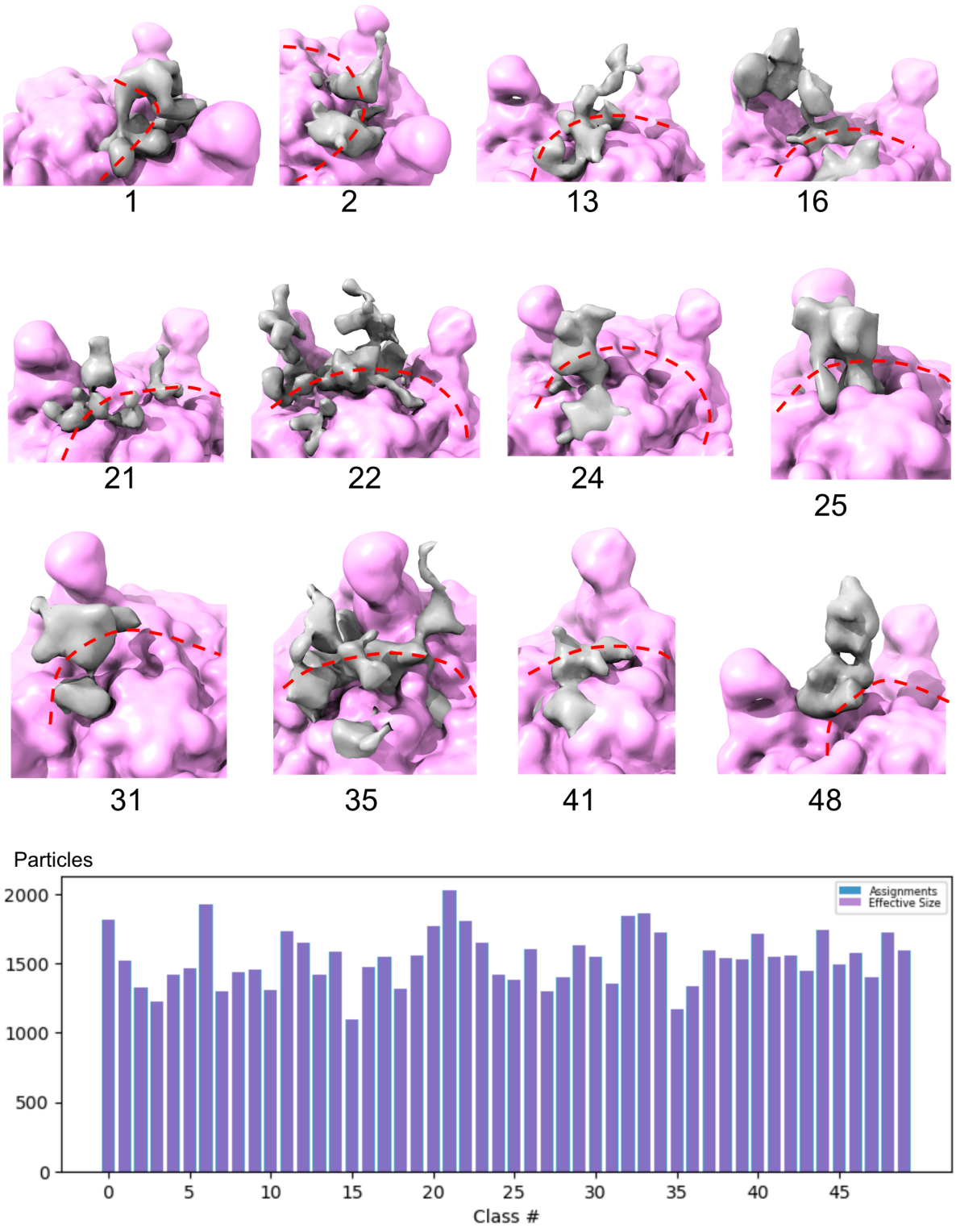


Figure 4.5.6 Round 4-2 of 3D classification (northern rim of canyon). Top rows: Potential Fab-binding classes, demonstrated in proper angle for best Fab-view. Red circle indicates the approximate location of the southern rim of the canyon.

4.6 New epitopes provided by an absent pentamer

It was not expected to find absent pentamers in poliovirus VLPs. However, the VLPs used for this study (except PV1 expanded particles) have 3% - 4% of the pentamers missing (each viral capsid is consisted of 12 pentamers). This result is not observed in capsid-scale heterogeneous refinement, but is revealed by pentamer-scale 3D classification using the SyRe procedure and was uncovered in an effort to explain the deviations of the icosahedral reconstructions from the expected 'smooth' virus-like structure.

At first, the protomer-scale SyRe method was applied to all the datasets to look for outcomes similar to that described for the PV1 expanded particles (section 4.3 – 4.5). Not a single consistent class of Fab was observed, but the capsid surface was not as smooth as the negative-control, indicating that Fabs were attached to the surface but could not be classified with the protomer-scale extraction box. There are two plausible explanations. One is that the polyclonal Fabs in those datasets were extremely diversified and potentially far less than 1000 particles per class. Alternatively, adequate consistency for 3D classification could not be found with that level of diversity.

The other explanation is that the viral capsid was not in the natural antigenic state, however the particles were not expanded as checked in homogeneous refinement. To further dissect the issue a middle-sized extraction box was chosen for SyRe protocol, and a middle scale (pentamer-scale) classification was performed. This led to the discovery of pentamers from some of the native class particles. This is itself was surprising. What was even more surprising was that Fabs were found attaching strongly to the inside of the pentamer-pentamer interface (Figure 4.6.1-4.6.3). These Fabs overlapped the missing pentamers, but also protruded somewhat, presumably explaining the deviations from a ‘smooth’ capsid. Although Fab was found at the same position as the absent pentamer, there is no evidence that, for these VLPs, pentamer-loss is caused by Fab attachment, because a broadly similar ratio of absent pentamers was found in the negative control (PV2 without pAB). However, this is a critical question and warrants careful investigation, since pentamer loss would provide a mechanism by which such antibodies could be neutralising.

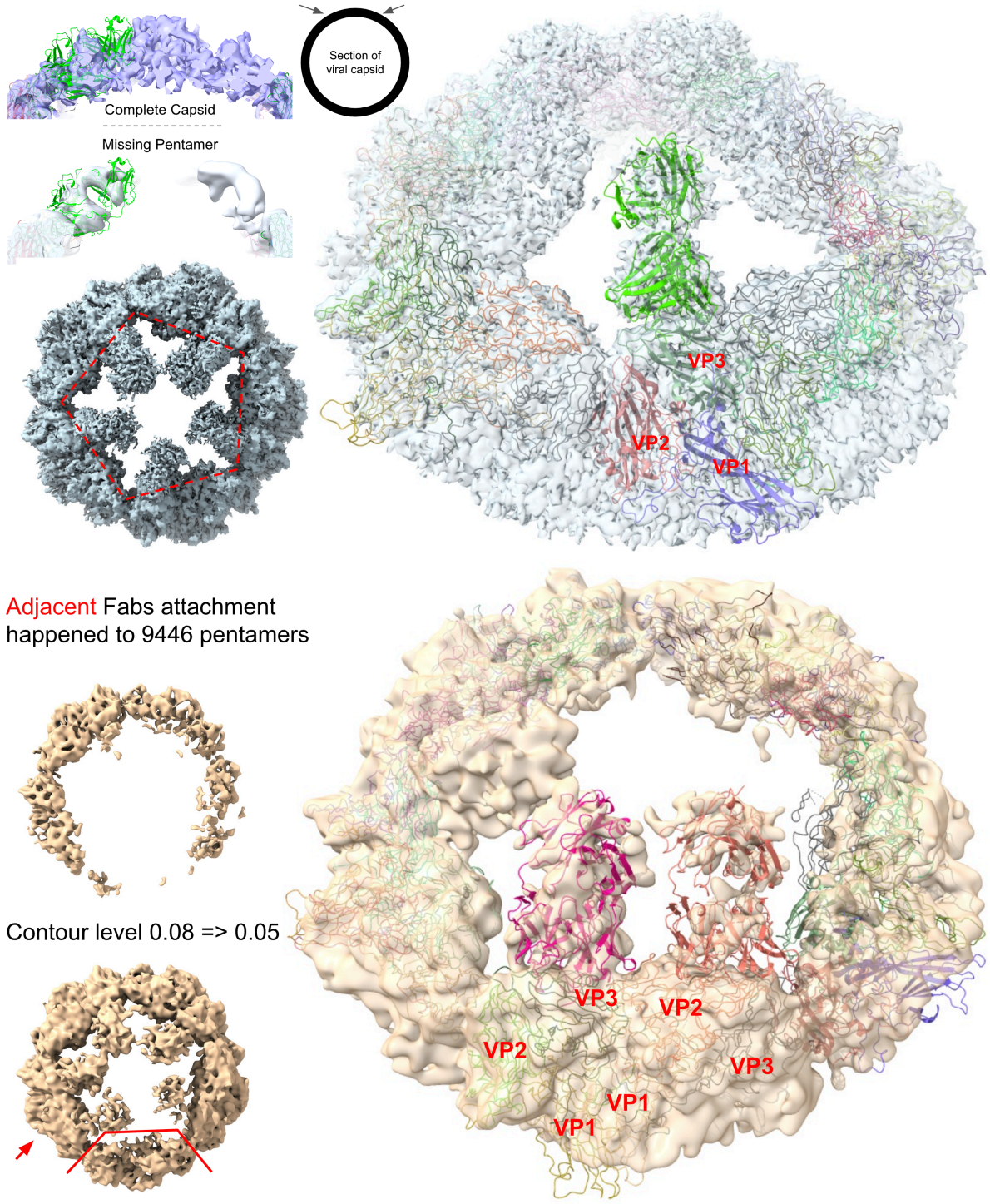


Figure 4.6.1 PV3-pAb2

Left column 1st - 2nd row: upper part of viral capsid in section view. Purple density is where the absent pentamer used to be. Grey density represents Fabs replacing one pentamer. Green model is a fitted Fab coordinates (PDB:1ftp) indicating that if not missing, the pentamer would completely clash with Fab. Left column 3rd row and right column 1st row: top and 45˚ view. Left column 4th – 5th row: in high contour level, two adjacent absent-pentamers can be seen (red line), and in low contour level, two Fabs can be found attaching to the same side of the pentamer (red arrow). Right column 2nd row: 45˚ view, VP1-3 are marked correspondingly. Right column: PV3 model (PDB:8ayy) are fitted into pentamer density, coloured in rainbow. Models of Fab (PDB:1ftp) are shown in green, pink and orange.

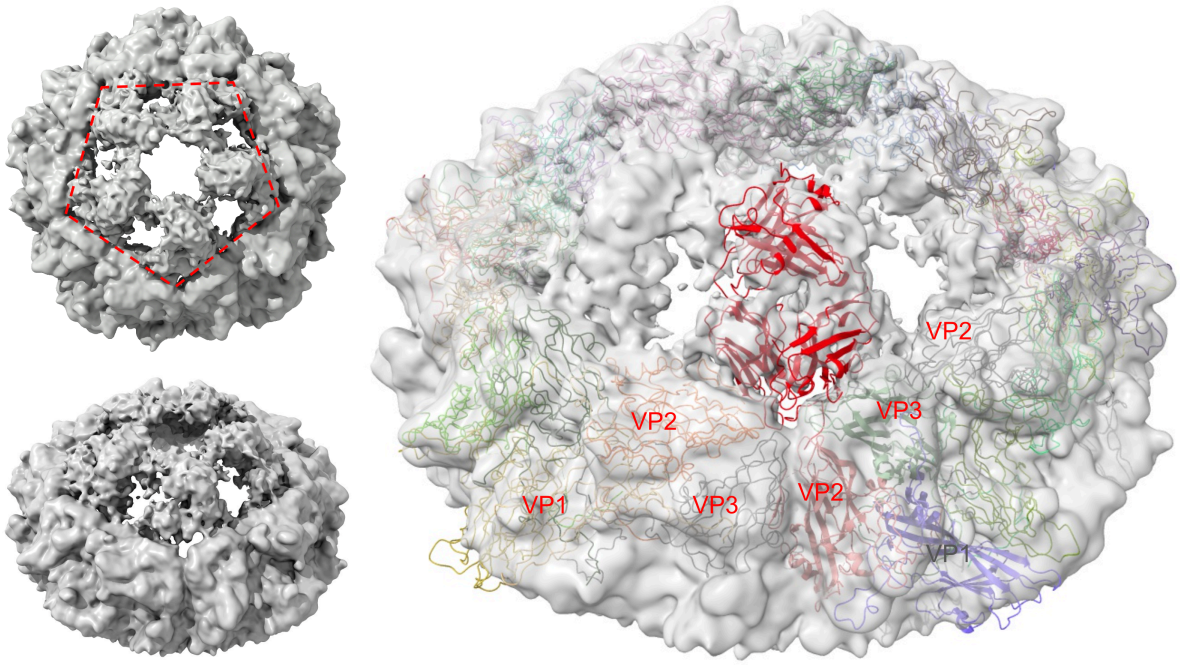


Figure 4.6.2 PV3-pAb1. Top view and 45˚ view.
Fitted Fab model is shown in red (PDB:1ftp), protomer model in rainbow (PDB:8ayy)

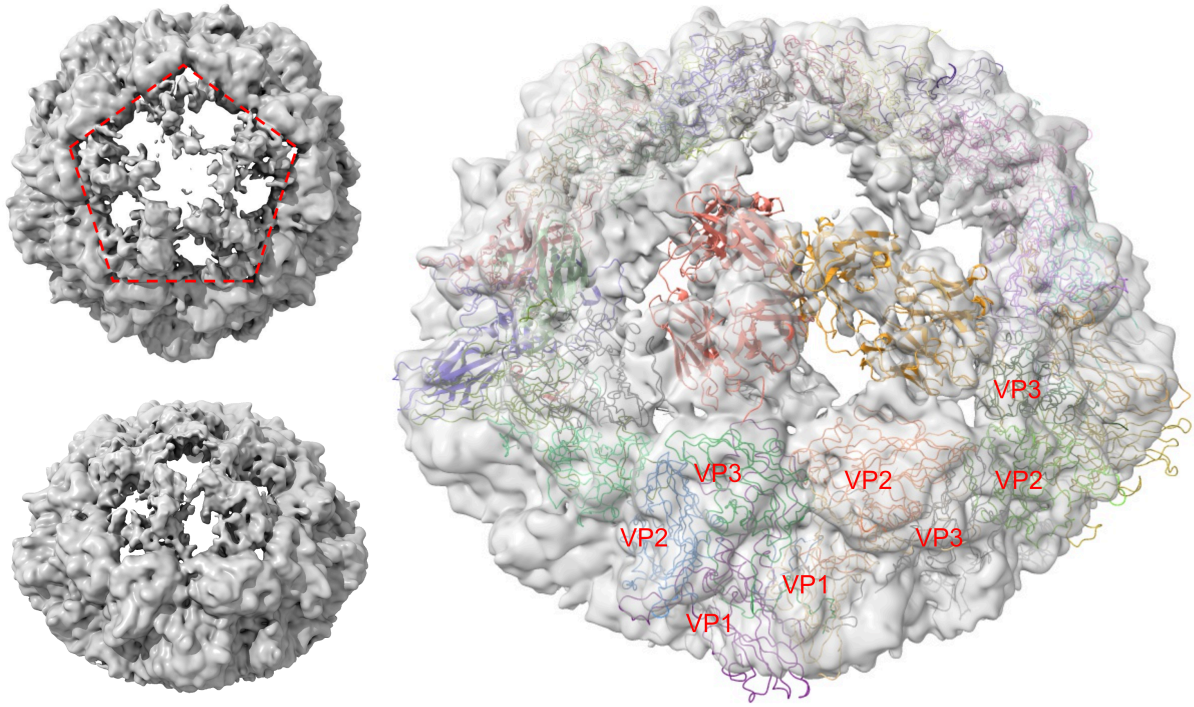


Figure 4.6.3 PV2-pAb1. Top view and 45˚ view.
Fitted Fab model is shown in red (PDB:1ftp), protomer model in rainbow (PDB:1eah)

4.7 Semi-attached pentamer

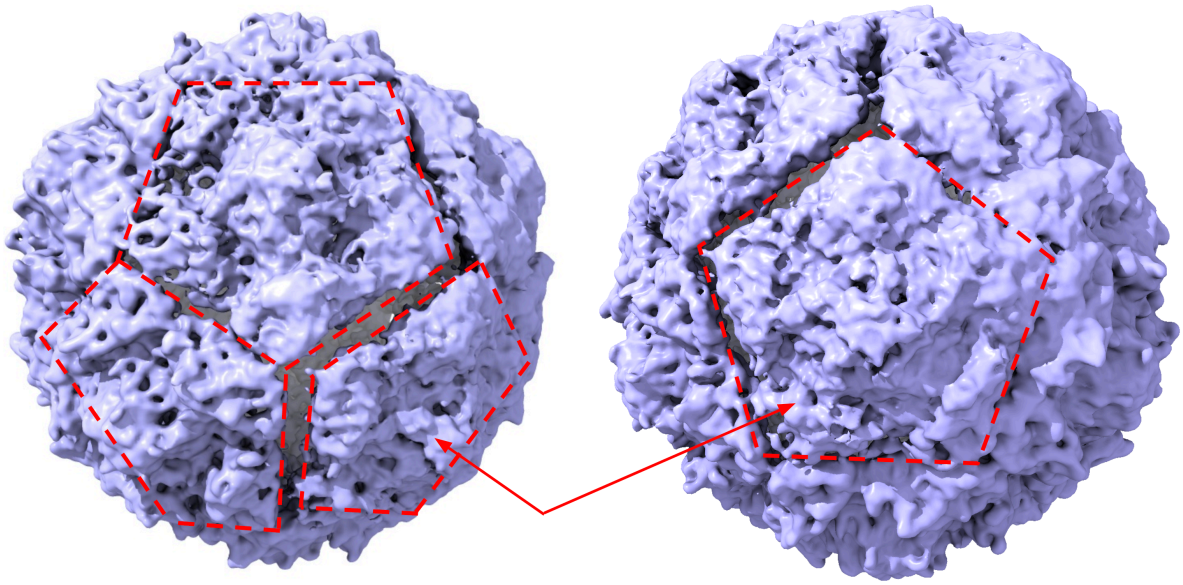


Figure 4.7.1 viral capsid with semi-attached pentamer (red line marks the pentamer edge)

In the process of pentamer scale 3D classification, a few thousand particles are found in one class showing a 'semi-attached' pentamer (Figure 4.7.1). Apart from this semi-attached pentamer, the rest of the viral capsid remained intact and showed no difference to natural particles. This may be an intermediate status of poliovirus assembly or disassembly, and it was found only in the PV3-pAb2 dataset. Since 'breathing' of enteroviruses is well documented it is plausible that this structure represents the first visualisation of a virus caught 'mid-breath' – the openings in the capsid could allow the transient exposure of normally internal proteins which is the hallmark of enterovirus breathing [280]. Finally, I see no direct connection between this semi-attached pentamer and pAb2 interaction since no Fab is detected in the structure and pentamer loss happened before Fab interaction.

4.8 Conclusions and Discussion

Attachment of polyclonal antibody (pAb1 and pAb2) to poliovirus type 1/2/3 VLPs has been studied with structural biology tools. Even at the level of icosahedral reconstructions it was obvious for one of the reconstructions, PV1 VLP expanded particles, that there was a dominant class of pAb1 attached almost exactly on the 2-fold axis. This type of Fab attachment potentially neutralizes poliovirus as poliovirus RNA is released near the 2-fold axis [281] (Figure 4.3.all), and in this region there are major conformational changes between native and expanded particles. However there was no evidence that the antibodies had altered the balance of native vs expanded particles. Therefore it seems that in serum from immunised individuals there is a high level of response to the expanded particle. These particles (antigenic form C) do not elicit neutralising antibodies [282] [273], it is the level of D (native) antigenicity that is the critical metric for the release of batches of polio vaccine. This suggests that the usual vaccination regime elicits high levels of non-productive immune responses, implying that much of the vaccine antigen is not in the useful native state.

Indeed beyond the 2-fold binders, the SyRe protocol was developed to run protomer level 3D classification. In this way, the dominant 2-fold Fab could be further classified into one major class and several minor classes. In a similar way, the SyRe protocol managed to sort out several classes of pAb1 binding to poliovirus type 1 expanded particles at the 3-fold axis, southern rim and northern rim of the canyon. The limitation of the SyRe protocol is 1000

particles per class. (Figure 4.4.all and 4.5.all). Again these binders could not be detected bound to native antigen.

SyRe protocol protomer-scale classification was also applied to the native antigenicity datasets but no such major nor minor classes of surface bound Fabs were found. However, the SyRe protocol pentamer-scale classification managed to detect that all the natural particles (non-expanded) lost 3-4% of total pentamers. This is not caused by antibodies because non-antibody control group also lost 3-4% pentamers.

Interestingly, dominant classes of pAb1 and pAb2 are found attaching to PV2 and PV3 at the pentamer-pentamer interface in particles missing a pentamer and exposing this interface. This cannot happen to intact particles but only to the ones that have lost 1 or more pentamer. These Fabs bind to similar epitopes but vary in pose. In rare cases 2 Fabs attaching to one pentamer can be seen. These dominant classes of Fabs may interfere with viral assembly and therefore inhibit viral replication, however since assembly occurs within the cell this seems unlikely (Figure 4.6.all).

Finally, using SyRe protocol pentamer-scale classification, a rare class of semi-attached pentamer was found, which may be an intermediate status of viral assembly or disassembly. (Figure 4.7.1) or may represent the first detailed glimpse of the breathing particle. Note that while it has been proposed that the breathing may reflect a transient transition to the expanded state the new ‘semi-attached’ state is a more attractive candidate, since conversion to the expanded state would likely be irreversible, setting the virus on a pathway to uncoating.

Chapter Five

Enterovirus A71 - SCARB2 – nanodisc

Major achievement:

1. Improved the cMSP26 method and production efficiency
2. Increased the amount of EV71:nanodisc complex per field of view
3. Discovered a middle sized nanodisc
4. Determined that pH 5.5 is likely to trigger the virus uncoating

5.1 Introduction

The penetration of viruses into host cells necessitates the disruption of the host cell membrane while preserving the cell's overall integrity. This critical stage of infection is controlled by glycoproteins embedded in enveloped viruses [283], while hydrophobic capsid peptides carry out this function in non-enveloped viruses [284]. Despite intensive study, it is still unclear how simple non-enveloped viruses such as poliovirus breach the limiting membrane of the vacuole within which they are enclosed. Questions persist regarding the specific mechanisms of membrane penetration, virus disassembly, conformational changes, and the influence of host factors. Unfortunately, observing the virus during the moment of membrane interaction presents a significant challenge, which remains the primary obstacle in studying viral cell entry.

Recent cryo-electron tomography studies, utilizing a liposome system decorated with receptors, have provided significant insights. These studies demonstrated that poliovirus 135s particles create 50 Å connectors, attaching the virus to the membrane and establishing a pathway for the viral genome, thereby initiating infection [285]. Additionally, cryo-EM tomography investigations on rotavirus particles revealed a direct interaction between VP4 spikes and the membrane [286]. Similarly, human rhinovirus 2 (HRV2) particles were observed to bind to the membrane around a 2-fold icosahedral symmetry axis [287].

Although these studies have shed light on the transition of the capsid and the interaction between viruses and membranes, progress is hindered by the limitations of using liposomes as a model for membranes. To overcome these limitations, the utilization of large nanodiscs has emerged as a promising alternative due to their ample surface area, homogeneity, and stability [288] [289]. These nanodiscs serve as surrogate membranes and enable the investigation of

stepwise alterations involved in viral entry for most viruses. In a previous study, a covalently circularized nanodisc measuring 50 nm in diameter was employed to examine how poliovirus attaches to the membrane and transfers its genome into host cells [288]. Electron microscopy (EM) images were captured, demonstrating the binding of poliovirus to 50 nm nanodiscs decorated with poliovirus receptors. Additionally, the study revealed the formation of a putative pore and the ejection of RNA across the membrane (Figures 2A,B) [288]. Similarly, using 45-nm DNA-corralled nanodiscs functionalized with His-tagged poliovirus receptor ectodomain, the receptor-mediated uncoating of poliovirus was successfully initiated, and initial stages of virus attachment to the bilayer were observed [289].

However, to fully understand the mechanisms underlying virus cell entry, it is essential to conduct structural analyses of virus uncoating and membrane penetration at the near-atomic level. Here, a split-intein based approach was employed to efficiently produce circularized membrane scaffold protein (cMSP26) measuring 26nm in size (Figure 5.1.1) [218]. Anionic phospholipids, specifically phosphatidylglycerol and phosphatidic acid, were utilized due to their ability to quickly diffuse between the bilayer leaflets in their uncharged, protonated state [290] . To properly decorate the nanodisc with the appropriate virus receptors, Ni-NTA molecules were incorporated among the phospholipids. Unfortunately, due to certain national safety regulations in the UK, the ability to conduct experiments with poliovirus was restricted. As a result, the study instead focused on enterovirus A71 (EV71), another example of a non-enveloped virus.

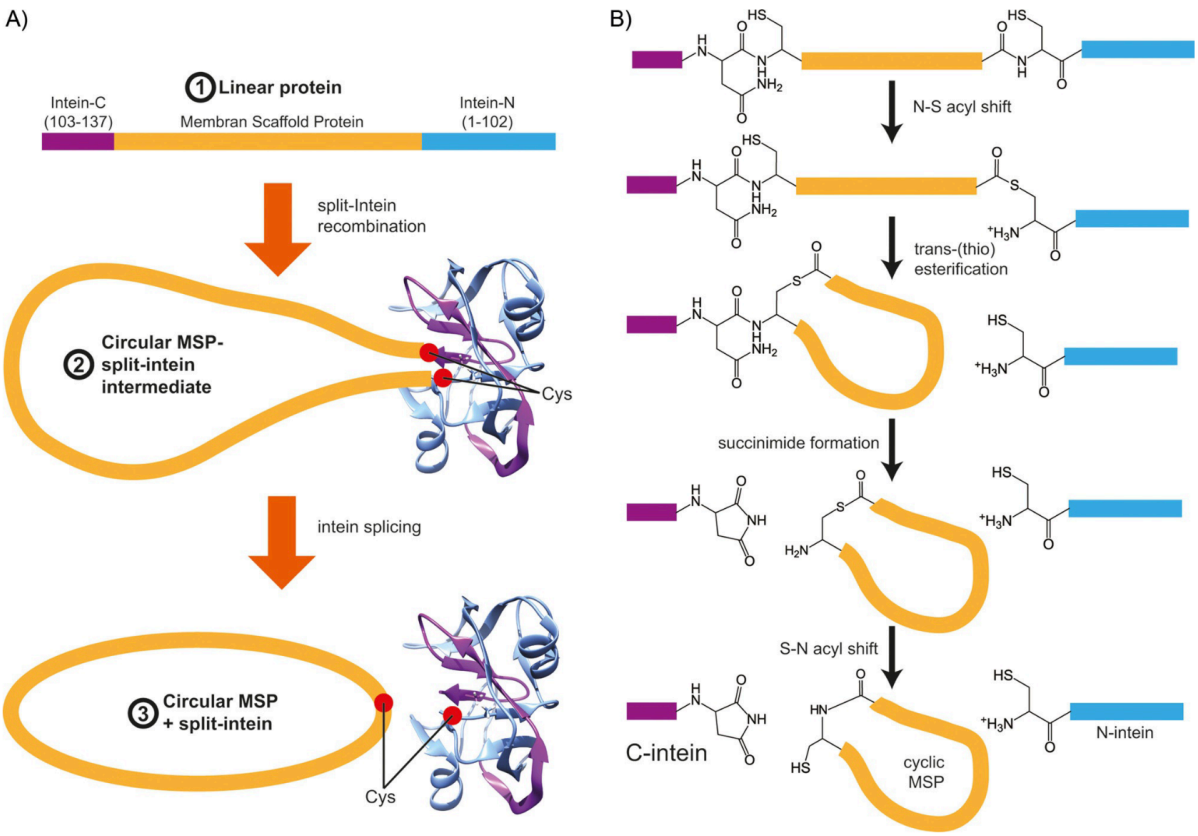


Figure 5.1.1 Split intein-based strategy for the production of cMSP26 in vivo [218].

A) Design of the *Npu* DnaE split-intein MSP fusion construct and mechanism of intein splicing in vivo, leading to the generation of cMSP. N-intein (aa 1-102) and C-intein (aa 103-137) are shown in blue and magenta, respectively. Intein structural coordinates were taken from PDB: 2KEQ) [291]. The essential cysteine residues are marked by red dots. B) Mechanism of intein splicing with the MSP and two split intein fragments coloured according to the scheme in A

EV71 and coxsackievirus A16 are significant causative agents of hand, foot, and mouth disease (HFMD), which have been responsible for repeated epidemics in the Asia-Pacific region for over two decades [292]. The main receptor for EV71 is the scavenger receptor class B member 2 (SCARB2). There is compelling evidence indicating that SCARB2 attachment facilitates the internalization and uncoating of EV71 [293] [294]. However, it has been established that uncoating requires not only attachment to SCARB2 but also a low pH environment [295]. This suggests that binding to SCARB2 may destabilize the virus particle under low pH conditions, leading to the formation of expanded or "A-particles" [296] [36].

SCARB2, also known as lysosomal integral membrane protein-2, is a type III membrane protein that possesses amino (N)- and carboxy (C)-terminal transmembrane helices [297]. Although it binds EV71 at the plasma membrane it is primarily found in lysosomal limiting membranes, and its luminal domain, consisting of 400 residues, is heavily glycosylated with nine potential N-linked glycosylation sites [298]. SCARB2 plays a crucial role in the organization of endo/lysosomal membranes, and mutations in this protein have been associated with various neurodegenerative and renal diseases [299].

The structure of EV71 in complex with the luminal domain of SCARB2 has previously been successfully determined under low pH conditions [19]. This achievement greatly facilitated my study of the VRNC with EV71. A detailed description of the methodology used to generate the VRNC can be found in Chapter 2 of this thesis.

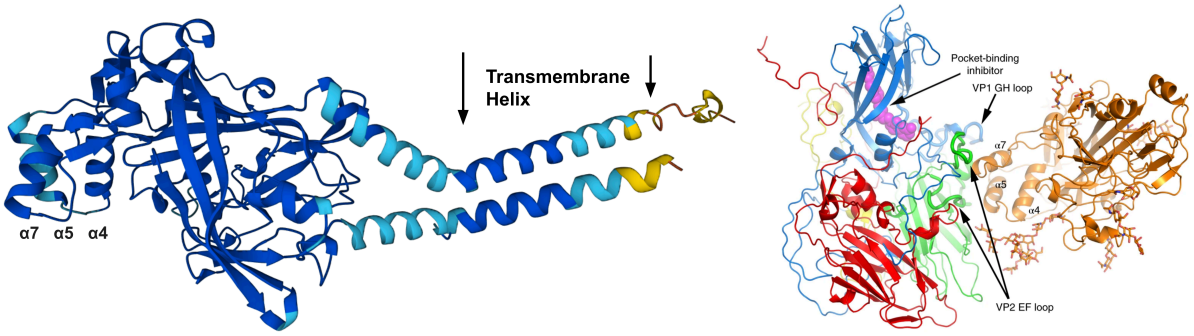


Figure 5.1.2 Alphafold structure prediction of SCARB2 (left) and SCARB2-EV71 interaction mainly at α7 and α5 (right, PDB:6I2K) [19]

In summary, the cMSP was expressed in *Escherichia coli (E. coli)* and subjected to several purification steps (till Size Exclusion A, Figure 5.1.3). The purified cMSP was then used to wrap the lipids, which were initially formed into micelles with the assistance of Na-cholate. The Na-cholate was subsequently removed using biobeads, and the cMSP effectively enveloped the lipids, resembling a belt-like structure (Figure 5.1.4). To purify the nanodisc and eliminate any unwanted components, the mixture underwent a size exclusion step referred to as Size Exclusion B (Figure 5.1.3). Following this, the extracellular domain of SCARB2, fused to a 6xHis tag, was mixed with the purified nanodisc and bound to the Ni-NTA molecules present among the lipids of the nanodisc. Any excess SCARB2 was removed through Size Exclusion C. Finally, EV71 was introduced into the sample and visualized using transmission electron microscopy (TEM).

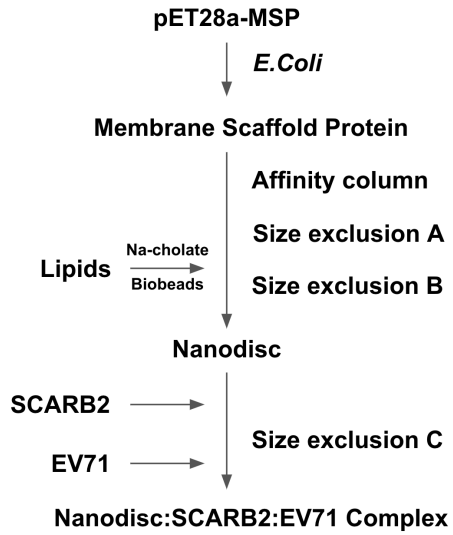


Figure 5.1.3 Flowchart of generating the Nanodisc:SCARB2:EV71 complex

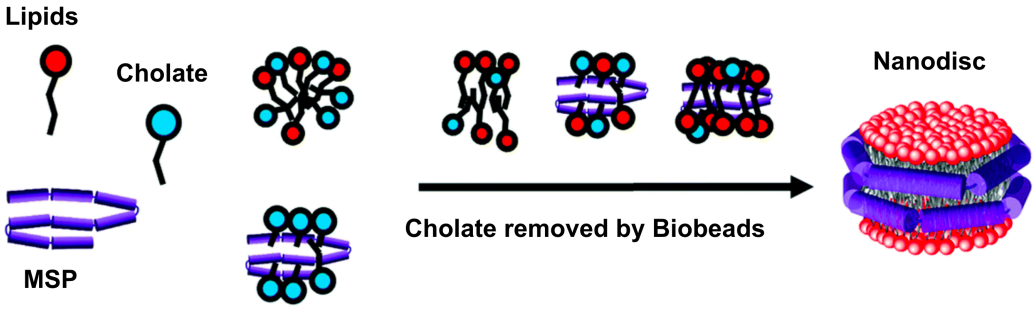


Figure 5.1.4 The process of forming a nanodisc

5.2 Nanodisc(His)-SCARB2-EV71 complex

The production of nanodiscs involves three important size exclusion steps (Figure 5.1.3). These steps are crucial for obtaining a purified nanodisc stock and also play a vital role in assessing the quality and integrity of the sample.

During the size exclusion A step (Figure 5.2.1), the input sample has already undergone an affinity column process. As a result, theoretically, the sample should only contain components with a binding affinity equilibrium dissociation constant (K_d) falling between 20 mM imidazole and 200 mM imidazole, corresponding to the binding affinity for immobilized nitrilotriacetic acid (Ni-NTA) resin. However, examination of the SDS-PAGE (outside the red square) and the first UV absorption peak during size exclusion, shows that this purification step is not flawless.

Although the goal is to achieve a perfect result at each purification step, the experiments proceed using the protein fraction from peak B (Figure 5.2.1), which corresponds to the membrane scaffold protein and is relatively pure, and it turns out it that this has no influence on the later experiments.

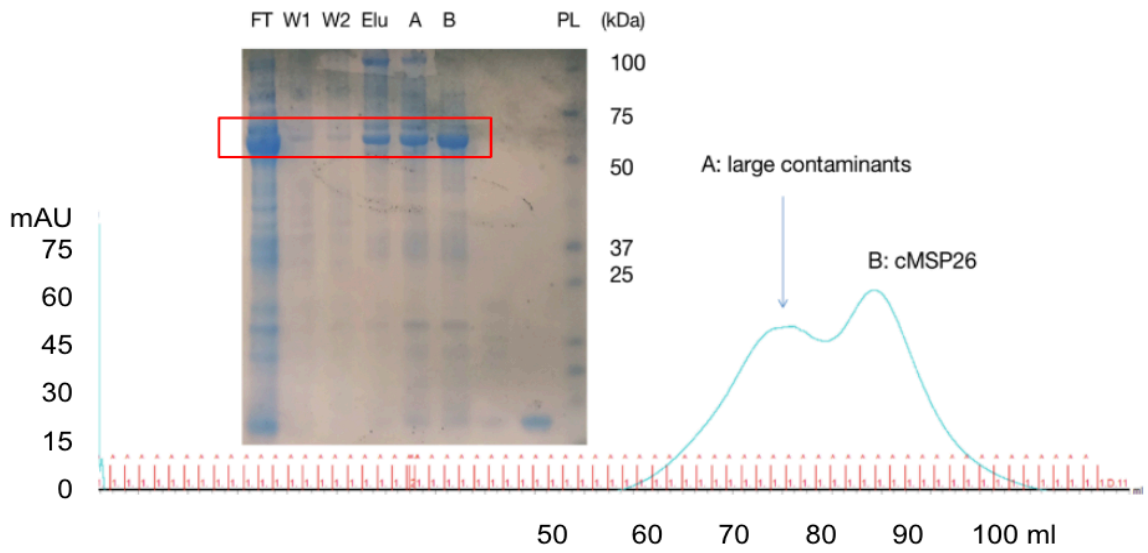


Figure 5.2.1 SDS-PAGE result of affinity column and size exclusion (Superdex 200) result of His-tag circularised Membrane Scaffold Protein (cMSP26-His) purification
FT: Flowthrough sample of affinity column. W1: Buffer (no Imidazole) wash.
W2: Buffer (20mM imidazole) wash. Elu: Buffer (200mM imidazole) elution.
PL: standard protein ladder. Red square: cMSP26-His (65kDa).

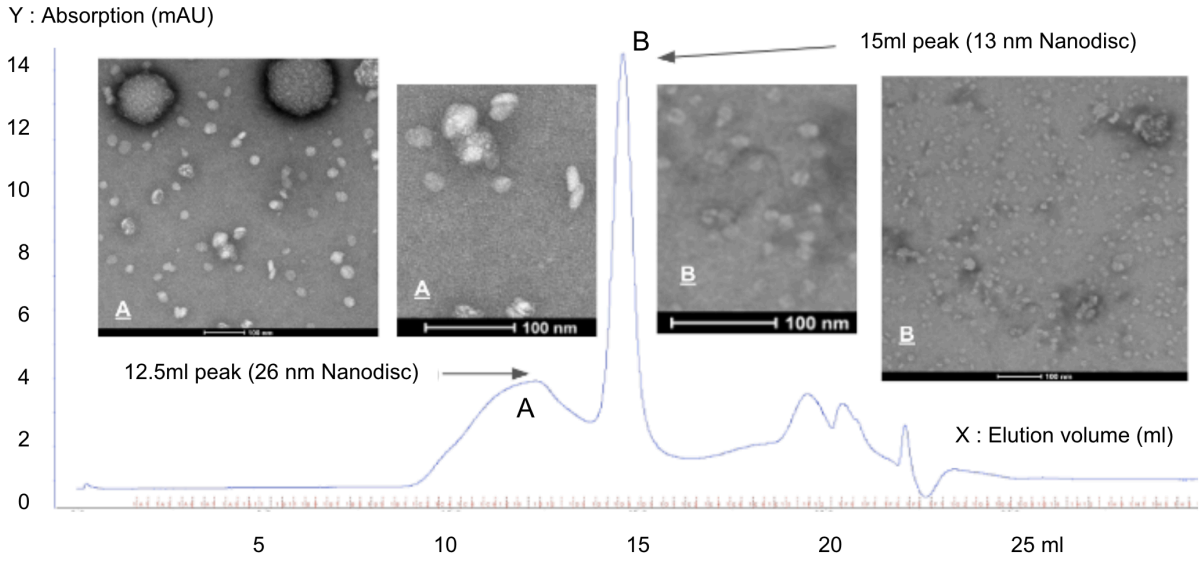


Figure 5.2.2 Size exclusion (superose 6) and negative stain EM result of His-tag nanodisc assembly

The generation of nanodiscs involves a process of mixing the desired lipids with cholate, followed by the replacement of cholate with purified membrane scaffold protein. Initially, the cholate is removed using a biobeads extraction step, as described in the methods (chapter 2). Subsequently, a complete removal of cholate is achieved through a size exclusion step, referred to as size exclusion B. This step involves gradually diluting the sample with a non-cholate buffer while passing it through a superose 6 column. The output of size exclusion B is composed of pure assembled nanodiscs, which exhibit two different sizes (Fig. 5.2.2). Since EV71 is a spherical particle with a diameter of approximately 30nm, nanodiscs with a size of 26nm are specifically collected for further experiments as they closely match the dimensions of the EV71 viral particle.

The third size exclusion step is conducted subsequent to the mixture of 26nm nanodiscs with an excess of the extracellular domain of SCARB2, with the intention of removing any unbound EV71 receptor (Figure 5.2.3). The binding of SCARB2 to the nanodiscs occurs through the interaction between the 6xHis tag on SCARB2 and the Ni-NTA molecules present among the lipids. This interaction results in an increase in the overall molecular weight of the complex, causing the RNC to pass through the column at a faster rate compared to before SCARB2 incorporation. By examining the UV absorption curve, it becomes apparent that a new protein peak emerges at 11.5 ml, which is 1 ml earlier than the peak observed before the incorporation of SCARB2 (comparing Figure 5.2.3 with Figure 5.2.2). However the new peak is not sharp, since the number of SCARB2 incorporated vary stochastically.

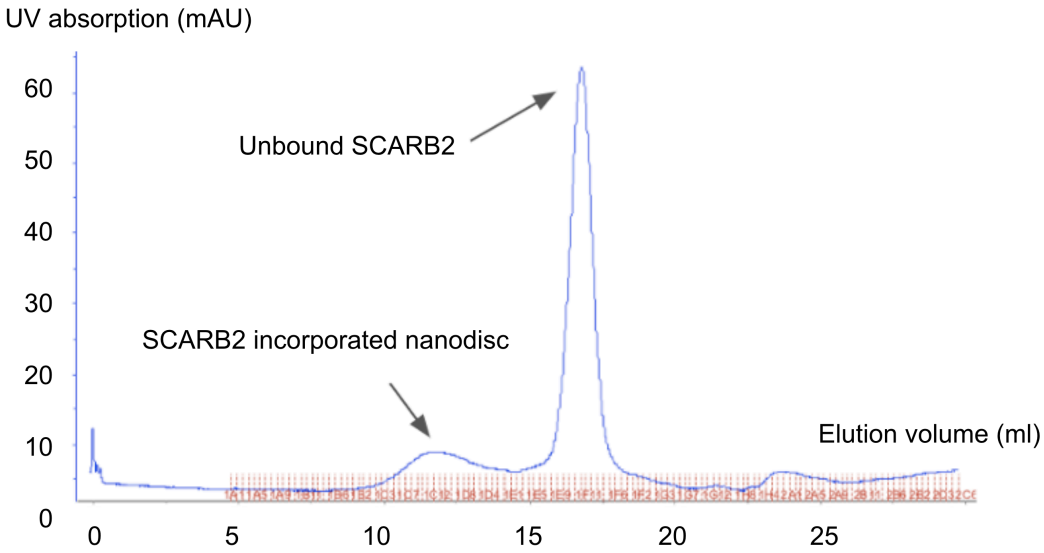


Figure 5.2.3 Size exclusion result of SCARB2 incorporated nanodisc

Size exclusion steps B and C utilize Superose 6 Increase resin to separate nanodiscs based on their differences in molecular weight. In contrast to the Superdex 200 resin used in step A, Superose 6 provides improved separation for molecules with a relative formula mass ranging from 500,000 Da to 1,400,000 Da. This enhanced separation is evident by the spreading out of the elution of these molecules from 11ml to 20ml, avoiding the crowding observed at the elution fraction around 9ml with Superdex 200 (as shown in Figure 5.2.4).

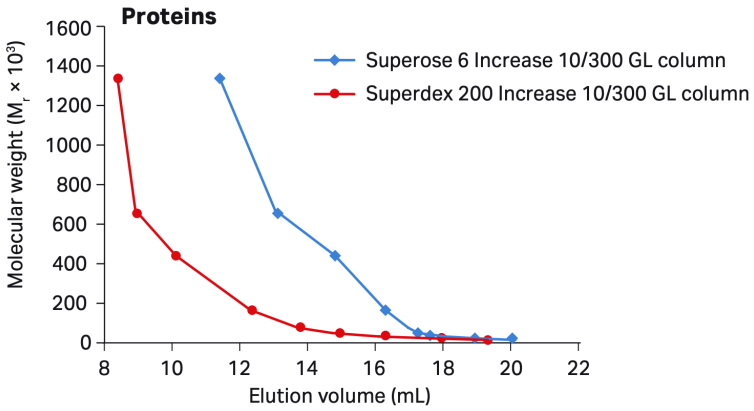


Figure 5.2.4 Selectivity of Superose 6 Increase chromatography resin compared with Superdex 200 Increase for a range of proteins from M_r 1,400,000 down to M_r 6500 (Image from Citiva)

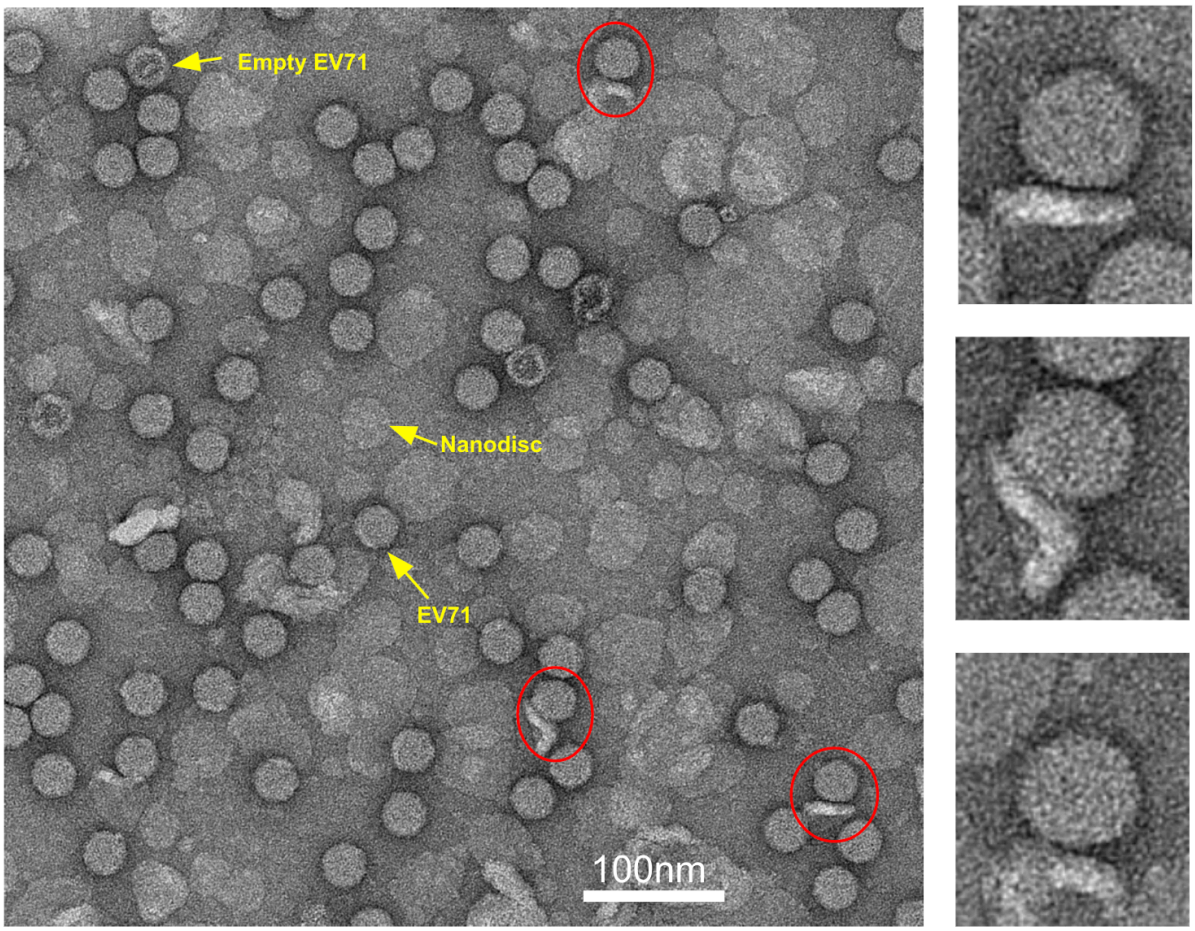


Figure 5.2.5 negative stain EM result of VRNC. Yellow arrows point out free (empty) virus particles and nanodiscs. Red circles highlight the three VRNC.

The incorporation of human SCARB2 into the nanodisc creates a comprehensive membrane simulation system. By combining this system with EV71 particles, images were obtained using negative stain (TEM), (Figure 5.2.5). The image presented above represents one of the highest-quality images captured during the experiment, but only three VRNCs could be observed in side-view, and that is the only way to confirm nanodisc-EV71 interaction at this stage. Potentially, there are a certain of nanodisc hiding behind the virus that cannot be visualized from top view. This can be solved by tilting the sample stage when collecting cryo-EM images. On average, the current methodology allows for the confident detection of approximately one VRNC per image. Therefore, the formation of VRNC may be exceptionally rare in this experimental setup. One possible reason for the limited formation of complexes could be the lack of opportunity for the virus particles to come into proximity with the nanodisc. At this stage, nanodisc and EV71 were simply mixed and place in a tube a 4˚C for 1 hour. To address this issue, one potential solution is to immobilize the nanodisc and allow the virus particles to flow through, maximizing the chances for the virus to interact with the nanodisc. This approach creates an environment where the virus particles have a higher likelihood of approaching and potentially forming complexes with the immobilized nanodisc.

5.3 Nanodisc(StrepII)-SCARB2-EV71 complex

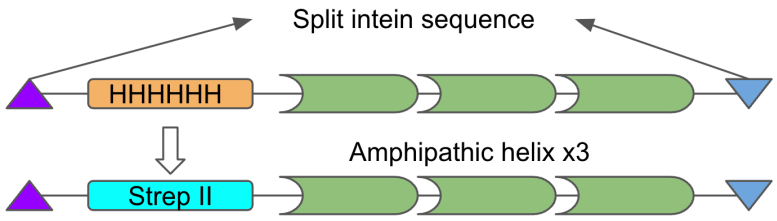


Figure 5.3.1 Diagram of changing affinity tag of MSP26 gene

In this study, a cloning method was employed to switch the affinity tag of the membrane scaffold protein from 6xHis to StrepII. There were two primary reasons for this modification. Firstly, removing the 6xHis tag was necessary to prevent the presence of both cMSP and SCARB2 with the same tag, thereby minimizing any potential mis-assembly in the process of assembling RNC. Secondly, the addition of the StrepII tag enabled the immobilization of nanodiscs to the Strep Tactin column, therefore enriching the VRNC became feasible. A comprehensive description of the methodology can be found in Chapter 2. In the present section, the results of StrepII-nanodiscs are presented and compared with the results obtained using 6xHis-nanodiscs in the previous section.

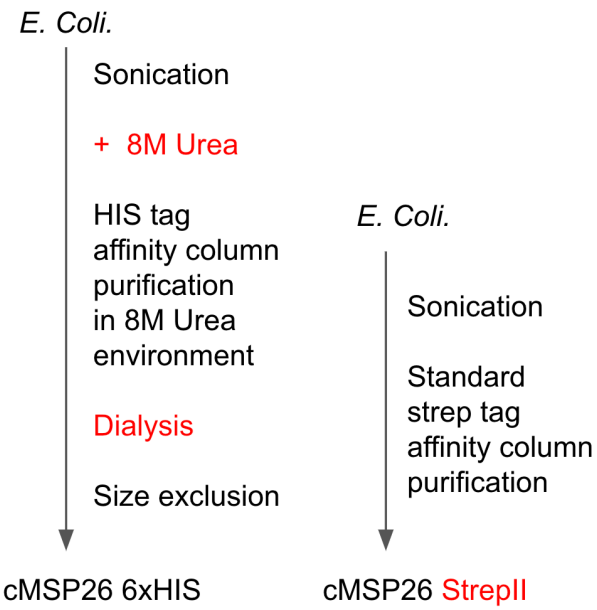


Figure 5.3.2 Comparison of experimental workflow of cMSP-6xHis and cMSP-StrepII.

Similarly, the plasmid for expressing cMSP was transfected and expressed in *E. coli*. However, the purification process was significantly simplified. Initially, an 8M Urea solution was applied to the sample to denature the cMSP, exposing the 6xHis tag for binding to its affinity column. With the StrepII tag, this step is no longer required, as the StrepII tag is larger than the 6xHis tag and exhibits a higher affinity for its respective affinity column. As a result, the dialysis process to remove the high concentration of Urea is also unnecessary (Figure 5.3.2). This streamlined purification approach saves time and eliminates the need for additional steps in the purification process.

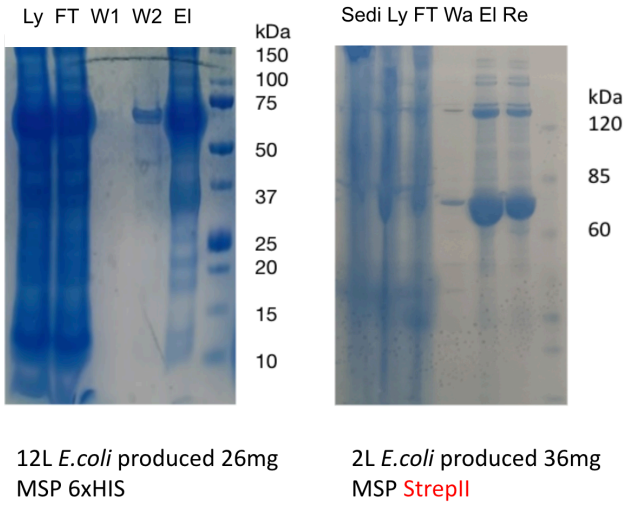


Figure 5.3.3 Comparison of SDS-PAGE result of affinity chromatography. Sedi: precipitates after cell lysate. Ly: supernatant after cell lysate. FT: flowthrough sample of affinity column. W1: Buffer (without Imidazole) wash. W2: Buffer (with 20 mM imidazole) wash. El(left): elution with Buffer (200mM imidazole). Wa: Buffer (no Biotin) wash. El(right): elution with Buffer (with 50mM Biotin). Re: regenerate affinity column with 10mM NaOH. Last column of each SDS-PAGE: standard protein ladder.

Application of this simplified workflow with the StrepII tag worked extremely well, as may be seen from the significant increase in the yield of cMSP-StrepII, even when the over-expression is less compared to cMSP-His (Figure 5.3.3). The SDS-PAGE results of the affinity purification step highlight this difference, with a prominent band of cMSP-6xHis observed in the supernatant sample after cell lysate, while no obvious band of cMSP-StrepII is observed.

Further comparison of the flow-through (FT), wash (W1/W2/Wa), and elution samples (EL) from the affinity chromatography process reveals a substantial improvement in purification efficiency with cMSP-StrepII using the Strep Tactin column. cMSP-StrepII demonstrates a higher binding capacity for the target protein, resulting in less target protein being washed out during the purification process and a cleaner elution of the target protein.

As a result, the outcome yields 36mg of cMSP-StrepII from a 2L *E. coli* culture, which is approximately 9 times higher than the production rate achieved with cMSP-His (Figure5.3.3). This significant increase in production demonstrates the advantages of the simplified workflow and the utilization of the StrepII tag.

Following the purification of cMSP-StrepII, the assembly of nanodiscs and their incorporation with SCARB2 proceeds similarly to the approach employed with cMSP-6xHis. However, a notable difference arises when comparing the 26nm and 13nm nanodiscs: the emergence of an additional population of nanodiscs of intermediate size (~20nm). This presented a challenge in terms of separation from the larger (and desired) 26nm nanodisc (Figure 5.3.4). The nature and characteristics of this 20nm nanodisc warrant further investigation, as its formation and distinct properties are currently not understood.

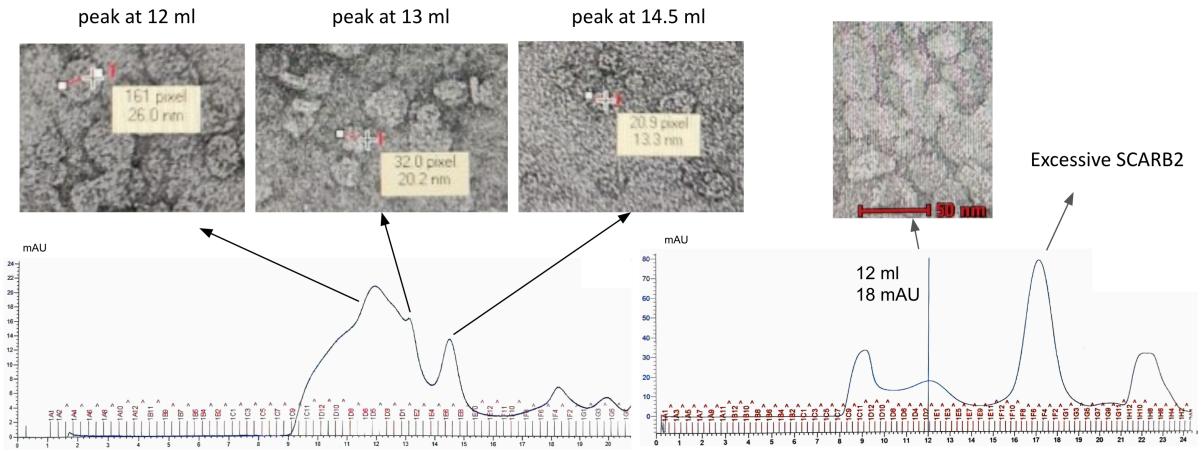


Figure 5.3.4 Size exclusion and negative stain EM result of nanodisc (StrepII) assembly and SCARB2 incorporation to nanodisc.

The immobilization of RNC is achieved using a small-sized affinity column with a reduced resin volume, specifically the Strep-Tactin®XT 4Flow® high-capacity column. The assembled RNC was flowed through the column once, allowing the complex to bind to the Strep Tactin resin in the column. Subsequently, the virus was flowed through multiple times, with the last pass allowing for a 1-hour binding period (RT, 4˚, pH7.5). Despite the immobilisation of the RNC to the Strep-Tactin®XT resin, a small amount of (20% of the total number of objects in the field of view) RNCs were washed out during the virus binding step, observed in the TEM micrographs (Figure 5.3.5). Post-incubation and removal of the flowthrough, the RNC and VRNC were eluted from the column using biotin, and the elution peaks were examined with negative stain TEM.

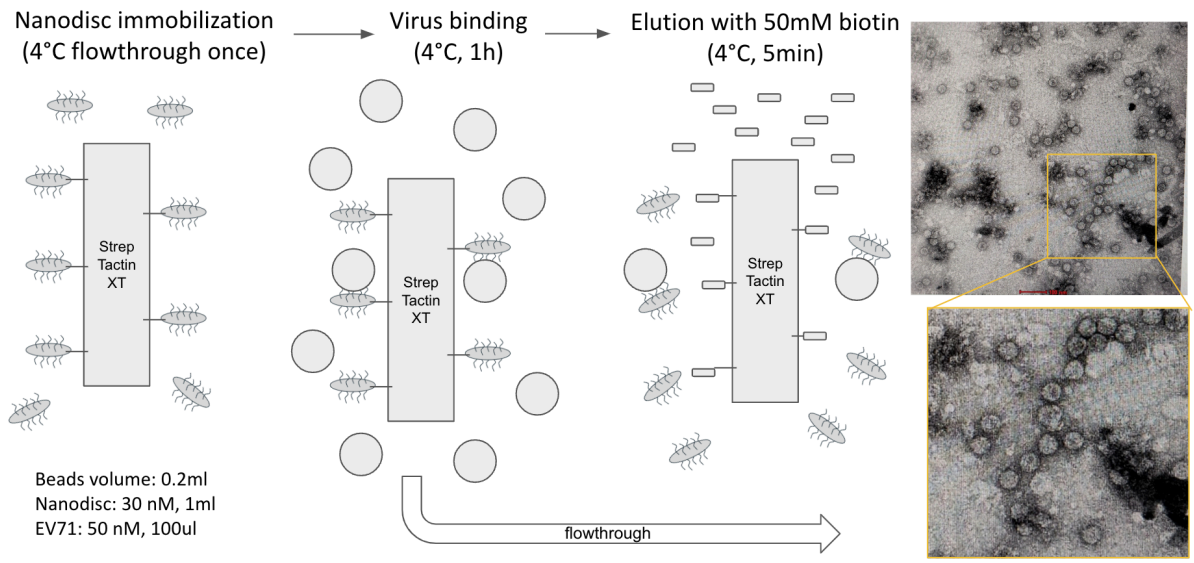


Figure 5.3.5 Flowchart of VRNC forming procedure and negative stain EM result of flowthrough EV71

The elution outcome depicted in the negative stain sample (Figure 5.3.6) is not entirely satisfactory. The sample appears to be crowded with RNC, with only approximately 10% of them being in close proximity to virus particles and presumably forming VRNC. Most of the virus particles are found adjacent to at least one nanodisc, indicating that the virus receptor is functioning, and has successfully attracted the virus to form VRNC. The current acquisition yields a maximum of 7 VRNCs per field of EM view, with an average of 4 VRNCs. Among the 7 VRNCs shown, 4 of them have a nanodisc attached next to them rather than underneath, which may provide better EM data for reconstructing the virus receptor and its position. With a reasonable number of VRNC formed, the next question to address is how to trigger membrane penetration.

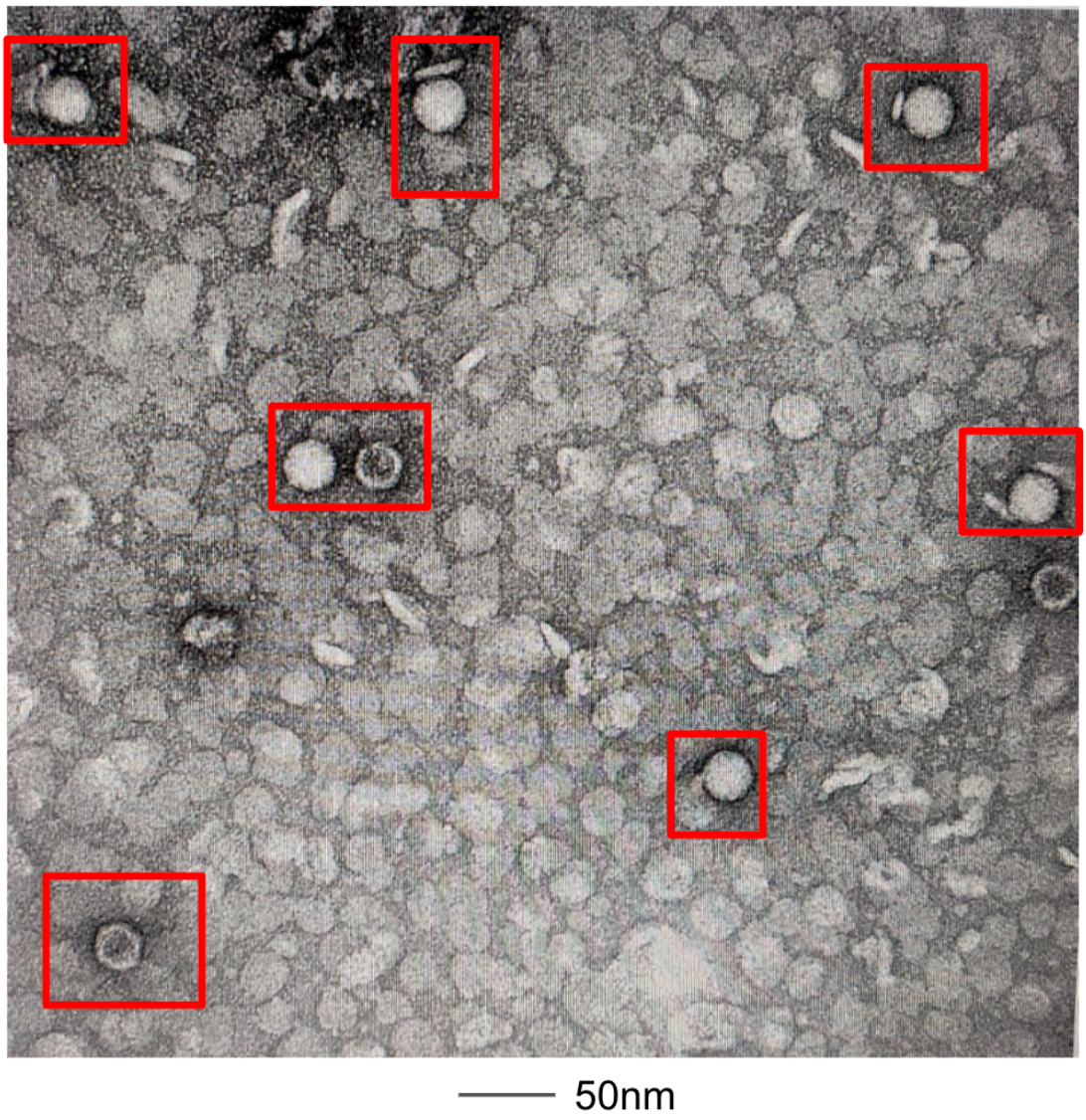


Figure 5.3.6 Demonstration of improved VRNC

5.4 Environmental trigger

Although acidic pH is a requirement for triggering the release of EV71 capsid expansion and genome release, the kinetics of the process are poorly understood. Thus, a 'PaSTRy' assay was performed with EV71 virus and SCARB2 (see Methods) [232]. In short, samples were heated from 25 to 99 °C, fluorescence (Syto9 (monitoring RNA release) / SyproRed (monitoring protein denaturation)) was recorded in 1 °C steps, and a Sigmoid S curve fitted to the resultant plot to calculate three important temperature values – T_{start}, T_{half}, $T_{complete}$ (an example shown in Figure 5.4.1).

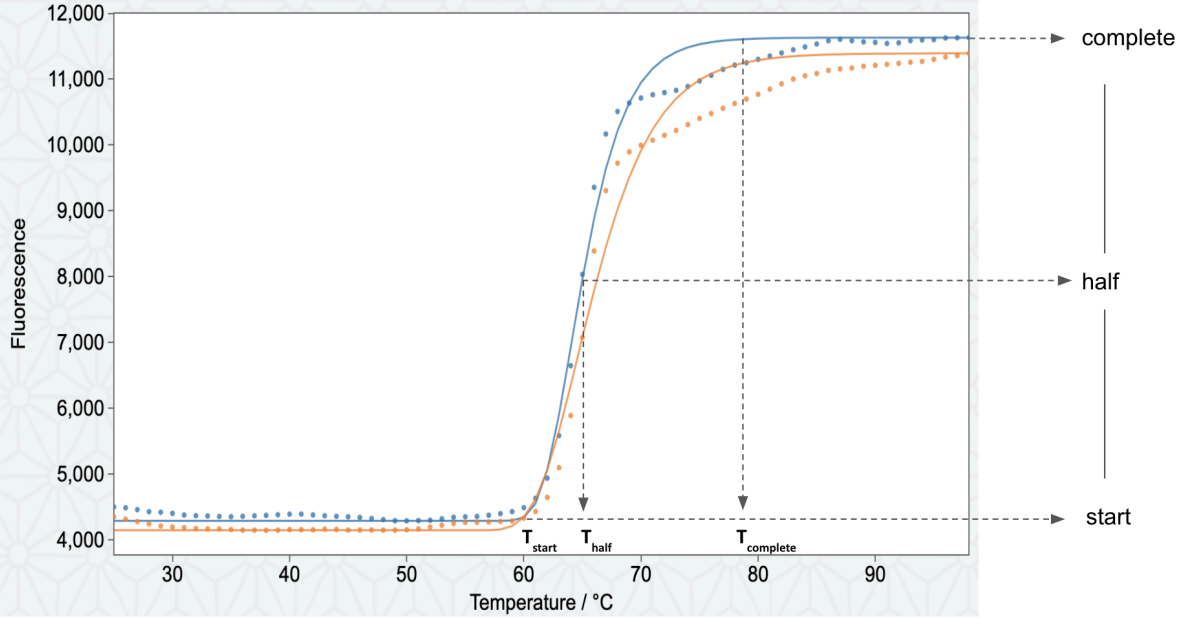


Figure 5.4.1 Demonstration of how the 3 key parameters are calculated
pH 5.5, Syto 9 fluorescence, EV71 only. The duplicate test data curves (blue and orange) are only for demonstration, they are not used in Figure 5.4.2.
T_{start} : The temperature when fluorescence starts increasing in the fitted Sigmoid curve
$T_{complete}$: The temperature when fluorescence stops increasing in the fitted Sigmoid curve
T_{half} : The temperature when fluorescence reaches half of the increasing value in the fitted sigmoid curve

Comparing the three key temperature values (T_{start}, T_{half}, $T_{complete}$) for EV71 with the EV71:SCARB2 complex at different pH values yielded the curves shown in Figure 5.4.2. From this result, three obvious differences between experimental data with/without the presence of SCARB2 were observed (main conclusion A, B, C pointed out in Figure 5.4.2 A, B, C respectively):

A. At pH range 5.5-6.5, despite the completion of EV71 RNA release requiring a higher temperature than normal without the presence of SCARB2, the presence of virus receptor can lower the energy barrier: -27°C at pH5.5, -38°C at pH6.0, -7°C at pH 6.5, and enabling an easier RNA release.

B. At pH5.5, in the presence of SCARB2, the completion of EV71 capsid denaturation requires lower energy input, around -7°C.

C. At pH range 5.5-6.0, in the presence of SCARB2, the T_{half} of EV71 capsid denaturation requires a lower energy input: -10°C at pH5.5, -7°C at pH6.0.

Thus, SCARB2 facilitates EV71 RNA release at pH 5.5-6.5 and causes hydrophobic surfaces to be exposed more readily i.e. triggering virus capsid disassembly at around pH 5.5. Taken together this confirms the catalytic role of SCARB2 in facilitating the exposure of the genome to the environment by lowering the energy barrier of the viral capsid denaturing and viral RNA release at certain low pH conditions.

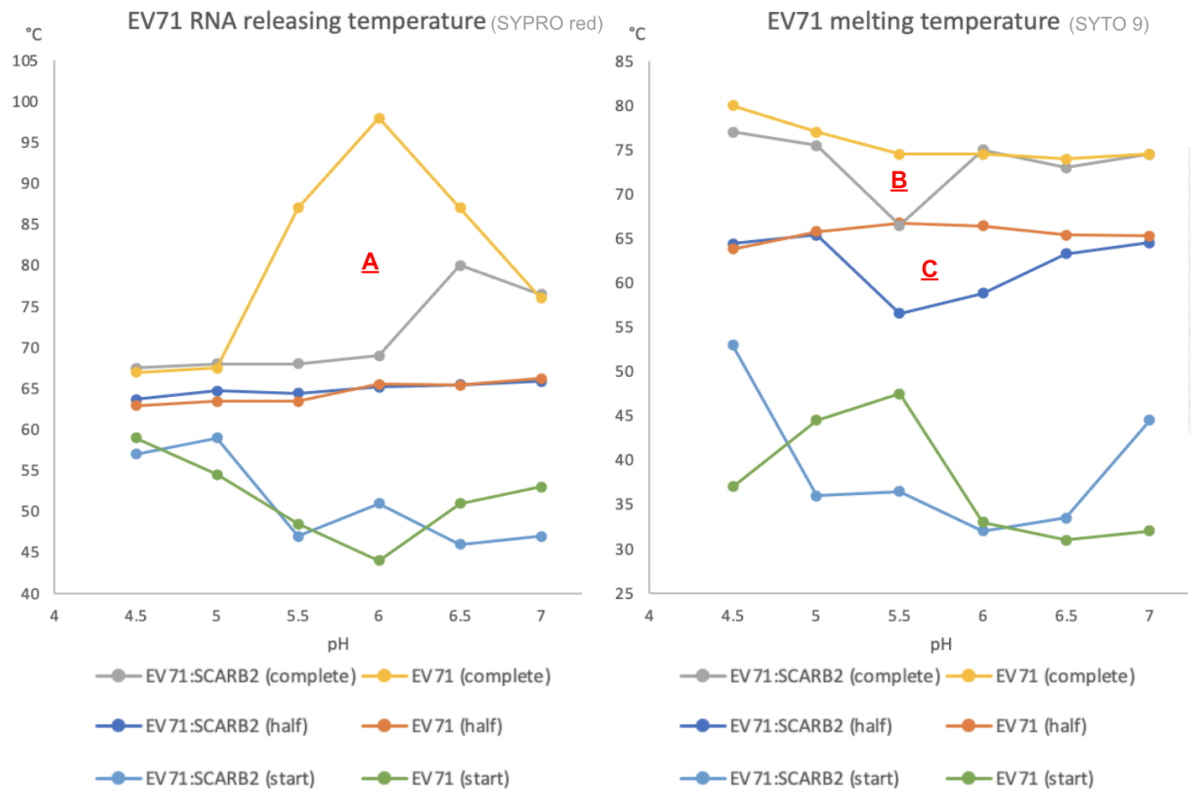


Figure 5.4.2 EV71 RNA releasing and protein melting condition (temperature and pH)

5.5 Conclusion and Discussion

Due to the ample surface area, homogeneity, and stability of large nanodiscs, it has emerged as a promising tool to serve as surrogate membranes and enable the investigation of stepwise alterations of viral entry for most of the non-enveloped viruses [288] [289]. However, the investigation only works if VRNC amenable for structural characterisation by single particle EM can be prepared. Thus, there is a need to optimise the quality and yield of the VRNC to meet the requirement of 3D reconstruction in atomic-level resolution and structural analysis of viral entry.

The experimental results presented in this chapter provide an optimized method of generating 26nm nanodiscs with higher efficiency and productivity, and for the first time, several VRNCs per field of EM view have been achieved. This is a breakthrough in comparison to rarely captured VRNC images from the previous papers [288] [289]. However, it is still not enough to unravel the mystery of EV71 virus entry in structural details until two main issues are solved.

Issue 1: Although the enterovirus capsid possesses icosahedral symmetry, the VRNC is most likely to be in asymmetric form with only one or two nanodisc(s) attaching to the virus. Therefore, it requires 60 times more particles to be collected than for enterovirus alone to resolve an equally good cryo-EM density map for structural analysis. Let alone the potential unsteadiness of the key area (pore-forming area) which require even more data to be collected. The current sample with the result of 4 VRNCs per micrograph in average will require an extensive amount of data collecting time (approximately 15 days if aiming for one million particles) to provide enough VRNCs to be analysed in sub 3Å resolution.

Issue 2: Unlike poliovirus [288], it is unknown if the experimental conditions have met the prerequisite of EV71 membrane penetration. I have tried to find the most suitable pH value for the experiments, but further experiments are needed to prove that nanodisc can function at low pH and the pH-temperature-timing combination for triggering the penetration also requires further investigation. Besides, *in vivo*, it is the full-length SCARB2 functioning on the cell surface as an uncoating receptor and probably solely led to membrane penetration, but only the extracellular domain of SCARB2 was tested in this thesis. Nanodisc assembly with the full-length SCARB2 might be a useful direction to explore.

Chapter Six

Conclusions and Future directions

With the advances in cryo-EM, structural biology has become a systematic way of analysing and understanding the most fundamental biological mechanisms based on structural features and molecular interactions. In this thesis, I have presented three diverse structural studies using echovirus 11, poliovirus VLPs, and enterovirus A71 all of which are classified within the enterovirus genus.

In chapter three, the atomic-level structure of echovirus 11 in complex with full length ectodomain attachment receptor DAF was solved for the first time. An unexpected glycan connector is observed in the status of virus-receptor interaction for the first time. The function of the glycan connector and whether it facilitates virus-receptor interaction or even cell entry remains unknown and requires future experiments.

Also in chapter three, DAF binding modes are classified into E11 mode and E6 mode, and all nineteen DAF-binding enteroviruses are analysed using a phylogenetic tree to examine their evolutionary history. Sequence alignment of the key residues related to receptor attachment found in 6 resolved enterovirus-DAF structures also supports the E11 and E6 binding modes. Further sequence alignment of the other DAF-binding enteroviruses suggests that DAF might attach echovirus 19 in E11 mode, and this requires further structural study to verify.

Thanks to the advance of computational methods, the question of whether 30 or 60 DAF can bind one echovirus 11 simultaneously was resolved three years later in 2022 by mask-focused 3D classification without alignment job using CryoSPARC™, and the answer is 30 due to steric hindrance (chapter three).

In a similar way, computational advances allowed the ‘SyRe’ protocol to be developed to analyse the interaction of polyclonal responses from vaccines with poliovirus VLPs (chapter four).

In chapter four, Fab-scale SyRe protocol managed to separate several minor classes (1000+ particles) of Fab attachment with minimum differences from the one major 2-fold Fab class. Protomer-scale SyRe protocol managed to separate several minor classes (1000+ particles) of Fab attachment to different epitopes. Pentamer-scale SyRe protocol managed to detect a completely unexpected epitope at the inside edge of a pentamer that only accessible when at least one pentamer is missing from a poliovirus particle. The reason why pentamers are missing from VLPs and whether the pentamer-interface Fab has anything to do with the absent pentamer remains unknown and is an intriguing direction for further exploration.

Analysis of the polyclonal response needs to be further developed but it is already very striking that, although it is generally accepted that antibody responses against expanded (C form antigenicity) do not confer protection, only the expanded particles showed detectable decoration on their outside surface. Note that this was true both for NIBSC standard serum and also for serum derived from an individual (although the full set of experiments was not fully completed). Even more unexpected was the discovery that in both NIBSC and individual serum the only detectable responses against the native (D-form) antigenicity were against cryptic epitopes at the pentamer-pentamer interface. Thus there was no evidence that either serum, contained significant levels of antibodies against any of the accepted antigenic sites (mapped mainly in

rodents). It is clear that further analyses will help us understand vaccine responses and may have a role to play in the regulatory processes required for licensing new vaccines, and in guiding the improvement of vaccines, although it must be remembered that extant polio vaccines are amongst the longest lasting and most effective, making the results presented here all the more remarkable.

In chapter five, an *in vitro* cell membrane mimetic system is established and enterovirus A71 was tested on the system. An improvement of the membrane scaffold protein significantly simplified the whole procedure and enabled the system to form more VRNC than before. Although the current VRNC concentration in EM sample is not suitable for SPA, with improved image shift methods for tomography [300], it would be useful to collect tomography data of VRNC in the future. Since collection of a tomogram in 5 minutes would multiply the analysable VRNC data and the Falcon-IV/Selectris would allow a higher resolution result than currently available, the structural details of virus cell entry and membrane (nanodisc) penetration may be resolved.

Despite some preliminary PaSTRy data, the exact environmental condition to trigger the membrane penetration of enterovirus A71 remains unknown. However, for future work studying enterovirus membrane penetration with the nanodisc system, it is recommended to work with a virus that does not require such harsh conditions.

In summary, whilst in the early days of cryoEM analysis of virus structures tended to focus on the analysis of dominant classes and to use capsid symmetry to obtain an average of the structures present, a dominant theme of this thesis has been the demonstration that much richer data can be obtained by initially locking the analysis down with icosahedral symmetry to accurately locate and orientate the virus or virus like particles and then relaxing the symmetry to detect events that occur at lower symmetry, e.g. at the level of a pentamer or icosahedral subunit. As hinted above it is likely that in the future the distinction between single particle and tomographic analyses will blur and lower symmetry events will be mapped not only in solution but also in the context of the cell.

Acknowledgements

Normally, I am not a ‘thankful’ person, not because I am not grateful for any help or ignore the people who helped me, but because I prefer to solve any problem independently and do not count on others. However, the experience in Oxford university completely changed me and made me realize the importance of asking for help as a student and cooperation as a scientist.

During the time in Oxford (Oct 2019 – Sep 2023) , my supervisors Dave and Liz treated me like parents to their own son. My gratitude is beyond word for their acceptance of me being their student, considerate plan for my D.Phil. projects, (fortnightly) weekly update meeting to tackle all my experimental problem and issues outside campus. I totally understand that how busy Prof. David Stuart (Dave) is, and deeply touched by that he can always prioritize his student when needed. Thank you, Sir David Stuart and Dr. Elizabeth Fry!

Dr. Daming Zhou, my Chinese friend and fellow who has been working for Dave as a post-Doc the same four years as mine, provided me countless help including almost all the lab works. Whenever and whatever wet-lab problem I cannot solve, asking Daming is always the solution!

Dr. Pranav Shah, my Indian friend and fellow who came to this lab as a PI about half a year earlier than me, is full of ideas and is my closest foreign teacher who taught me high standard experimental design and train of thought. Whenever and whatever dry-lab problem I cannot solve, asking Pranav is always the solution!

Dr. Helen Duyvesteyn, an expert of cryo-EM, helped me in every single step from EM sample preparation, data collection to data processing. Her enthusiasm to science touches me that she makes me not feel sorry about asking her questions in the weekend or late night about computational problem I run into working on CryoSPARC™.

Dr. Mohammad Bahar, Dr. Claudine Porta and Dr. Mark Boyce and many other work fellows in Dave's research group and STRUBI, has provided me so many help for my research that it's beyond my ability to memorize them all.

Claire Morris, PA of Sir Dave, who has left the group a few months before but left her memory as my counsellor, which I do not mention but will not forget!

Many thanks to Sally Gillard, Paul Buck and every staff in Christ Church! The accommodation and facilities are so good that I want to live here forever!

Huge thanks to CSC-NDM studentship which make my life so easy in Oxford and allow me to fully focus on research and study!

Of course, there are my parents and wife who …… this is *cliché*, and they are shy, so skip it!

References:

1 Henry, R. Etymologia: poliomyelitis. *Emerging Infectious Diseases* **25**, 1611 (2019).

2 J., H. Über die acute Kinderlähmung. *Medizinische Zeitung, Berlin* **9**, 121-124 (1840).

3 Landsteiner, K. Ubertragung der Poliomyelitis acuta auf Affen. *Z Immunitatsforsch* **2**, 377-390 (1909).

4 Eggers, H. J. Milestones in early poliomyelitis research (1840 to 1949). *J Virol* **73**, 4533-4535 (1999).

5 Dalldorf, G. & Sickles, G. M. An Unidentified, Filtrable Agent Isolated From the Feces of Children With Paralysis. *Science* **108**, 61-62 (1948).

6 Brouwer, L., Moreni, G., Wolthers, K. C. & Pajkrt, D. World-Wide Prevalence and Genotype Distribution of Enteroviruses. *Viruses* **13**, 434 (2021).

7 Richardson, M., Elliman, D., Maguire, H., Simpson, J. & Nicoll, A. Evidence base of incubation periods, periods of infectiousness and exclusion policies for the control of communicable diseases in schools and preschools. *The Pediatric infectious disease journal* **20**, 380-391 (2001).

8 Tee, H. K., Zainol, M. I., Sam, I.-C. & Chan, Y. F. Recent advances in the understanding of enterovirus A71 infection: a focus on neuropathogenesis. *Expert review of anti-infective therapy* **19**, 733-747 (2021).

9 Versalovic, J. *Manual of clinical microbiology*. Vol. 1 (American Society for Microbiology Press, 2011).

10 Knipe, D. & Howley, P. (Wolters Kluwer Health, 2013).

11 Caspar, D. L. & Klug, A. Physical principles in the construction of regular viruses. *Cold Spring Harb Symp Quant Biol* **27**, 1-24 (1962).

12 Argos, P., Tsukihara, T. & Rossmann, M. G. A structural comparison of concanavalin A and tomato bushy stunt virus protein. *Journal of molecular evolution* **15**, 169-179 (1980).

13 Kiener, T. K. *et al.* Characterization and specificity of the linear epitope of the enterovirus 71 VP2 protein. *Virology journal* **9**, 1-11 (2012).

14 Yuan, J. *et al.* Enterovirus A71 proteins: structure and function. *Frontiers in microbiology* **9**, 286 (2018).

15 Plevka, P., Perera, R., Cardosa, J., Kuhn, R. J. & Rossmann, M. G. Crystal structure of human enterovirus 71. *Science* **336**, 1274-1274 (2012).

16 Rossmann, M. G. *et al.* Structure of a human common cold virus and functional relationship to other picornaviruses. *Nature* **317**, 145-153 (1985).

17 Strauss, M. *et al.* Nectin-like interactions between poliovirus and its receptor trigger conformational changes associated with cell entry. *J Virol* **89**, 4143-4157 (2015).

18 Baggen, J. *et al.* Role of enhanced receptor engagement in the evolution of a pandemic acute hemorrhagic conjunctivitis virus. *Proceedings of the National Academy of Sciences* **115**, 397-402 (2018).
19 Zhou, D. *et al.* Unexpected mode of engagement between enterovirus 71 and its receptor SCARB2. *Nature microbiology* **4**, 414-419 (2019).
20 Lee, S. E. *et al.* Progress Toward Poliomyelitis Eradication—Worldwide, January 2021–March 2023. *Morbidity and Mortality Weekly Report* **72**, 517 (2023).
21 Bigouette, J. P. *et al.* Update on vaccine-derived poliovirus outbreaks—worldwide, January 2021–December 2022. *Morbidity and Mortality Weekly Report* **72**, 366 (2023).
22 Laitinen, O. H. *et al.* Enteroviral proteases: structure, host interactions and pathogenicity. *Rev Med Virol* **26**, 251-267 (2016).
23 Rossmann, M. G., He, Y. & Kuhn, R. J. Picornavirus–receptor interactions. *Trends in microbiology* **10**, 324-331 (2002).
24 Greve, J. M. *et al.* The major human rhinovirus receptor is ICAM-1. *Cell* **56**, 839-847 (1989).
25 Bergelson, J. M. *et al.* Isolation of a common receptor for Coxsackie B viruses and adenoviruses 2 and 5. *Science* **275**, 1320-1323 (1997).
26 Mendelsohn, C. L., Wimmer, E. & Racaniello, V. R. Cellular receptor for poliovirus: molecular cloning, nucleotide sequence, and expression of a new member of the immunoglobulin superfamily. *Cell* **56**, 855-865 (1989).
27 Hofer, F. *et al.* Members of the low density lipoprotein receptor family mediate cell entry of a minor-group common cold virus. *Proceedings of the National Academy of Sciences* **91**, 1839-1842 (1994).
28 Yamayoshi, S. *et al.* Scavenger receptor B2 is a cellular receptor for enterovirus 71. *Nature medicine* **15**, 798-801 (2009).
29 Roivainen, M. *et al.* RGD-dependent entry of coxsackievirus A9 into host cells and its bypass after cleavage of VP1 protein by intestinal proteases. *Journal of virology* **65**, 4735-4740 (1991).
30 Roivainen, M. *et al.* Entry of coxsackievirus A9 into host cells: specific interactions with αvβ3 integrin, the vitronectin receptor. *Virology* **203**, 357-365 (1994).
31 Hafenstein, S. *et al.* Interaction of decay-accelerating factor with coxsackievirus B3. *Journal of virology* **81**, 12927-12935 (2007).
32 Ohka, S. & Nomoto, A. Recent insights into poliovirus pathogenesis. *Trends in microbiology* **9**, 501-506 (2001).
33 Iwasaki, A. *et al.* Immunofluorescence analysis of poliovirus receptor expression in Peyer's patches of humans, primates, and CD155 transgenic mice: implications for poliovirus infection. *The Journal of infectious diseases* **186**, 585-592 (2002).

34 Marjomäki, V. *et al.* Internalization of echovirus 1 in caveolae. *Journal of virology* **76**, 1856-1865 (2002).
35 Heikkilä, O. *et al.* Internalization of coxsackievirus A9 is mediated by β2-microglobulin, dynamin, and Arf6 but not by caveolin-1 or clathrin. *Journal of virology* **84**, 3666-3681 (2010).
36 Ren, J. *et al.* Picornavirus uncoating intermediate captured in atomic detail. *Nature communications* **4**, 1929 (2013).
37 Guest, S., Pilipenko, E., Sharma, K., Chumakov, K. & Roos, R. P. Molecular mechanisms of attenuation of the Sabin strain of poliovirus type 3. *Journal of virology* **78**, 11097-11107 (2004).
38 Valcárcel, J. & Gebauer, F. Post-transcriptional regulation: the dawn of PTB. *Current Biology* **7**, R705-R708 (1997).
39 Lind, K., Hühn, M. & Flodström-Tullberg, M. Immunology in the clinic review series; focus on type 1 diabetes and viruses: the innate immune response to enteroviruses and its possible role in regulating type 1 diabetes. *Clinical & Experimental Immunology* **168**, 30-38 (2012).
40 Lee, Y. F., Nomoto, A., Detjen, B. M. & Wimmer, E. A protein covalently linked to poliovirus genome RNA. *Proceedings of the National Academy of Sciences* **74**, 59-63 (1977).
41 Yogo, Y. & Wimmer, E. Polyadenylic acid at the 3′-terminus of poliovirus RNA. *Proceedings of the National Academy of Sciences* **69**, 1877-1882 (1972).
42 Kräusslich, H.-G., Nicklin, M. J., Lee, C.-K. & Wimmer, E. Polyprotein processing in picornavirus replication. *Biochimie* **70**, 119-130 (1988).
43 Nicklin, M., Kräusslich, H., Toyoda, H., Dunn, J. J. & Wimmer, E. Poliovirus polypeptide precursors: expression in vitro and processing by exogenous 3C and 2A proteinases. *Proceedings of the National Academy of Sciences* **84**, 4002-4006 (1987).
44 Toyoda, H. *et al.* A second virus-encoded proteinase involved in proteolytic processing of poliovirus polyprotein. *Cell* **45**, 761-770 (1986).
45 Hober, D. *et al.* Chapter Viruses and Type 1 Diabetes: Focus on the Enteroviruses. (2013).
46 Basavappa, R. *et al.* Role and mechanism of the maturation cleavage of VP0 in poliovirus assembly: structure of the empty capsid assembly intermediate at 2.9 Å resolution. *Protein Science* **3**, 1651-1669 (1994).
47 Suhy, D. A., Giddings Jr, T. H. & Kirkegaard, K. Remodeling the endoplasmic reticulum by poliovirus infection and by individual viral proteins: an autophagy-like origin for virus-induced vesicles. *Journal of virology* **74**, 8953-8965 (2000).

48 Pathak, H. B., Arnold, J. J., Wiegand, P. N., Hargittai, M. R. & Cameron, C. E. Picornavirus genome replication: assembly and organization of the VPg uridylylation ribonucleoprotein (initiation) complex. *Journal of Biological Chemistry* **282**, 16202-16213 (2007).

49 Novak, J. E. & Kirkegaard, K. Improved method for detecting poliovirus negative strands used to demonstrate specificity of positive-strand encapsidation and the ratio of positive to negative strands in infected cells. *Journal of virology* **65**, 3384-3387 (1991).

50 Nugent, C. I., Johnson, K. L., Sarnow, P. & Kirkegaard, K. Functional coupling between replication and packaging of poliovirus replicon RNA. *Journal of virology* **73**, 427-435 (1999).

51 Pfister, T., Pasamontes, L., Troxler, M., Egger, D. & Bienz, K. Immunocytochemical localization of capsid-related particles in subcellular fractions of poliovirus-infected cells. *Virology* **188**, 676-684 (1992).

52 Inal, J. M. & Jorfi, S. Coxsackievirus B transmission and possible new roles for extracellular vesicles. *Biochemical Society Transactions* **41**, 299-302 (2013).

53 Robinson, S. M. *et al.* Coxsackievirus B exits the host cell in shed microvesicles displaying autophagosomal markers. *PLoS pathogens* **10**, e1004045 (2014).

54 Chehadeh, W. *et al.* Persistent infection of human pancreatic islets by coxsackievirus B is associated with alpha interferon synthesis in β cells. *Journal of virology* **74**, 10153-10164 (2000).

55 Jartti, T., Lehtinen, P., Vuorinen, T., Koskenvuo, M. & Ruuskanen, O. Persistence of rhinovirus and enterovirus RNA after acute respiratory illness in children. *Journal of medical virology* **72**, 695-699 (2004).

56 Klingel, K. *et al.* Ongoing enterovirus-induced myocarditis is associated with persistent heart muscle infection: quantitative analysis of virus replication, tissue damage, and inflammation. *Proceedings of the National Academy of Sciences* **89**, 314-318 (1992).

57 Stenfeldt, C., Diaz-San Segundo, F., De Los Santos, T., Rodriguez, L. L. & Arzt, J. The pathogenesis of foot-and-mouth disease in pigs. *Frontiers in veterinary science* **3**, 41 (2016).

58 Stenfeldt, C., Pacheco, J. M., Borca, M. V., Rodriguez, L. L. & Arzt, J. Morphologic and phenotypic characteristics of myocarditis in two pigs infected by foot-and mouth disease virus strains of serotypes O or A. *Acta Veterinaria Scandinavica* **56**, 1-7 (2014).

59 Huang, K.-Y. A. *et al.* Emergence of genotype C1 Enterovirus A71 and its link with antigenic variation of virus in Taiwan. *PLoS Pathogens* **16**, e1008857 (2020).

60 Sei, J. J., Waters, R. A., Kenney, M., Barlow, J. W. & Golde, W. T. Effect of foot-and-mouth disease virus infection on the frequency, phenotype and function of circulating dendritic cells in cattle. *PLoS One* **11**, e0152192 (2016).

61 Nfon, C. K., Toka, F. N., Kenney, M., Pacheco, J. M. & Golde, W. T. Loss of plasmacytoid dendritic cell function coincides with lymphopenia and viremia during foot-and-mouth disease virus infection. *Viral immunology* **23**, 29-41 (2010).

62 Toka, F. N., Nfon, C., Dawson, H. & Golde, W. T. Natural killer cell dysfunction during acute infection with foot-and-mouth disease virus. *Clinical and vaccine immunology* **16**, 1738-1749 (2009).

63 Li, D. *et al.* Foot-and-mouth disease virus non-structural protein 3A inhibits the interferon-β signaling pathway. *Scientific reports* **6**, 21888 (2016).

64 Li, M. *et al.* Foot-and-mouth disease virus non-structural protein 2B negatively regulates the RLR-mediated IFN-β induction. *Biochemical and biophysical research communications* **504**, 238-244 (2018).

65 Zhu, Z. *et al.* Foot-and-mouth disease virus infection inhibits LGP2 protein expression to exaggerate inflammatory response and promote viral replication. *Cell death & disease* **8**, e2747-e2747 (2017).

66 Zhu, Z. *et al.* Foot-and-mouth disease virus viroporin 2B antagonizes RIG-I-mediated antiviral effects by inhibition of its protein expression. *Journal of virology* **90**, 11106-11121 (2016).

67 Rodríguez Pulido, M. *et al.* Innate immune sensor LGP2 is cleaved by the Leader protease of foot-and-mouth disease virus. *PLoS Pathogens* **14**, e1007135 (2018).

68 Li, D. *et al.* The VP3 structural protein of foot‐and‐mouth disease virus inhibits the IFN‐β signaling pathway. *The FASEB Journal* **30**, 1757-1766 (2016).

69 Li, D. *et al.* Poly (rC) binding protein 2 interacts with VP0 and increases the replication of the foot-and-mouth disease virus. *Cell Death & Disease* **10**, 516 (2019).

70 Wang, D. *et al.* Foot-and-mouth disease virus leader proteinase inhibits dsRNA-induced type I interferon transcription by decreasing interferon regulatory factor 3/7 in protein levels. *Biochemical and biophysical research communications* **399**, 72-78 (2010).

71 Mu, H., Ma, X., Luo, Z., Zhang, J. & Zheng, H. Structural protein VP0 of foot-and-mouth disease virus inhibits type I interferon signaling pathway. *Acta Microbiologica Sinica* **57**, 1-11 (2017).

72 Li, D. *et al.* Foot-and-mouth disease virus structural protein VP3 degrades Janus kinase 1 to inhibit IFN-γ signal transduction pathways. *Cell cycle* **15**, 850-860 (2016).

73 Du, Y. *et al.* 3Cpro of foot-and-mouth disease virus antagonizes the interferon signaling pathway by blocking STAT1/STAT2 nuclear translocation. *Journal of virology* **88**, 4908-4920 (2014).

74 Medina, G. N. *et al.* Interaction between FMDV Lpro and transcription factor ADNP is required for optimal viral replication. *Virology* **505**, 12-22 (2017).
75 Gingras, A.-C., Raught, B. & Sonenberg, N. eIF4 initiation factors: effectors of mRNA recruitment to ribosomes and regulators of translation. *Annual review of biochemistry* **68**, 913-963 (1999).
76 Glaser, W., Cencic, R. & Skern, T. Foot-and-mouth disease virus leader proteinase: involvement of C-terminal residues in self-processing and cleavage of eIF4GI. *Journal of Biological Chemistry* **276**, 35473-35481 (2001).
77 Lawrence, P., Schafer, E. A. & Rieder, E. The nuclear protein Sam68 is cleaved by the FMDV 3C protease redistributing Sam68 to the cytoplasm during FMDV infection of host cells. *Virology* **425**, 40-52 (2012).
78 Belsham, G. J., McInerney, G. M. & Ross-Smith, N. Foot-and-mouth disease virus 3C protease induces cleavage of translation initiation factors eIF4A and eIF4G within infected cells. *Journal of virology* **74**, 272-280 (2000).
79 Sun, P. *et al.* Foot-and-mouth disease virus capsid protein VP2 activates the cellular EIF2S1-ATF4 pathway and induces autophagy via HSPB1. *Autophagy* **14**, 336-346 (2018).
80 Gladue, D. *et al.* Foot-and-mouth disease virus nonstructural protein 2C interacts with Beclin1, modulating virus replication. *Journal of virology* **86**, 12080-12090 (2012).
81 Puenpa, J., Wanlapakorn, N., Vongpunsawad, S. & Poovorawan, Y. The history of enterovirus A71 outbreaks and molecular epidemiology in the Asia-Pacific region. *Journal of biomedical science* **26**, 1-11 (2019).
82 Oberste, M. S., Maher, K., Kilpatrick, D. R. & Pallansch, M. A. Molecular evolution of the human enteroviruses: correlation of serotype with VP1 sequence and application to picornavirus classification. *Journal of virology* **73**, 1941-1948 (1999).
83 Wang, J., Hu, Y. & Zheng, M. Enterovirus A71 antivirals: Past, present, and future. *Acta Pharmaceutica Sinica B* **12**, 1542-1566 (2022).
84 De Palma, A. M., Vliegen, I., De Clercq, E. & Neyts, J. Selective inhibitors of picornavirus replication. *Medicinal research reviews* **28**, 823-884 (2008).
85 Thibaut, H. J., De Palma, A. M. & Neyts, J. Combating enterovirus replication: state-of-the-art on antiviral research. *Biochemical pharmacology* **83**, 185-192 (2012).
86 Anasir, M. I., Zarif, F. & Poh, C. L. Antivirals blocking entry of enteroviruses and therapeutic potential. *Journal of biomedical science* **28**, 1-12 (2021).
87 Plevka, P. *et al.* Structure of human enterovirus 71 in complex with a capsid-binding inhibitor. *Proceedings of the National Academy of Sciences* **110**, 5463-5467 (2013).
88 Abzug, M. J. *et al.* A randomized, double-blind, placebo-controlled trial of pleconaril for the treatment of neonates with enterovirus sepsis. *Journal of the Pediatric Infectious Diseases Society* **5**, 53-62 (2016).

89 Pevear, D. C. *et al.* Relationship of pleconaril susceptibility and clinical outcomes in treatment of common colds caused by rhinoviruses. *Antimicrobial agents and chemotherapy* **49**, 4492-4499 (2005).

90 Benschop, K. *et al.* Genetic and antigenic structural characterization for resistance of echovirus 11 to pleconaril in an immunocompromised patient. *Journal of General Virology* **96**, 571-579 (2015).

91 Ma, C., Hu, Y., Zhang, J., Musharrafieh, R. & Wang, J. A novel capsid binding inhibitor displays potent antiviral activity against enterovirus D68. *ACS infectious diseases* **5**, 1952-1962 (2019).

92 Senior, K. FDA panel rejects common cold treatment. *The Lancet infectious diseases* **2**, 264 (2002).

93 Ho, J.-Y. *et al.* In vitro and in vivo studies of a potent capsid-binding inhibitor of enterovirus 71. *Journal of Antimicrobial Chemotherapy* **71**, 1922-1932 (2016).

94 De Colibus, L. *et al.* More-powerful virus inhibitors from structure-based analysis of HEV71 capsid-binding molecules. *Nature structural & molecular biology* **21**, 282-288 (2014).

95 Hsieh, C.-F. *et al.* Rosmarinic acid exhibits broad anti-enterovirus A71 activity by inhibiting the interaction between the five-fold axis of capsid VP1 and cognate sulfated receptors. *Emerging microbes & infections* **9**, 1194-1205 (2020).

96 Meng, T., Jia, Q., Wong, S.-M. & Chua, K.-B. In vitro and in vivo inhibition of the infectivity of human enterovirus 71 by a sulfonated food azo dye, brilliant black BN. *Journal of Virology* **93**, e00061-00019 (2019).

97 Egorova, A., Ekins, S., Schmidtke, M. & Makarov, V. Back to the future: Advances in development of broad-spectrum capsid-binding inhibitors of enteroviruses. *European journal of medicinal chemistry* **178**, 606-622 (2019).

98 Martinez-Gualda, B. *et al.* Scaffold simplification strategy leads to a novel generation of dual human immunodeficiency virus and enterovirus-A71 entry inhibitors. *Journal of Medicinal Chemistry* **63**, 349-368 (2019).

99 Wang, C.-Y. *et al.* Antiviral potential of a novel compound CW-33 against enterovirus A71 via inhibition of viral 2A protease. *Viruses* **7**, 3155-3171 (2015).

100 Falah, N. *et al.* Blocking human enterovirus 71 replication by targeting viral 2A protease. *Journal of antimicrobial chemotherapy* **67**, 2865-2869 (2012).

101 Cortez, K. J. *et al.* Infections Caused by Scedosporium spp. *Clinical Microbiology Reviews* **21**, 157-197 (2008).

102 Zhai, Y. *et al.* Cyanohydrin as an Anchoring Group for Potent and Selective Inhibitors of Enterovirus 71 3C Protease. *Journal of Medicinal Chemistry* **58**, 9414-9420 (2015).

103 Zhang, L. *et al.* α-Ketoamides as Broad-Spectrum Inhibitors of Coronavirus and Enterovirus Replication: Structure-Based Design, Synthesis, and Activity Assessment. *Journal of Medicinal Chemistry* **63**, 4562-4578 (2020).

104 Li, P. *et al.* Design, synthesis, and evaluation of a novel macrocyclic anti-EV71 agent. *Bioorganic & Medicinal Chemistry* **28**, 115551 (2020).
105 Wang, S.-H., Wang, K., Zhao, K., Hua, S.-C. & Du, J. The structure, function, and mechanisms of action of enterovirus non-structural protein 2C. *Frontiers in Microbiology* **11**, 615965 (2020).
106 Xia, H. *et al.* Human enterovirus nonstructural protein 2CATPase functions as both an RNA helicase and ATP-independent RNA chaperone. *PLoS pathogens* **11**, e1005067 (2015).
107 Guan, H. *et al.* Crystal structure of 2C helicase from enterovirus 71. *Science advances* **3**, e1602573 (2017).
108 Nagy, P. D., Strating, J. R. & van Kuppeveld, F. J. Building viral replication organelles: close encounters of the membrane types. *PLoS pathogens* **12**, e1005912 (2016).
109 Li, X. *et al.* Enterovirus replication organelles and inhibitors of their formation. *Frontiers in Microbiology* **11**, 1817 (2020).
110 Lyoo, H. *et al.* ACBD3 is an essential pan-enterovirus host factor that mediates the interaction between viral 3A protein and cellular protein PI4KB. *MBio* **10**, 10.1128/mbio. 02742-02718 (2019).
111 Horova, V. *et al.* Convergent evolution in the mechanisms of ACBD3 recruitment to picornavirus replication sites. *PLoS pathogens* **15**, e1007962 (2019).
112 Yates, M. K. & Seley-Radtke, K. L. The evolution of antiviral nucleoside analogues: A review for chemists and non-chemists. Part II: Complex modifications to the nucleoside scaffold. *Antiviral research* **162**, 5-21 (2019).
113 Seley-Radtke, K. L. & Yates, M. K. The evolution of nucleoside analogue antivirals: A review for chemists and non-chemists. Part 1: Early structural modifications to the nucleoside scaffold. *Antiviral research* **154**, 66-86 (2018).
114 Van Der Linden, L. *et al.* The RNA template channel of the RNA-dependent RNA polymerase as a target for development of antiviral therapy of multiple genera within a virus family. *PLoS pathogens* **11**, e1004733 (2015).
115 Lai, M.-C., Chen, H.-H., Xu, P. & Wang, R. Y. Translation control of Enterovirus A71 gene expression. *Journal of Biomedical Science* **27**, 1-9 (2020).
116 Davila-Calderon, J. *et al.* IRES-targeting small molecule inhibits enterovirus 71 replication via allosteric stabilization of a ternary complex. *Nature communications* **11**, 4775 (2020).
117 Melia, C. E. *et al.* Origins of enterovirus replication organelles established by whole-cell electron microscopy. *MBio* **10**, 10.1128/mbio. 00951-00919 (2019).
118 Xie, S. *et al.* DIDS blocks a chloride-dependent current that is mediated by the 2B protein of enterovirus 71. *Cell Research* **21**, 1271-1275 (2011).
119 Nieva, J. L., Madan, V. & Carrasco, L. Viroporins: structure and biological functions. *Nature Reviews Microbiology* **10**, 563-574 (2012).

120 Shih, S.-R., Stollar, V. & Li, M.-L. Host factors in enterovirus 71 replication. *Journal of virology* **85**, 9658-9666 (2011).
121 Lim, Z. Q., Ng, Q. Y., Ng, J. W. Q., Mahendran, V. & Alonso, S. Recent progress and challenges in drug development to fight hand, foot and mouth disease. *Expert opinion on drug discovery* **15**, 359-371 (2020).
122 Byers, L. & Wolfenden, R. A potent reversible inhibitor of carboxypeptidase A. *Journal of Biological Chemistry* **247**, 606-608 (1972).
123 Patlak, M. From viper's venom to drug design: treating hypertension. *The FASEB Journal* **18**, 421-421 (2004).
124 Baldwin, J. J. *et al.* Thienothiopyran-2-sulfonamides: novel topically active carbonic anhydrase inhibitors for the treatment of glaucoma. *Journal of medicinal chemistry* **32**, 2510-2513 (1989).
125 Sorzano, C. O. S. *et al.* Survey of the analysis of continuous conformational variability of biological macromolecules by electron microscopy. *Acta Crystallographica Section F: Structural Biology Communications* **75**, 19-32 (2019).
126 Dubochet, J., Lepault, J., Freeman, R., Berriman, J. & Homo, J. C. Electron microscopy of frozen water and aqueous solutions. *Journal of Microscopy* **128**, 219-237 (1982).
127 Ripstein, Z. & Rubinstein, J. Processing of cryo-EM movie data. *Methods in enzymology* **579**, 103-124 (2016).
128 Glaeser, R. M. & Han, B.-G. Opinion: hazards faced by macromolecules when confined to thin aqueous films. *Biophysics reports* **3**, 1-7 (2017).
129 Taylor, K. A. & Glaeser, R. M. Retrospective on the early development of cryoelectron microscopy of macromolecules and a prospective on opportunities for the future. *Journal of structural biology* **163**, 214-223 (2008).
130 Noble, A. J. *et al.* Routine single particle CryoEM sample and grid characterization by tomography. *Elife* **7**, e34257 (2018).
131 D'Imprima, E. *et al.* Protein denaturation at the air-water interface and how to prevent it. *Elife* **8**, e42747 (2019).
132 Vinothkumar, K. R. & Henderson, R. Single particle electron cryomicroscopy: trends, issues and future perspective. *Quarterly reviews of biophysics* **49**, e13 (2016).
133 Klebl, D. P. *et al.* Need for speed: examining protein behavior during CryoEM grid preparation at different timescales. *Structure* **28**, 1238-1248. e1234 (2020).
134 Brilot, A. F. *et al.* Beam-induced motion of vitrified specimen on holey carbon film. *Journal of structural biology* **177**, 630-637 (2012).
135 Campbell, M. G. *et al.* Movies of ice-embedded particles enhance resolution in electron cryo-microscopy. *Structure* **20**, 1823-1828 (2012).
136 Li, X. *et al.* Electron counting and beam-induced motion correction enable near-atomic-resolution single-particle cryo-EM. *Nature methods* **10**, 584-590 (2013).

137 Scheres, S. H. Beam-induced motion correction for sub-megadalton cryo-EM particles. *elife* **3**, e03665 (2014).
138 Russo, C. J. & Passmore, L. A. Ultrastable gold substrates for electron cryomicroscopy. *Science* **346**, 1377-1380 (2014).
139 Nakane, T. *et al.* Single-particle cryo-EM at atomic resolution. *Nature* **587**, 152-156 (2020).
140 Yip, K. M., Fischer, N., Paknia, E., Chari, A. & Stark, H. Atomic-resolution protein structure determination by cryo-EM. *Nature* **587**, 157-161 (2020).
141 Zhang, K., Pintilie, G. D., Li, S., Schmid, M. F. & Chiu, W. Resolving individual atoms of protein complex by cryo-electron microscopy. *Cell research* **30**, 1136-1139 (2020).
142 Ricolleau, C. *et al.* High resolution imaging and spectroscopy using Cs-corrected TEM with cold FEG JEM-ARM200F. *JEOL news* **47**, 2-8 (2012).
143 Zivanov, J., Nakane, T. & Scheres, S. H. Estimation of high-order aberrations and anisotropic magnification from cryo-EM data sets in RELION-3.1. *IUCrJ* **7**, 253-267 (2020).
144 Sun, M. *et al.* Practical considerations for using K3 cameras in CDS mode for high-resolution and high-throughput single particle cryo-EM. *Journal of structural biology* **213**, 107745 (2021).
145 Eng, E. T. *et al.* Reducing cryoEM file storage using lossy image formats. *Journal of structural biology* **207**, 49-55 (2019).
146 Guo, H. *et al.* Electron-event representation data enable efficient cryoEM file storage with full preservation of spatial and temporal resolution. *IUCrJ* **7**, 860-869 (2020).
147 Turnbaugh, C. *et al.* High-power near-concentric Fabry–Perot cavity for phase contrast electron microscopy. *Review of scientific instruments* **92** (2021).
148 Buijsse, B., Trompenaars, P., Altin, V., Danev, R. & Glaeser, R. M. Spectral DQE of the Volta phase plate. *Ultramicroscopy* **218**, 113079 (2020).
149 Carragher, B. *et al.* Leginon: an automated system for acquisition of images from vitreous ice specimens. *Journal of structural biology* **132**, 33-45 (2000).
150 Suloway, C. *et al.* Automated molecular microscopy: the new Leginon system. *Journal of structural biology* **151**, 41-60 (2005).
151 Cheng, A. *et al.* Leginon: New features and applications. *Protein Science* **30**, 136-150 (2021).
152 Mastronarde, D. N. Automated electron microscope tomography using robust prediction of specimen movements. *Journal of structural biology* **152**, 36-51 (2005).
153 Zhang, J. *et al.* JADAS: a customizable automated data acquisition system and its application to ice-embedded single particles. *Journal of structural biology* **165**, 1-9 (2009).
154 Cheng, A. *et al.* High resolution single particle cryo-electron microscopy using beam-image shift. *Journal of structural biology* **204**, 270-275 (2018).

155 Wu, C., Huang, X., Cheng, J., Zhu, D. & Zhang, X. High-quality, high-throughput cryo-electron microscopy data collection via beam tilt and astigmatism-free beam-image shift. *Journal of structural biology* **208**, 107396 (2019).
156 Zivanov, J. *et al.* New tools for automated high-resolution cryo-EM structure determination in RELION-3. *elife* **7**, e42166 (2018).
157 Zivanov, J. *et al.* New tools for automated high-resolution cryo-EM structure determination in RELION-3. *Elife* **7** (2018).
158 Zivanov, J., Nakane, T. & Scheres, S. H. A Bayesian approach to beam-induced motion correction in cryo-EM single-particle analysis. *IUCrJ* **6**, 5-17 (2019).
159 Russo, C. J. & Henderson, R. Ewald sphere correction using a single side-band image processing algorithm. *Ultramicroscopy* **187**, 26-33 (2018).
160 DeRosier, D. J. Correction of high-resolution data for curvature of the Ewald sphere. *Ultramicroscopy* **81**, 83-98 (2000).
161 Seitz, I. *et al.* DNA-origami-directed virus capsid polymorphism. *Nature Nanotechnology*, 1-8 (2023).
162 Bai, X.-c., Rajendra, E., Yang, G., Shi, Y. & Scheres, S. H. Sampling the conformational space of the catalytic subunit of human γ-secretase. *elife* **4**, e11182 (2015).
163 Nakane, T., Kimanius, D., Lindahl, E. & Scheres, S. H. Characterisation of molecular motions in cryo-EM single-particle data by multi-body refinement in RELION. *elife* **7**, e36861 (2018).
164 Punjani, A. & Fleet, D. J. 3D variability analysis: Resolving continuous flexibility and discrete heterogeneity from single particle cryo-EM. *Journal of structural biology* **213**, 107702 (2021).
165 Maji, S. *et al.* Propagation of conformational coordinates across angular space in mapping the continuum of states from cryo-EM data by manifold embedding. *Journal of chemical information and modeling* **60**, 2484-2491 (2020).
166 Chen, M. & Ludtke, S. J. Deep learning-based mixed-dimensional Gaussian mixture model for characterizing variability in cryo-EM. *Nature methods* **18**, 930-936 (2021).
167 Zhong, E. D., Bepler, T., Berger, B. & Davis, J. H. CryoDRGN: reconstruction of heterogeneous cryo-EM structures using neural networks. *Nature methods* **18**, 176-185 (2021).
168 Huiskonen, J. T. Image processing for cryogenic transmission electron microscopy of symmetry-mismatched complexes. *Biosci Rep* **38** (2018).
169 Hartley, C. *et al.* Kelp fly virus: a novel group of insect picorna-like viruses as defined by genome sequence analysis and a distinctive virion structure. *Journal of virology* **79**, 13385-13398 (2005).
170 Briggs, J. A. *et al.* Classification and three-dimensional reconstruction of unevenly distributed or symmetry mismatched features of icosahedral particles. *Journal of structural biology* **150**, 332-339 (2005).

171 Ilca, S. L. *et al.* Localized reconstruction of subunits from electron cryomicroscopy images of macromolecular complexes. *Nature communications* **6**, 8843 (2015).
172 Abrishami, V. *et al.* Localized reconstruction in Scipion expedites the analysis of symmetry mismatches in cryo-EM data. *Progress in Biophysics and Molecular Biology* **160**, 43-52 (2021).
173 Burnley, T., Palmer, C. M. & Winn, M. Recent developments in the CCP-EM software suite. *Acta Crystallographica Section D: Structural Biology* **73**, 469-477 (2017).
174 Afonine, P. V. *et al.* Real-space refinement in PHENIX for cryo-EM and crystallography. *Acta Crystallographica Section D: Structural Biology* **74**, 531-544 (2018).
175 Wang, R. Y.-R. *et al.* Automated structure refinement of macromolecular assemblies from cryo-EM maps using Rosetta. *Elife* **5**, e17219 (2016).
176 Pettersen, E. F. *et al.* UCSF Chimera—a visualization system for exploratory research and analysis. *Journal of computational chemistry* **25**, 1605-1612 (2004).
177 Croll, T. I. ISOLDE: a physically realistic environment for model building into low-resolution electron-density maps. *Acta Crystallographica Section D: Structural Biology* **74**, 519-530 (2018).
178 Casañal, A., Lohkamp, B. & Emsley, P. Current developments in Coot for macromolecular model building of Electron Cryo-microscopy and Crystallographic Data. *Protein Science* **29**, 1055-1064 (2020).
179 Rout, M. P. & Sali, A. Principles for integrative structural biology studies. *Cell* **177**, 1384-1403 (2019).
180 Hoh, S. W., Burnley, T. & Cowtan, K. Current approaches for automated model building into cryo-EM maps using Buccaneer with CCP-EM. *Acta Crystallographica Section D: Structural Biology* **76**, 531-541 (2020).
181 Terashi, G. & Kihara, D. De novo main-chain modeling for EM maps using MAINMAST. *Nature communications* **9**, 1618 (2018).
182 Terwilliger, T. C., Adams, P. D., Afonine, P. V. & Sobolev, O. V. A fully automatic method yielding initial models from high-resolution cryo-electron microscopy maps. *Nature methods* **15**, 905-908 (2018).
183 Si, D. *et al.* Deep learning to predict protein backbone structure from high-resolution cryo-EM density maps. *Scientific reports* **10**, 4282 (2020).
184 Senior, A. W. *et al.* Improved protein structure prediction using potentials from deep learning. *Nature* **577**, 706-710 (2020).
185 Baek, M. *et al.* Accurate prediction of protein structures and interactions using a three-track neural network. *Science* **373**, 871-876 (2021).
186 Lawson, C. L., Berman, H. M. & Chiu, W. Evolving data standards for cryo-EM structures. *Structural Dynamics* **7** (2020).

187 Patwardhan, A. Trends in the electron microscopy data bank (EMDB). *Acta Crystallographica Section D: Structural Biology* **73**, 503-508 (2017).
188 Chiu, W., Schmid, M. F., Pintilie, G. D. & Lawson, C. L. Evolution of standardization and dissemination of cryo-EM structures and data jointly by the community, PDB, and EMDB. *Journal of Biological Chemistry* **296** (2021).
189 Chang, L.-Y. *et al.* Risk factors of enterovirus 71 infection and associated hand, foot, and mouth disease/herpangina in children during an epidemic in Taiwan. *Pediatrics* **109**, e88-e88 (2002).
190 Jin, P. *et al.* Validation and evaluation of serological correlates of protection for inactivated enterovirus 71 vaccine in children aged 6-35 months. *Human Vaccines & Immunotherapeutics* **12**, 916-921 (2016).
191 Huang, K.-Y. A. Structural basis for neutralization of enterovirus. *Current Opinion in Virology* **51**, 199-206 (2021).
192 Zhu, L. *et al.* Neutralization mechanisms of two highly potent antibodies against human enterovirus 71. *MBio* **9**, 10.1128/mbio. 01013-01018 (2018).
193 Plevka, P. *et al.* Neutralizing antibodies can initiate genome release from human enterovirus 71. *Proceedings of the National Academy of Sciences* **111**, 2134-2139 (2014).
194 Huang, K.-Y. A. *et al.* Structural and functional analysis of protective antibodies targeting the threefold plateau of enterovirus 71. *Nature Communications* **11**, 5253 (2020).
195 Arthur Huang, K.-Y. *et al.* Epitope-associated and specificity-focused features of EV71-neutralizing antibody repertoires from plasmablasts of infected children. *Nature communications* **8**, 762 (2017).
196 Wang, K. *et al.* Structures of Echovirus 30 in complex with its receptors inform a rational prediction for enterovirus receptor usage. *Nature communications* **11**, 4421 (2020).
197 Zhao, X. *et al.* Human neonatal Fc receptor is the cellular uncoating receptor for enterovirus B. *Cell* **177**, 1553-1565. e1516 (2019).
198 Wang, K. *et al.* Serotype specific epitopes identified by neutralizing antibodies underpin immunogenic differences in Enterovirus B. *Nature communications* **11**, 4419 (2020).
199 Olson, N. H. *et al.* Structure of a human rhinovirus complexed with its receptor molecule. *Regulation of Gene Expression in Animal Viruses*, 1-12 (1993).
200 Smith, T. J., Olson, N. H., Cheng, R. H., Chase, E. S. & Baker, T. S. Structure of a human rhinovirus-bivalently bound antibody complex: implications for viral neutralization and antibody flexibility. *Proceedings of the National Academy of Sciences* **90**, 7015-7018 (1993).

201 Smith, T. J., Chase, E. S., Schmidt, T. J., Olson, N. H. & Baker, T. S. Neutralizing antibody to human rhinovirus 14 penetrates the receptor-binding canyon. *Nature* **383**, 350-354 (1996).

202 Che, Z. *et al.* Antibody-mediated neutralization of human rhinovirus 14 explored by means of cryoelectron microscopy and X-ray crystallography of virus-Fab complexes. *Journal of virology* **72**, 4610-4622 (1998).

203 Tormo, J. *et al.* Three‐dimensional structure of the Fab fragment of a neutralizing antibody to human rhinovirus serotype 2. *Protein Science* **1**, 1154-1161 (1992).

204 Tormo, J. *et al.* Docking of a human rhinovirus neutralizing antibody onto the viral capsid. *Proteins: Structure, Function, and Bioinformatics* **23**, 491-501 (1995).

205 Dong, Y. *et al.* Antibody-induced uncoating of human rhinovirus B14. *Proceedings of the National Academy of Sciences* **114**, 8017-8022 (2017).

206 He, M. *et al.* Identification of antibodies with non-overlapping neutralization sites that target coxsackievirus A16. *Cell host & microbe* **27**, 249-261. e245 (2020).

207 Yamayoshi, S. *et al.* Human SCARB2-dependent infection by coxsackievirus A7, A14, and A16 and enterovirus 71. *Journal of virology* **86**, 5686-5696 (2012).

208 Staring, J. *et al.* KREMEN1 is a host entry receptor for a major group of enteroviruses. *Cell Host & Microbe* **23**, 636-643. e635 (2018).

209 Zhao, Y. *et al.* Hand-foot-and-mouth disease virus receptor KREMEN1 binds the canyon of Coxsackie Virus A10. *Nature communications* **11**, 38 (2020).

210 Xu, L. *et al.* Atomic structures of Coxsackievirus A6 and its complex with a neutralizing antibody. *Nature communications* **8**, 505 (2017).

211 Zhu, R. *et al.* Discovery and structural characterization of a therapeutic antibody against coxsackievirus A10. *Science advances* **4**, eaat7459 (2018).

212 Riabi, S. *et al.* Study of Coxsackie B viruses interactions with Coxsackie Adenovirus receptor and Decay-Accelerating Factor using Human CaCo-2 cell line. *Journal of Biomedical Science* **21**, 1-9 (2014).

213 Xu, L. *et al.* Cryo-EM structures reveal the molecular basis of receptor-initiated coxsackievirus uncoating. *Cell host & microbe* **29**, 448-462. e445 (2021).

214 Liu, Y. *et al.* Sialic acid-dependent cell entry of human enterovirus D68. *Nature communications* **6**, 8865 (2015).

215 Vogt, M. R. *et al.* Human antibodies neutralize enterovirus D68 and protect against infection and paralytic disease. *Science immunology* **5**, eaba4902 (2020).

216 Zhang, C. *et al.* Functional and structural characterization of a two-MAb cocktail for delayed treatment of enterovirus D68 infections. *Nature communications* **12**, 2904 (2021).

217 Zheng, Q. *et al.* Atomic structures of enterovirus D68 in complex with two monoclonal antibodies define distinct mechanisms of viral neutralization. *Nature microbiology* **4**, 124-133 (2019).

218 Miehling, J., Goricanec, D. & Hagn, F. A Split-Intein-Based Method for the Efficient Production of Circularized Nanodiscs for Structural Studies of Membrane Proteins. *ChemBioChem* **19**, 1927-1933 (2018).
219 Aricescu, A. R., Lu, W. & Jones, E. Y. A time-and cost-efficient system for high-level protein production in mammalian cells. *Acta Crystallographica Section D: Biological Crystallography* **62**, 1243-1250 (2006).
220 Pettersen, E. F. *et al.* UCSF ChimeraX: Structure visualization for researchers, educators, and developers. *Protein Sci* **30**, 70-82 (2021).
221 Emsley, P. & Cowtan, K. Coot: model-building tools for molecular graphics. *Acta Crystallographica Section D: Biological Crystallography* **60**, 2126-2132 (2004).
222 Zhou, D. *et al.* Switching of Receptor Binding Poses between Closely Related Enteroviruses. *Viruses* **14**, 2625 (2022).
223 Zheng, S. Q. *et al.* MotionCor2: anisotropic correction of beam-induced motion for improved cryo-electron microscopy. *Nature Methods* **14**, 331-332 (2017).
224 Rohou, A. & Grigorieff, N. CTFFIND4: Fast and accurate defocus estimation from electron micrographs. *J Struct Biol* **192**, 216-221 (2015).
225 Tegunov, D. & Cramer, P. Real-time cryo-electron microscopy data preprocessing with Warp. *Nat Methods* **16**, 1146-1152 (2019).
226 Stuart, A. D. *et al.* Determination of the structure of a decay accelerating factor-binding clinical isolate of echovirus 11 allows mapping of mutants with altered receptor requirements for infection. *J Virol* **76**, 7694-7704 (2002).
227 Scheres, S. H. W. & Chen, S. Prevention of overfitting in cryo-EM structure determination. *Nature Methods* **9**, 853-854 (2012).
228 Lukacik, P. *et al.* Complement regulation at the molecular level: the structure of decay-accelerating factor. *Proceedings of the National Academy of Sciences* **101**, 1279-1284 (2004).
229 Krissinel, E. & Henrick, K. Inference of macromolecular assemblies from crystalline state. *Journal of molecular biology* **372**, 774-797 (2007).
230 Xiao, C. & Rossmann, M. G. Interpretation of electron density with stereographic roadmap projections. *Journal of structural biology* **158**, 182-187 (2007).
231 DeLano, W. L. Pymol: An open-source molecular graphics tool. *CCP4 Newsletter on protein crystallography* **40**, 82-92 (2002).
232 Walter, T. S. *et al.* A plate-based high-throughput assay for virus stability and vaccine formulation. *J Virol Methods* **185**, 166-170 (2012).
233 Stuart, D. I., Levine, M., Muirhead, H. & Stammers, D. K. Crystal structure of cat muscle pyruvate kinase at a resolution of 2.6 A. *J Mol Biol* **134**, 109-142 (1979).
234 Huerta-Cepas, J., Serra, F. & Bork, P. ETE 3: Reconstruction, Analysis, and Visualization of Phylogenomic Data. *Mol Biol Evol* **33**, 1635-1638 (2016).

235 Koskiniemi, M., Paetau, R. & Linnavuori, K. Severe encephalitis associated with disseminated echovirus 22 infection. *Scandinavian journal of infectious diseases* **21**, 463-466 (1989).
236 Tracy, S. *et al.* A molecular and serologic evaluation of enteroviral involvement in human myocarditis. *Journal of molecular and cellular cardiology* **22**, 403-414 (1990).
237 Carrol, E. *et al.* Clinical and diagnostic findings of an echovirus meningitis outbreak in the north west of England. *Postgraduate medical journal* **82**, 60-64 (2006).
238 Modlin, J. F. Perinatal echovirus infection: insights from a literature review of 61 cases of serious infection and 16 outbreaks in nurseries. *Reviews of infectious diseases* **8**, 918-926 (1986).
239 Rossmann, M. G. *et al.* Structure of a human common cold virus and functional relationship to other picornaviruses. *Nature* **317**, 145-153 (1985).
240 Zhao, X. *et al.* Human Neonatal Fc Receptor Is the Cellular Uncoating Receptor for Enterovirus B. *Cell* **177**, 1553-1565.e1516 (2019).
241 Nicholson-Weller, A., Burge, J., Fearon, D., Weller, P. & Austen, K. Isolation of a human erythrocyte membrane glycoprotein with decay-accelerating activity for C3 convertases of the complement system. *The Journal of Immunology* **129**, 184-189 (1982).
242 Medof, M. E., Kinoshita, T. & Nussenzweig, V. Inhibition of complement activation on the surface of cells after incorporation of decay-accelerating factor (DAF) into their membranes. *The Journal of experimental medicine* **160**, 1558-1578 (1984).
243 Kuttner-Kondo, L. A., Mitchell, L., Hourcade, D. E. & Medof, M. E. Characterization of the active sites in decay-accelerating factor. *The Journal of Immunology* **167**, 2164-2171 (2001).
244 Davis, L., Patel, S., Atkinson, J. & Lipsky, P. Decay-accelerating factor functions as a signal transducing molecule for human T cells. *The Journal of Immunology* **141**, 2246-2252 (1988).
245 Lublin, D. M. & Atkinson, J. Decay-accelerating factor: biochemistry, molecular biology, and function. *Annual review of immunology* **7**, 35-58 (1989).
246 Bergelson, J. M. *et al.* Decay-accelerating factor (CD55), a glycosylphosphatidylinositol-anchored complement regulatory protein, is a receptor for several echoviruses. *Proceedings of the National Academy of Sciences* **91**, 6245-6248 (1994).
247 Powell, R. *et al.* Characterization of echoviruses that bind decay accelerating factor (CD55): evidence that some haemagglutinating strains use more than one cellular receptor. *Journal of General Virology* **79**, 1707-1713 (1998).
248 Bhella, D. *et al.* The structure of echovirus type 12 bound to a two-domain fragment of its cellular attachment protein decay-accelerating factor (CD 55). *J Biol Chem* **279**, 8325-8332 (2004).

249 Plevka, P. *et al.* Interaction of decay-accelerating factor with echovirus 7. *J Virol* **84**, 12665-12674 (2010).
250 Niu, S. *et al.* Molecular and structural basis of Echovirus 11 infection by using the dual-receptor system of CD55 and FcRn. *Chinese Science Bulletin* **65**, 67-79 (2020).
251 Wang, K. *et al.* Structures of Echovirus 30 in complex with its receptors inform a rational prediction for enterovirus receptor usage. *Nature Communications* **11**, 4421 (2020).
252 Lea, S. M. *et al.* Determination of the affinity and kinetic constants for the interaction between the human virus echovirus 11 and its cellular receptor, CD55. *Journal of Biological Chemistry* **273**, 30443-30447 (1998).
253 Kotecha, A. *et al.* Rules of engagement between αvβ6 integrin and foot-and-mouth disease virus. *Nature Communications* **8**, 15408 (2017).
254 Goodfellow, I. G., Sioofy, A. B., Powell, R. M. & Evans, D. J. Echoviruses Bind Heparan Sulfate at the Cell Surface. *Journal of Virology* **75**, 4918-4921 (2001).
255 Rezaikin, A. V., Novoselov, A. V., Sergeev, A. G., Fadeyev, F. A. & Lebedev, S. V. Two clusters of mutations map distinct receptor-binding sites of echovirus 11 for the decay-accelerating factor (CD55) and for canyon-binding receptors. *Virus Res* **145**, 74-79 (2009).
256 Bamford, D. H., Grimes, J. M. & Stuart, D. I. What does structure tell us about virus evolution? *Curr Opin Struct Biol* **15**, 655-663 (2005).
257 Fry, E. E. *et al.* The structure and function of a foot-and-mouth disease virus-oligosaccharide receptor complex. *Embo j* **18**, 543-554 (1999).
258 Fry, E. E. *et al.* Structure of Foot-and-mouth disease virus serotype A10 61 alone and complexed with oligosaccharide receptor: receptor conservation in the face of antigenic variation. *J Gen Virol* **86**, 1909-1920 (2005).
259 Hogle, J., Chow, M. & Filman, D. Three-dimensional structure of poliovirus at 2.9 Å resolution. *Science* **229**, 1358-1365 (1985).
260 Takai, Y., Irie, K., Shimizu, K., Sakisaka, T. & Ikeda, W. Nectins and nectin-like molecules: roles in cell adhesion, migration, and polarization. *Cancer science* **94**, 655-667 (2003).
261 Strauss, M. *et al.* Nectin-like interactions between poliovirus and its receptor trigger conformational changes associated with cell entry. *Journal of virology* **89**, 4143-4157 (2015).
262 Tsang, S. K., Danthi, P., Chow, M. & Hogle, J. M. Stabilization of poliovirus by capsid-binding antiviral drugs is due to entropic effects. *Journal of molecular biology* **296**, 335-340 (2000).
263 Filman, D. J. *et al.* Structural factors that control conformational transitions and serotype specificity in type 3 poliovirus. *The EMBO journal* **8**, 1567-1579 (1989).

264 Belnap, D. M. *et al.* Molecular tectonic model of virus structural transitions: the putative cell entry states of poliovirus. *Journal of virology* **74**, 1342-1354 (2000).
265 Huang, Y., Hogle, J. M. & Chow, M. Is the 135S poliovirus particle an intermediate during cell entry? *Journal of Virology* **74**, 8757-8761 (2000).
266 Butan, C., Filman, D. J. & Hogle, J. M. Cryo-electron microscopy reconstruction shows poliovirus 135S particles poised for membrane interaction and RNA release. *Journal of virology* **88**, 1758-1770 (2014).
267 Fricks, C. E. & Hogle, J. M. Cell-induced conformational change in poliovirus: externalization of the amino terminus of VP1 is responsible for liposome binding. *Journal of virology* **64**, 1934-1945 (1990).
268 Chow, M. *et al.* Myristylation of picornavirus capsid protein VP4 and its structural significance. *Nature* **327**, 482-486 (1987).
269 Shah, P. N. *et al.* Cryo-EM structures reveal two distinct conformational states in a picornavirus cell entry intermediate. *PLoS pathogens* **16**, e1008920 (2020).
270 Curry, S., Chow, M. & Hogle, J. M. The poliovirus 135S particle is infectious. *Journal of virology* **70**, 7125-7131 (1996).
271 Le Bouvier, G. The modification of poliovirus antigens by heat and ultraviolet light. *Lancet*, 1013-1016 (1955).
272 Mayer, M. M. *et al.* The purification of poliomyelitis virus as studied by complement fixation. *The Journal of Immunology* **78**, 435-455 (1957).
273 Ferguson, M. o., Wood, D. J. & Minor, P. D. Antigenic structure of poliovirus in inactivated vaccines. *Journal of general virology* **74**, 685-690 (1993).
274 Minor, P. D., Ferguson, M., Evans, D. M., Almond, J. W. & Icenogle, J. P. Antigenic structure of polioviruses of serotypes 1, 2 and 3. *Journal of General Virology* **67**, 1283-1291 (1986).
275 Patel, V., Ferguson, M. & Minor, P. Antigenic sites on type 2 poliovirus. *Virology* **192**, 361-364 (1993).
276 Page, G. *et al.* Three-dimensional structure of poliovirus serotype 1 neutralizing determinants. *Journal of Virology* **62**, 1781-1794 (1988).
277 HARBER, J., BERNHARDT, G., LU, H.-H., SGRO, J.-Y. & WIMMER, E. Canyon rim residues, including antigenic determinants, modulate serotype-specific binding of polioviruses to mutants of the poliovirus receptor. *Virology* **214**, 559-570 (1995).
278 Lin, J., Cheng, N., Hogle, J. M., Steven, A. C. & Belnap, D. M. Conformational shift of a major poliovirus antigen confirmed by immuno-cryogenic electron microscopy. *The Journal of Immunology* **191**, 884-891 (2013).
279 Chen, Z. *et al.* Cross-neutralizing human anti-poliovirus antibodies bind the recognition site for cellular receptor. *Proceedings of the National Academy of Sciences* **110**, 20242-20247 (2013).

280 Lin, J. *et al.* Structure of the Fab-labeled “breathing” state of native poliovirus. *Journal of virology* **86**, 5959-5962 (2012).
281 Bostina, M., Levy, H., Filman, D. J. & Hogle, J. M. Poliovirus RNA is released from the capsid near a twofold symmetry axis. *Journal of virology* **85**, 776-783 (2011).
282 Le Bouvier, G. Poliovirus D and C antigens; their differentiation and measurement by precipitation in agar. *British Journal of Experimental Pathology* **40**, 452 (1959).
283 White, J. M. & Whittaker, G. R. Fusion of enveloped viruses in endosomes. *Traffic* **17**, 593-614 (2016).
284 Johnson, J. E. & Banerjee, M. Activation, exposure and penetration of virally encoded, membrane-active polypeptides during non-enveloped virus entry. *Current Protein and Peptide Science* **9**, 16-27 (2008).
285 Strauss, M., Levy, H. C., Bostina, M., Filman, D. J. & Hogle, J. M. RNA transfer from poliovirus 135S particles across membranes is mediated by long umbilical connectors. *Journal of virology* **87**, 3903-3914 (2013).
286 Abdelhakim, A. H. *et al.* Structural correlates of rotavirus cell entry. *PLoS pathogens* **10**, e1004355 (2014).
287 Kumar, M. & Blaas, D. Human rhinovirus subviral a particle binds to lipid membranes over a twofold axis of icosahedral symmetry. *Journal of Virology* **87**, 11309-11312 (2013).
288 Nasr, M. L. *et al.* Covalently circularized nanodiscs for studying membrane proteins and viral entry. *Nature methods* **14**, 49-52 (2017).
289 Zhao, Z. *et al.* DNA-corralled nanodiscs for the structural and functional characterization of membrane proteins and viral entry. *Journal of the American Chemical Society* **140**, 10639-10643 (2018).
290 Redelmeier, T., Hope, M. & Cullis, P. On the mechanism of transbilayer transport of phosphatidylglycerol in response to transmembrane pH gradients. *Biochemistry* **29**, 3046-3053 (1990).
291 Oeemig, J. S., Aranko, A. S., Djupsjöbacka, J., Heinämäki, K. & Iwaï, H. Solution structure of DnaE intein from Nostoc punctiforme: structural basis for the design of a new split intein suitable for site-specific chemical modification. *FEBS letters* **583**, 1451-1456 (2009).
292 Wu, J.-S. *et al.* Patterns of polymorphism and divergence in the VP1 gene of enterovirus 71 circulating in the Asia-Pacific region between 1994 and 2013. *Journal of virological methods* **193**, 713-728 (2013).
293 Nishimura, Y. *et al.* Human P-selectin glycoprotein ligand-1 is a functional receptor for enterovirus 71. *Nature medicine* **15**, 794-797 (2009).
294 Yamayoshi, S., Ohka, S., Fujii, K. & Koike, S. Functional comparison of SCARB2 and PSGL1 as receptors for enterovirus 71. *Journal of virology* **87**, 3335-3347 (2013).

295 Dang, M. *et al.* Molecular mechanism of SCARB2-mediated attachment and uncoating of EV71. *Protein & cell* **5**, 692-703 (2014).
296 Wang, X. *et al.* A sensor-adaptor mechanism for enterovirus uncoating from structures of EV71. *Nature structural & molecular biology* **19**, 424-429 (2012).
297 Calvo, D., Dopazo, J. & Vega, M. A. The CD36, CLA-1 (CD36L1), and LIMPII (CD36L2) gene family: cellular distribution, chromosomal location, and genetic evolution. *Genomics* **25**, 100-106 (1995).
298 Zhao, Y., Ren, J., Padilla-Parra, S., Fry, E. E. & Stuart, D. I. Lysosome sorting of β-glucocerebrosidase by LIMP-2 is targeted by the mannose 6-phosphate receptor. *Nature communications* **5**, 4321 (2014).
299 Dibbens, L., Schwake, M., Saftig, P. & Rubboli, G. SCARB2/LIMP2 deficiency in action myoclonus–renal failure syndrome. *Epileptic Disorders* **18**, S63-S72 (2016).
300 Eisenstein, F. *et al.* Parallel cryo electron tomography on in situ lamellae. *Nature Methods* **20**, 131-138 (2023).